Low-Energy Positron Scattering from Atoms and Molecules

Joshua Rueben Machacek

A thesis submitted for the degree of
Doctor of Philosophy of
The Australian National University

Australian
National
University

November, 2013

Declaration

This thesis covers research undertaken between February 2010 and April 2013 as part of the Australian Research Council Centre for Antimatter-Matter Studies in the Atomic and Molecular Physics Laboratories of The Research School of Physical Sciences and Engineering, The Australian National University, Canberra, Australia. To the best of the authors knowledge and belief, this thesis contains no material which has been accepted for the award of any other degree or diploma in any university. It contains no material previously published or written by another person, except where due reference is made in the text.

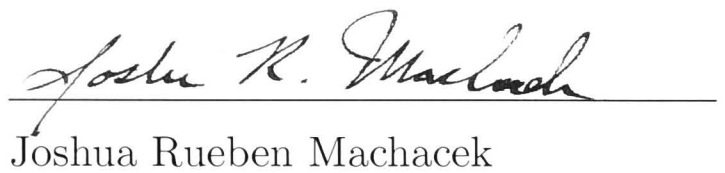

Joshua Rueben Machacek

3 December 2013

Acknowledgements

Many people have been influential in crafting the intellect which has completed this work. My parents; Tom and Sherri, instilled the work ethic. I don't think I could have made it as far as I did in the early years without this. A series of teachers deserve a great amount of credit for teaching me different ways of thinking and inspiring me. Mr. Ruewain (Brookings, SD) Builders and Engineers Club in Middle School, Mr. Winemiller (Lincoln, Ne) Science Olympiad in High School, Mr. John Pierce (Milford, NE) of Southeast Community College, Profs. Tim Gay, Duane Jaecks, Paul Burrow, Herman Batelaan, Ilya Fabrikant and Dr. Orhan Yenen (University of Nebraska-Lincoln), Dr. A.L.D. Kilcoyne (Advanced Light Source, Lawrence Berkeley National Laboaratory) and Dr. John Furst (University of Newcastle at Ourimbah). And of course Les from the student machine shop at UNL. Thanks for making fun of everything I made, but also teaching me how to machine. I cannot thank these people enough, and some more than others, for the preparation they have provided me.

The fruitful scientific discussions and generally easy-going working style was one of the greatest things about the ANU and the Centre for Antimatter-Matter Studies or CAMS. I learned a lot from my fellow students: Ryan Weed, Adric Jones, Alan Hayes, Emma Anderson, Colin Campbell, Wade Tattersall, Prasanga Palihawadana, Luca Chiari, Jacob Hughes, Peter Caradonna, Roisin Boadle and Jason Roberts. The postdocs; Casten, Dan, Simon and David for the excellent physics discussions. Everything from what not to do, to how to teach and communicate to a variety of people with different backgrounds, even within physics.

My theoretical godfather, Prof. Bob McEachran. Theory night, that is wine on wednesday evenings, is now a tradition which I will endeavor to continue elsewhere. Bob kept us in-line and was an invaluable resource reminding everyone of the quantum mechanics we all had forgotten.

My advisors. Prof. Stephen Buckman was the best. We nearly always came to the same conclusion and could rapidly come to a compromise. Assoc. Prof. James Sullivan, thanks for checking on me every day, even when I didn't need it, but perhaps the most important thing, taking a break for beer club on Friday afternoons. Prof. Michael Brunger, thanks for being mellow with the occasional jab.

My wife, Imogen, for dealing with the long nights in front of the computer pounding away at the keyboard. I could not have finished my thesis without the support of my wonderful wife. And to my extended family, Anna Bell, Tom and Ralph for providing support during the busy time surrounding the writing of this thesis.

My success was made possible by these individuals and organisations.

Abstract

Low-energy positron scattering has been conducted for over 40 years and large discrepancies (>20%) in the measured cross sections have plagued both experimental and theoretical results. The advent of the Surko buffer-gas trap has provided for sufficiently large numbers of positrons, with previously unmatched angular and energy distributions, which has allowed for the measurement of absolute cross sections with absolute uncertainties of less than 10%. Continual improvement of the experimental techniques has allowed for the separation of the partial scattering channels. These results are crucial for testing our theoretical understanding of the scattering process and for modeling of positron transport in complex systems.

The experiments reported in this thesis used a scattering apparatus which incorporated a radiative ^{22}Na source of positrons that were moderated using solid neon and cooled further by a Surko buffer-gas trap. Those positrons were subsequently scattered from various atomic and molecular gases in a cylindrical scattering cell. Scattered and unscattered positrons emerging from the scattering cell were energy analysed with a retarding potential analyser to determine their energy loss, which enabled the determination of various scattering cross sections.

Absolute elastic differential, grand total, total elastic, total inelastic and positronium formation scattering cross sections for energies between 1 and 200 eV are presented for a number of atomic and molecular species. Where possible, knowledge of the experimental limitations are combined with theoretical calculations to estimate the amount of the angular scattering missed due to the finite angular resolution of the experiment. Comparison of both grand total and partial total cross sections are compared to a number of theoretical calculations and previous experimental results, again where possible.

A rotating electric field, or 'rotating-wall' electrode, was implemented to increase the central density of the positron beam. The operational phase space was explored in the context of the standard running parameters of this Surko-trap system used for atomic and molecular scattering experiments. Mechanisms for compression are reviewed in the context of applicability to the operational parameters of the trap and in the understanding of the dominant mechanism. The limitations in the implementation are discussed in regard to scattering experiments from atoms and molecules.

Finally, the conclusions of this work are summarised, and future research directions briefly noted.

Contents

Chapter 1

Introduction

The use of positrons is now common in humanity's exploration of the nature of the physical world. Scattering experiments from thermal (energies of ~25 meV) to relativistic velocities are routinely carried out in various laboratories using apparatus ranging in size from a tabletop to large storage rings. Positrons have found applications in medical physics, where their unique properties allow functional imaging of biological processes, and in material science. It has been less than 100 years since the prediction and discovery of the positron, with a significant amount of work being performed during that time in observing, understanding and controlling positrons for use in the exploration of antimatter collisions with matter.

The simplest comparison between electron and positron scattering from atomic or molecular targets is in the elastic scattering channel. The elastic scattering problem for positrons and electrons differs due to their opposite charge, typically resulting in very different scattering cross sections. The exchange interaction in which an incident electron takes the place of an atomic or molecular target-electron leads to rich effects on the scattering dynamics whereas the positron does not undergo this interaction as it is distinguishable from an electron. At high collision energies, the grand total scattering cross section for electrons and positrons converge [1] since the interaction potential between the positron-target and electron-target are now dominated by the same potential [2].

Experimental investigations of low-energy positron scattering have been limited due to low moderation efficiencies and large energy spreads, until the development of the Surko buffer-gas trap [3] coupled with a high-efficiency neon moderator [4]. That combination provides a system with high positron flux and low energy width allowing measurements of channel-resolved scattering, such as electronic and vibrational excitations.

This work is part of a program aimed at exploring the fundamental interaction of positrons with atoms and molecules. The variety of targets and measurements considered is a reflection of the wealth of possibilities in positron scattering due to the complexity of the interaction. The ability to determine absolute scattering cross sections, both differential and total, provides a strict test for the validity of modern theoretical calculations.

In positron scattering from atomic species, below the positronium formation threshold, only the elastic scattering channel is open. Measurements of the grand total scattering cross section, and theoretical calculations below this threshold, are now at the benchmark level for the case of positron-helium scattering [5]. However, there is significant theoretical

difficulty in calculating positron-atom collisions once the positronium formation channel is open. The formation of a neutral, bound, state of a positron and an electron leads to a scattering problem which is inherently two-centred, since the positronium atom has internal structure. This difficulty has required calculations of greater complexity to treat the two centres [6].

A series of recent measurements of positron scattering from the noble gases has been compared to theoretical calculations, which do not consider the two centre nature of the scattering problem [5,7–9]. General agreement was found below the positronium formation threshold between experiment and theory. For example, comparison of elastic differential scattering cross sections for Krypton [8] and Xenon [9] have shown general agreement below the positronium formation threshold, but deviate above the threshold where the experiment appears to be more forward peaked than most theoretical work. Recently, McEachran and Stauffer [10] modified the relativistic optical potential method simulating positronium formation. A comparison of the available theoretical and experimental angular differential cross sections for positron-helium scattering is reviewed, in light of experimental limitations, in Chapter 5.

The binding of positrons to atomic targets is of great interest both experimentally and theoretically, due to their, in principle, similarity to temporary negative ion resonances in electron scattering. There have been many predictions of binding to a number of atomic targets [11, 12], but only a few of those studies have considered binding to excited states [13, 14]. Chapter 6 covers a search for recently predicted resonances, due to the presence of a positron bound to a doubly-excited state of helium.

Many of the theoretical methods used to describe positron- or electron-atom collisions have been extended to positron-molecule collisions. This has provided a wealth of results for the most fundamental of molecular targets, H_2. A number of theoretical methods have been applied to positron-molecular hydrogen scattering: such as the Complex Model Potential [15], Single-Centre Convergent Close Coupling (CCC) Method [16], Swinger Multichannel [17], and R-Matrix Approach [18]. Despite this large body of work, significant discrepancies occur at low energies. Chapter 7 compares new measurements of positron scattering from molecular hydrogen to the results from various calculations at the grand total, elastic differential and total elastic, and total inelastic level, with particular attention paid to scattering energies below the positronium formation threshold.

Channel coupling in scattering physics is a well established phenomenon. One manifestation of such channel coupling occurs in the elastic scattering cross section, due to the onset of an inelastic scattering channel, and is referred to as a Wigner Cusp [19]. A number of examples can be found for cusps in electron scattering which led to the search for cusps in positron scattering where, positronium formation could, in principle, lead to a feature in the elastic scattering channel. Recently, a series of cusps were observed in the total elastic scattering cross section for positrons scattering with the noble gases [20]. No trend was, however, observed in the magnitude or width of the cusps and no theoretical work has been able to reproduce these results as yet. Chapter 8 discusses the results of

a search for Wigner Cusps in molecules isoelectronic with Neon: Water (H_2O), Ammonia (NH_3) and Methane (CH_4), and in the molecule isoelectronic with Helium, i.e. H_2.

Positron beams generated in a Surko style buffer gas trap can be tailored using a 'rotating-wall' or RW electrode. A radio-frequency (RF) electric field couples to positrons in the potential trap preferentially driving the positrons toward the electrodes axis of symmetry and thereby effectively compressing the positrons radially. Two regimes have been found which describe the compression mechanism, and they are reviewed in comparison to the operational parameters of the current experimental apparatus in Chapter 9.

Chapter 2

Overview of Positron Scattering

This chapter initially briefly reviews the channel's that are available when a positron (or an electron in most cases) collides with an atom or molecule. It also includes a short comparison of positron versus electron scattering behaviour. Finally, a review of the theoretical approaches that are currently employed to describe positron-atom and positron-molecule scattering is given. Most of that discussion is limited to helium and molecular hydrogen, reflecting the experimental data presented in later chapters.

Introduction

Positron collisions with atoms and molecules have the same general scattering channels available as electrons (2.2-2.6) with a few notable exceptions (2.1 and 2.7):

$$
\begin{aligned}
e^+ + AB(\nu, J) &\rightarrow n\gamma + AB^+(\nu, J), \text{Annihilation } (\sigma_{n\gamma}), && (2.1)\\
&\rightarrow e^+ + AB(\nu, J), \text{Elastic } (\sigma_{ICS}), && (2.2)\\
&\rightarrow e^+ + AB(\nu', J'), \text{Ro-vibrational Excitation } (\sigma_{Vib}), && (2.3)\\
&\rightarrow e^+ + A + B, \text{Dissociation } (\sigma_{Diss}), && (2.4)\\
&\rightarrow e^+ + AB^*, \text{Electronic Excitation } (\sigma_{Exc}), && (2.5)\\
&\rightarrow e^+ + AB^+ + e^-, \text{Direct Ionisation } (\sigma_{Ion}), && (2.6)\\
&\rightarrow Ps(e^-e^+) + AB^+, \text{Positronium Formation } (\sigma_{Ps}). && (2.7)
\end{aligned}
$$

However, the different interaction potentials in positron and electron scattering can lead to large differences in the energy dependence of the cross sections below a few hundred electron volts. The exploration of differences between electron and positron scattering cross sections, in this energy range, provides insight into the fundamental nature of scattering physics. The focus of this discussion will be on processes (2.1) through to (2.7), but this list is not exhaustive. The underlying mechanisms or interactions which cause the differences between electron and positron scattering are summarised in table 2.1. Only the polarisation potential is the same when scattering with a positron or electron. The lack of the exchange interaction in positron scattering significantly reduces the number of accessible electronically excited states, thereby decreasing the observed complexity of,

or amount of structure in, the energy loss spectrum, see §2.4. Positronium formation, however, provides a scattering channel to rival the complexity of the exchange interaction. It is the goal of low-energy positron scattering to determine the magnitude and energy

Table 2.1: e^+ and e^- interaction comparisons.

	Electrons	Positrons
Static Potential	attractive	repulsive
Polarisation Potential	attractive	attractive
Electron Exchange	✓	✗
Positronium Formation	✗	✓
e^-,e^+ Annihilation	✗	✓

dependence of scattering cross sections, in an effort to understand the interactions of the positrons in various media. Much of the earlier experimental and theoretical work has been summarised in a number of review articles and books, e.g. [21–23], to which the reader is referred for more details.

2.1 Annihilation

The annihilation channel is unique to antimatter collisions and provides a powerful tool for the investigation of antimatter (positron) scattering. When a positron and electron collide, or their wavefunctions overlap sufficiently, and annihilation occurs, a number of γ rays are produced with energies summing to the rest mass of the electron, the positron and the collisional kinetic energy. These γ rays are not readily absorbed in most materials and thus can be transported to appropriate detectors. This relative ease of detection provides a signal which can be related to atomic and molecular parameters, as was first shown in positron scattering from gases [24].

The spins of the positron and electron can be parallel or anti-parallel in the annihilation process, leading to an odd or even number of annihilation photons respectively. Dirac derived the fully relativistic cross section for the singlet spin state [25],

$$\sigma_{2\gamma} = \frac{4\pi r_o^2}{\gamma+1}\left[\frac{\gamma^2+4\gamma+1}{\gamma^2-1} ln\left(\gamma+\sqrt{\gamma^2-1}\right) - \frac{\gamma+3}{\sqrt{\gamma^2-1}}\right], \tag{2.8}$$

where r_o is the classical electron radius and γ is the Lorentz factor. However, the non-relativistic approximation is often sufficient. The 2-γ annihilation cross section can be written in terms of $\sigma_{2\gamma}$ [26],

$$\sigma_a = \sigma_{2\gamma} Z_{eff}, \tag{2.9}$$

where Z_{eff} is a dimensionless parameter. Z_{eff} represents the effective number of electrons allowing for complex interactions, and in molecular systems where additional degrees of freedom are present, can have a value up to 10^7. The annihilation rate, Γ, for positron collisions with atoms or molecules can be written in terms of the Dirac 2γ annihilation

cross section,

$$\Gamma = \sigma_a \upsilon n = Z_{eff} \rho \pi c r_o^2, \tag{2.10}$$

where ν is the velocity of the positron, c is the speed of light, and n and ρ are the number density of the gas. Note that Z_{eff} has been calculated for a number of atomic and molecular targets [27, 28]. The 3γ cross section is also considered negligible in most experiments having been shown to be 370 times smaller than the 2γ cross section [29]. In the case of the present experiment, the 2γ annihilation cross section is also considered negligible as it is up to 5 orders-of-magnitude smaller than the grand total scattering cross section at low energies [21].

2.2 Elastic Scattering

At very large distances neither the electron nor the positron are attracted or repelled by a neutral atom or molecule. When a positron or an electron approach an atomic or molecular target, they begin to polarise the target atom or molecule. Eventually, as the projectile gets closer still, the amount of screening of the heavy nucleus decreases due to the polarisation of the target and the static Coulomb interaction dominates and is attractive for electrons and repulsive for positrons. The interplāy of the polarization and static potentials tends to dominate the scattering of positrons and electrons. Knowledge of these potentials allows for the calculation of the scattering cross section and measurement of these cross sections provides insight into the scattering potentials. Experimental aspects of this thesis will be discussed in the following Chapter.

Elastic scattering does not change the internal state of the target and can be defined as,

$$e^+ + A \rightarrow e^+(\theta, \phi) + A, \tag{2.11}$$

where no excitation of the internal structure of A occurs (remembering that the e^+ has no internal structure). The elastic scattering cross section can be defined for an incident beam of flux, f_i, or current of particles. A detector is assumed to be placed far from the interaction region at polar angles θ and ϕ defining the solid angle $d\Omega$. The proportionality constant relating the number of scattered n_s positrons into dΩ to the incident flux, f_i, is $d\sigma(\theta, \phi)$ or,

$$d\sigma(\theta, \phi) = \frac{n_s(\theta, \phi) d\Omega}{f_i}. \tag{2.12}$$

The elastic differential scattering cross section is then written as,

$$\sigma_{DCS}(\theta, \phi) = \frac{d\sigma(\theta, \phi)}{d\Omega} = \frac{n_s(\theta, \phi)}{f_i}, \tag{2.13}$$

where $n_s(\theta, \phi)$ contains the angular scattering information and f_i is the incident flux. The integral elastic cross section (ICS) or total elastic scattering cross section can be

determined by integrating the angular dependence,

$$\sigma_{ICS} = \int \sigma_{DCS}(\theta, \phi) d\Omega. \tag{2.14}$$

Azimuthal symmetry allows the above integral to be written in terms of a single scattering angle,

$$\sigma_{ICS} = 2\pi \int \sigma_{DCS}(\theta) sin\theta d\theta. \tag{2.15}$$

Combining all of the possible scattering channels from (2.1-2.7) above, the grand total scattering cross section or GTCS can be written as,

$$\sigma_{GTCS} = \sigma_{n\gamma} + \sigma_{ICS} + \sigma_{Ro-vib.} + \sigma_{Dissociation} + \sigma_{Excitation} + \sigma_{DirectIonisation} + \sigma_{Ps}, \tag{2.16}$$

where each term is a function of the incident positron energy. In scattering from atoms, the annihilation and elastic scattering channels are the only open channels below the positronium formation threshold. As previously discussed, the cross section for annihilation can be considered to be negligible. Thus, a measurement of the grand total scattering cross section below the positronium formation threshold consists of only the elastic scattering channel and is equivalent to the total elastic cross section,

$$\sigma_{ICS} = \sigma_{GTCS}, \text{ for } E < E_{Ps}. \tag{2.17}$$

If the first electronic excitation energy is above the positronium formation threshold, then the total elastic scattering cross section is equivalent to the grand total scattering cross section minus the positronium formation cross section,

$$\sigma_{ICS} = \sigma_{GTCS} - \sigma_{Ps}, \text{ for } E < E_{1^{st}Exc}. \tag{2.18}$$

The grand total scattering cross section for scattering from molecules contains three more terms, due to vibrational and rotational modes and dissociation,

$$\sigma_{GTCS} = \sigma_{ICS} + \sigma_{Diss} + \sigma_{Exc.} + \sigma_{Ion} + \sigma_{Ps} + \sigma_{Rot} + \sigma_{Vib}. \tag{2.19}$$

It is often difficult to separate the vibrational and rotational channels due to their small excitation quantum which leads to the definition of a 'quasi' total elastic cross section defined as the sum of the elastic, vibrational and rotational channels,

$$\sigma_{QICS} = \sigma_{ICS} + \sigma_{Rot} + \sigma_{Vib}, \text{ with } \sigma_{ICS} \gg \sigma_{Rot} + \sigma_{Vib}. \tag{2.20}$$

Care must be taken when comparing σ_{QICS}. The ground electronic state of a molecule has a distribution of rotational and vibrational states and the population of these states is temperature dependent [30], whereas theoretical calculations consider only the ground state (i.e. electronic, rotational and vibrational quanta are all in their lowest energy states).

2.3 Inelastic Scattering

Inelastic scattering is any scattering process which the incident particle's kinetic energy is not conserved. Often it is thought of as any scattering processes which transfers energy from the projectile to an internal state of the target, but it can also lead to breakup of the target atom or molecule. In the case of positron scattering, there is an additional channel which results in a bound state of the positron and electron, or positronium formation. The various inelastic scattering channels are reviewed below.

2.3.1 Electronic Excitation

The process of electronic excitation of atoms or molecules involves a target electron being promoted to a higher-lying (in terms of energy) bound state via excitation by a positron (in this case) and can be denoted by,

$$e^+ + A \rightarrow e^+ + A^*, \tag{2.21}$$

where A^* denotes the excited target. Due to the lack of the exchange interaction, and because the spin-orbit interaction for positrons is negligible, a positron can only excite singlet states from a singlet ground state of an atom or molecule. Singlet to triplet transitions are dipole forbidden ($\Delta l \neq 1$) requiring a non-dipole (i.e. quadrupole) interaction which is not available for positrons. Atomic targets, such as helium, are in a singlet ground state at room temperature ($\sim$ 300K), but molecular targets, such as H_2, will be rotationally and vibrationally excited depending on the molecular structure. The population of rotational and vibrational levels of the ground electronic state are temperature dependent and follow a Boltzmann distribution in the simplest case. Excitation between molecular bands or electronic states, in positron scattering, is the same as for atoms with additional structure due to the vibrational and rotational states. The lack of non-dipole interactions between positrons and atomic and molecular targets decreases the number of possible states which can be excited, allowing for separation of the various channels in many cases.

2.3.2 Positronium Formation

$$e^+ + A \rightarrow Ps(e^+e^-) + A^+. \tag{2.22}$$

The bound state between a positron and an electron, or positronium, has a binding energy of 6.8 eV or half a Rydberg (13.6 eV). This bound state has two configurations; singlet and triplet positronium (with lifetimes of 125 ps and 142 ns, respectively) and decaying to 2 or 3-γ rays, respectively, as discussed previously in §2.1. The formation threshold for positronium is therefore 6.8 eV below the first ionisation potential of the target,

$$E_{Ps} = E_{IP} - 6.8\,eV. \tag{2.23}$$

Positronium has a finite lifetime and decays to two or three gamma rays, allowing for the measurement of the positronium formation cross section via measuring the annihilation γ rays versus the number of incident positrons on a target gas of atoms or molecules (while taking into account detection efficiency and solid angle). It is also possible to measure the number of ions produced as a function of the incident positron energy; as below the first ionisation potential the only mechanism for ionisation is positronium formation. Measuring the number of positrons lost due to positonium formation is another method, which will be discussed in more detail in Chapter 4.

2.3.3 Direct Ionisation

$$e^+ + A \rightarrow e^+ + A^+ + e^-. \tag{2.24}$$

A positron can directly ionise an atom or molecule, in the same manner as an incident electron, if its incident energy is equal to or greater than the ionisation potential of that atom or molecule. In this case, the outgoing electron and positron do not form the positronium bound state, but instead the excess energy is shared amongst the positron, electron and residual ion. A positron can also ionise a target by annihilation or by removing an electron to form positronium, which is discussed in the previous section.

2.3.4 Ro-vibrational Excitation

$$e^+ + AB(E, \nu') \rightarrow e^+ + AB(E', \nu''). \tag{2.25}$$

The vibrational spectrum of a molecule is directly related to its molecular structure. For diatomic molecules the vibrational modes can be described using a harmonic oscillator approximation, whereas for polyatomic molecules a full treatment of the vibrational spectrum requires Group theory. However, the number of modes, or fundamental modes, can be determined simply by calculating the number of degrees of freedom, $3N - 6$, where N is the number of atoms in the molecule [30]. Each electronic state, described above, has associated rotational and vibrational structure [31]. In addition to the fundamental modes, overtones and combination bands are also possible.

2.4 Comparison to Electron Scattering

The positron is the antiparticle of the electron and thus has the same mass, but opposite charge. Therefore, you might expect some similarity in the scattering cross sections. However, in scattering with atoms or molecules, it is the electronic structure of these targets which also helps determine the fine detail of the collision dynamics. The exchange interaction, or the ability of the incident electron to change places with the target electron because they are indistinguishable, plays a key role in the scattering dynamics for electrons, but is absent in the case of positron scattering because the positron is distinguished from the electron by its charge. The spin-orbit interaction is small for positron scattering

because the positron is positively charged and can not get close enough to the nucleus to interact significantly, unlike the electron, on high-Z targets.

2.4.1 Grand Total Scattering Cross Section

A comparison of electron and positron scattering, at the grand total cross section level, for helium by Kauppila *et al.* [32] is shown in figure 2.1. The grand total scattering cross section for electrons and positrons tends to the same value at high energies but diverges at low energies. A Born expansion of the forward scattering amplitude yields similar terms for the electron and positron at high incident energies. The interaction potential for the, electron-atom and positron-atom cases, are quadratic in both cases [2,21]. At low energies,

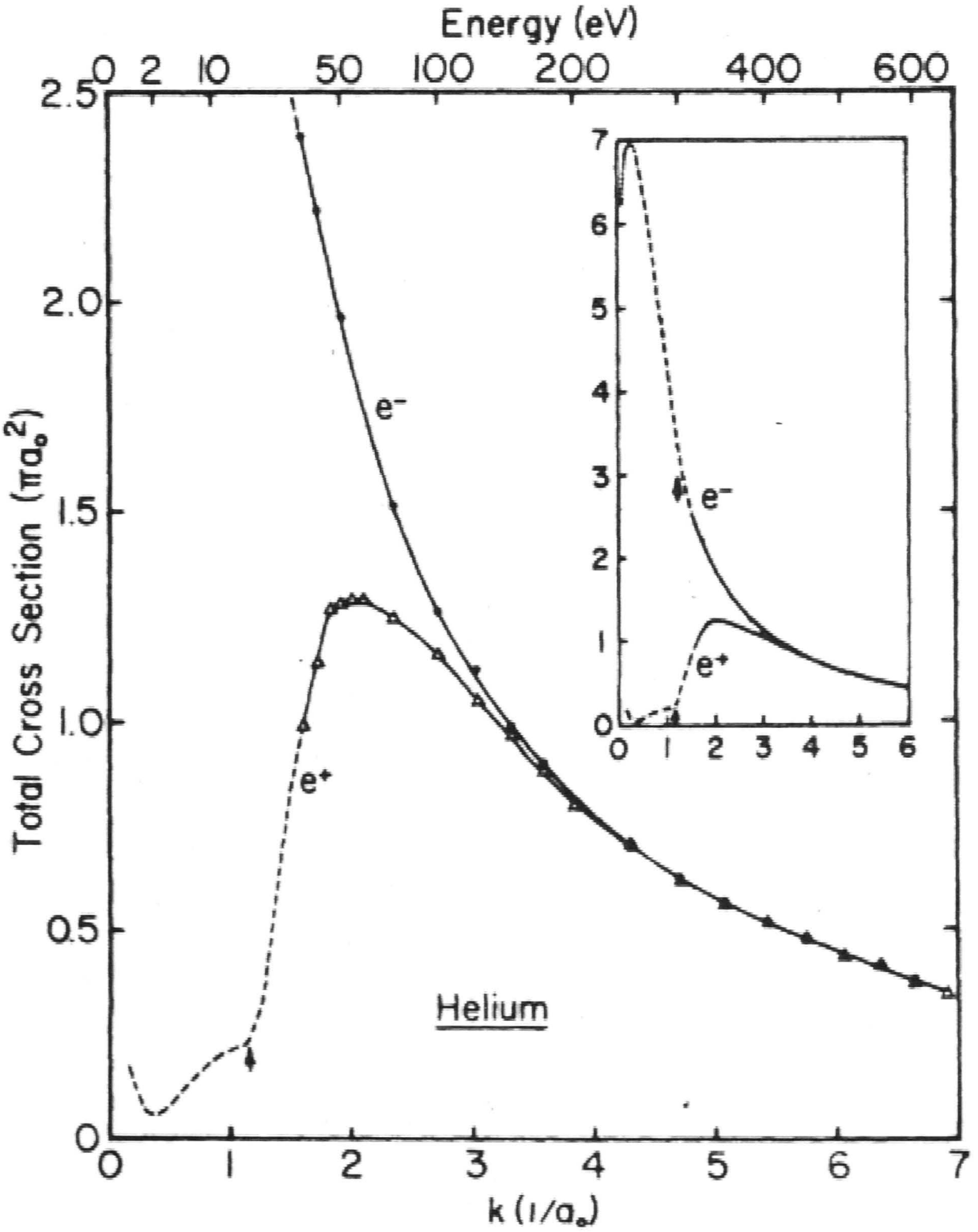

Figure 2.1: An early comparison of the electron and positron grand total scattering cross section, results from Kappila *et al.* [32] and references therein. The dashed line at low energies are theoretical results from Stein *et al.* [33].

the elastic channel for positron scattering is more than an order-of-magnitude smaller than

for the electron case. As the scattering energy increases above the RamsauerTownsend (R-T) minimum, the positron cross section increases in magnitude as the electron scattering cross section decreases. A R-T minimum occurs due to the s-wave phase shift passing through $n\pi$ at low scattering energies. At higher energies, inelastic channels, such as the positronium and direct ionisation scattering channels, increase the positron GTCS to near that of the electron scattering cross section, and they converge by 200 eV.

2.4.2 Electronic Excitation

When an electron electronically excites an atom or molecule it can do so via two mechanisms; direct and exchange. This provides a large number of available excitations resulting in a rich energy loss spectrum. The lack of the exchange interaction in the positron case limits the number of possible excited states, thus reducing the complexity of the excitation spectrum.

A comparison of positron measurements of electronic excitation from atomic and molecular states, although still quite limited in scope, has shown that the magnitude of excitation is similar [34]. This is reasonable when considering the excitation of these states is dominated by the dipole interaction. In principle they may be very similar away from resonant structures in electron scattering, due to negative ion resonances [35] for example.

In both cases, electron and positron excitation, there is the possibility that the excited state may support a bound state. Temporary bound states or negative ions are numerous in electron scattering and drive many chemical processes, but the temporarily bound positron is much more elusive. A search for resonance structure due to the existence of temporary binding of a positron to an excited state of helium is discussed in Chapter 6.

2.4.3 Vibrational and Rotational Excitation

Vibrational and rotational excitation of molecules is dominated by the dipole interaction [36]. Thus the excitation of vibrational modes via positron or electron impact is likely to be very similar in magnitude in energy regions void of resonant structure. Fundamentally, it is the dipole matrix element which determines the magnitude of the excitation. Comparisons between mode-specific electron- and positron-vibrational excitation have shown remarkable agreement for CF_4 [37], whereas previous integral measurements for the 0-1 mode in CO differed [38], and this is likely due to a resonance feature in the electron case.

The most investigated, positron-induced vibrational excitations, have been in large molecules where Vibrational Feshbach Resonances are observed in the annihilation rate as function of incident positron energy [39]. Here the same vibrational modes which are excited with infrared (IR) photons are seen in the measurement of Z_{eff} under positron excitation [40].

2.4.4 Ionisation

The ionisation of an atom or molecules by electrons begins when the energy of the incident particle exceeds the first ionisation potential of the target. Above this energy, the outgoing electrons and the residual ion share the collision energy minus the ionisation energy. The positron, however, can ionise an atom or molecule below the ionisation potential via the process of forming positronium. Hence the term 'direct' ionisation versus positronium formation. In direct ionisation the outgoing positron, electron and residual ion share the residual energy. When ionisation occurs via positronium formation, the outgoing Ps atom and the residual ion energy is shared between the residual ion and neutral Ps which subsequently annihilates. Thus for all of the ionisation potentials (IP) of a given target, atomic or molecular, there exists an associated positronium formation threshold occurring at 6.80 eV below the IP.

The direct ionisation and positronium formation cross sections have been measured for a number of atomic and molecular targets [22], with some of the most recent investigations being by Marler *et al.* [41, 42]. The total ionisation cross section has a threshold at the opening of the positronium formation channel and rises rapidly due to Ps formation. In general, the direction ionisation channel turns on more slowly and only overtakes Ps formation by $\sim$ 100 eV.

2.4.5 Exchange Interaction

An electron incident on an atom or a molecule can undergo the exchange interaction, where it takes the place of an electron in the atomic or molecular target. This process of replacing an electron is possible because the electrons are indistinguishable and leads to the excitation of triplet states from a singlet ground state, in the case of electronic-excitations, in which the spin of electrons are parallel rather than antiparallel in the ground state. A positron is distinguishable from an electron and thus the exchange interaction cannot occur in a collision of a positron with an atom or molecule. However, of course it is possible in collisions with anti-atoms and anti-molecules where the positron could exchange with a positron from the anti-atom or anti-molecule.

The only mechanism for the exchange interaction, involving positron collisions with atoms and molecules, requires a higher-order interaction involving positronium formation. When a positron is incident upon an atom or molecule with sufficient energy to form positronium, it removes an electron from the target to form a bound state. The outgoing positronium atom can then, in principle, undergo the exchange interaction, by exchanging the 'original' electron for another electron from the target.

2.5 Positron Scattering Theory

The goal of scattering theory is to solve or approximate the solution to the Schrödinger equation,

$$(H - E)\Psi = 0. \tag{2.26}$$

where Ψ is the wavefunction describing the configuration of the system. Generally, the time-independent nonrelativistic Schrödinger equation is considered for positron collision calculations, since the spin-orbit interaction is assumed to be small, and fast-dynamics (relativistic effects) are not being considered.

Consider scattering of a particle with an arbitrary potential $V(\mathbf{r})$, [43], which goes to zero faster than $1/r$ as $r \to \infty$. The Schrödinger is written in terms of the arbitrary potential,

$$\left[-\frac{\hbar^2}{2m}\nabla^2 + V(\mathbf{r})\right]\psi_{\mathbf{k}}(\mathbf{r}) = E\psi_{\mathbf{k}}(\mathbf{r}). \tag{2.27}$$

At infinity, the solution has the form of the unscattered and scattered wave,

$$e^{i\mathbf{k}\cdot\mathbf{r}} + f(\Omega)\frac{e^{ikr}}{r}, \tag{2.28}$$

where $f(\Omega)$ is the scattering amplitude. The cross section is now defined as for elastic scattering,

$$\sigma(\Omega) = |f(\Omega)|^2. \tag{2.29}$$

The following sections, in which atomic units are used throughout, describe methods which have been used to determine the basis sets for given approximate Hamiltonians, or provide approximate wave functions with a focus on solving the problem of positron scattering from helium or molecular hydrogen.

2.5.1 Partial-Wave Formalism

In the non-relativistic case, the elastic differential scattering cross section can be written as a single scattering amplitude $f(\theta)$ as,

$$\sigma(\theta) = f^*(\theta)f(\theta) = |f(\theta)|^2, \tag{2.30}$$

where

$$f(\theta) = \frac{1}{k}\sum_{l=0}^{\infty}(2l+1)T_l(k)P_l(cos\theta). \tag{2.31}$$

$P_l(cos\theta)$ is the Legendre Polynomial of order l and $T_l(k)$ is the T-matrix element which is complex. The scattering amplitude is a summation of an infinite series of partial waves in l, where l is a good quantum number and is the angular momentum of the positron in the frame of the atom. This summation reduces when the orthogonality of the Legendre Polynomials is considered,

$$\sum_{l'=0}^{\infty}\sum_{l=0}^{\infty} P_{l'}^*(cos\theta)P_l(cos\theta) = \delta_{l'l}. \tag{2.32}$$

The expression for the elastic differential scattering cross section can then be written as,

$$\sigma_{DCS}(\theta) = \frac{1}{k^2}\sum_{l=0}^{\infty}\sum_{l'=0}^{\infty}\left[1+(-1)^{l+l'}\right](2l+1)(2l'+1)T_l(k)T_{l'}^*(k)P_l(cos\theta)P_{l'}(cos\theta) \quad (2.33)$$

2.5.2 Polarised Orbital Approximation

The Polarised Orbital Approximation or POA was originally introduced by Temkin [44] and was used initially to describe electron scattering from atomic hydrogen [45]. It was extended to positron scattering from the noble gases by McEachran [46].

The POA considers the scattering problem in two parts, calculating the perturbed bound-state wave function, or polarised orbital, and calculating the scattered wave function. The positron is considered at a fixed position (the adiabatic approximation) and the polarised orbital is the atomic wavefunction perturbed by the presence of the positron. The Hamiltonian for the system with a stationary positron is,

$$H_{ad} = H_0 + V, \quad (2.34)$$

where H_0 is the Hamiltonian for the atom,

$$H_0 = -\frac{1}{2}\sum_{i=1}^{N}\nabla_i^2 - \sum_{i=1}^{N}\frac{Z}{r_i} + \sum_{i,j=1,i<j}^{N}\frac{1}{r_{ij}}. \quad (2.35)$$

The interaction potential is given as,

$$V = \frac{Z}{x} - \sum_{i=1}^{N}\frac{1}{|\mathbf{r}_i - \mathbf{x}|}, \quad (2.36)$$

where the total wave function is written as a determinant of component wave functions,

$$\Psi = \frac{1}{\sqrt{N!}}\det|\psi_1 \ldots \psi_N|, \quad (2.37)$$

where the component wave functions are represented by,

$$\psi_i(\mathbf{r}_i, \sigma_i, \mathbf{x}) = \phi_i^0(\mathbf{r}_i, \sigma_i) + \phi_i^1(\mathbf{r}_i, \sigma_i, \mathbf{x}). \quad (2.38)$$

Note that in equation 2.38 σ_i is the spin coordinate of the electron. The component wave function is in two parts, the unperturbed component, ϕ_i^0 , and the component, ϕ_i^1, perturbed by the potential V. Adjustment of the perturbation can be done by changing the fixed position of the positron, $\mathbf{x}$. The polarised orbitals are obtained by minimizing $\langle\Psi|H_{ad}|\Psi\rangle$ where the potential V is treated as a first-order perturbation [46]. This method has been used to calculate elastic differential scattering cross sections below the positronium formation threshold [10], and its results are compared to the current experimental results in Chapter 5.

2.5.3 Relativistic Optical Potential

The Relativistic Optical Potential method involves solving the integral form of the Dirac scattering equation [47]. The resulting spin-dependent T-matrices are written as,

$$T_{l_2}^{\pm}(k_0) = \frac{1}{2i}\left[e^{2i\bar{\delta}_{l_2}^{\pm}} - 1\right], \tag{2.39}$$

where spin-up is (+) and spin-down (−). The direct and spin-flip scattering amplitudes are written in terms of the T-matrix [47],

$$f(\theta) = \frac{1}{k_0}\sum_{l_2=0}^{\infty}\left[(l_2+1)T_{l_2}^{+}(k_0) + l_2 T_{l_2}^{-}(k_0)\right] P_{l_2}(cos\theta), \tag{2.40}$$

$$g(\theta) = \frac{1}{k_0}\sum_{l_2=0}^{\infty}\left[T_{l_2}^{-}(k_0) - T_{l_2}^{+}(k_0)\right] P_{l_2}^{1}(cos\theta), \tag{2.41}$$

where $P_{l_2}(cos\theta)$ and $P_{l_2}^{1}(cos\theta)$ are the Legendre and associated Legendre polynomials. The differential scattering cross section is,

$$\sigma(\theta) = |f(\theta)|^2 + |g(\theta)|^2. \tag{2.42}$$

The cross section can be deconstructed into two components, with one corresponding to pure elastic scattering or the real component of the phase shifts, and another corresponding to inelastic scattering or the imaginary part of the phase shifts [47]. This method has been extended to incorporate the positronium formation channel by lowering the ionisation threshold [10],

$$\sigma^{Ps}(k^2) = \sigma^{inel,\Delta}(k^2) - \sigma^{inel}(k^2), \tag{2.43}$$

where the Δ term corresponds to the reduced ionisation potential. A relation of these theoretical elastic differential cross sections are compared to experimental results for Helium in Chapter 5.

2.5.4 Convergent Close Coupling Method

Single-Centre

The Single-Centre approach used for positron-atom collisions [48] has recently been applied to molecular hydrogen, by considering a fixed internuclear separation (R = 1.4 a_o) and writing the total Hamiltonian [16],

$$H_T = H_1 + H_2 + V_{12} + \frac{1}{R}. \tag{2.44}$$

where $1/R$ is the internuclear Coulomb repulsion, and V_{12} is the interaction between the two electrons. In addition we define,

$$H_i = -\frac{1}{2}\nabla_i^2 + V(\mathbf{r}_i, \mathbf{R}), i = 1, 2, \tag{2.45}$$

where the electron-nuclei potential is,

$$V(\mathbf{r}_i, \mathbf{R}) = -\frac{1}{|\mathbf{r}_i - \mathbf{R}/2|} - \frac{1}{|\mathbf{r}_i + \mathbf{R}/2|}. \tag{2.46}$$

The target wave function is built from Laguerre one-electron orbitals. For a molecule with N electrons, the target must satisfy,

$$\langle \Phi_i^N | H_T | \Phi_j^N \rangle = \epsilon_j^N \delta_{ij}. \tag{2.47}$$

The T-matrix is obtained by transforming the body-frame Schrödinger equation into a set of coupled Lippmann-Schwinger equations,

$$\begin{aligned} \langle \mathbf{k}_f \Phi_f^{(N)} | T^{(N)} | \Phi_i^{(N)} \mathbf{k}_i \rangle &= \langle \mathbf{k}_f \Phi_f^{(N)} | V | \Phi_i^{(N)} \mathbf{k}_i \rangle \\ &+ \sum_{n=1}^{N} \int dk \frac{\langle \mathbf{k}_f \Phi_f^{(N)} | V | \Phi_n^{(N)} \mathbf{k} \rangle \langle \mathbf{k} \Phi_n^{(N)} | T^{(N)} | \Phi_i^{(N)} \mathbf{k}_i \rangle}{E^{(+)} - k^2/2 - \varepsilon_n^{(N)}}. \end{aligned} \tag{2.48}$$

A partial-wave expansion is used to obtain the T-matrix, which is then utilised to obtain the scattering amplitudes in the body-frame, f_{fi}^B. The angular differential scattering cross section is now obtained by transforming from the body-frame to the laboratory-frame, via rotation by the Euler-angle β,

$$\frac{d\sigma_{fi}}{d\Omega} = \frac{1}{8\pi^2} \int |f_{fi}^{(L)}(\beta)|^2 d\beta. \tag{2.49}$$

A series of elastic differential scattering and integral cross section calculations [16] for molecular hydrogen are compared to the present experimental results in Chapter 7.

Two-Centre

The formation of the positronium atom, which has internal structure, results in a scattering problem with two scattering centres. The Convergent Close Coupling or CCC method [49, 50], has been extended to a multiconfigurational two-centre approach allowing for the explicit inclusion of postronium formation [6].

In the case of positron scattering with helium the Hamiltonian is written as [6],

$$H = H_0 + \frac{2}{|\mathbf{R} + \rho/2|} - \frac{2}{|\mathbf{R} - \rho/2|} - \frac{2}{r_2} + \frac{1}{|\mathbf{R} - \rho/2 - \mathbf{r}_2|} - \frac{1}{\rho} - \frac{1}{|\mathbf{R} + \rho/2 - \mathbf{r}_2|}, \tag{2.50}$$

where

$$H_0 \equiv -\nabla_\rho^2 - \frac{1}{4}\nabla_R^2 - \frac{1}{2}\nabla_2^2, \tag{2.51}$$

is the free Hamiltonian. The two-centre approach is based on expanding the wave function

in terms of all channels about either centre, taking the Helium example specifically [6],

$$\begin{aligned}
\Psi &\approx \sum_{\alpha}^{N_\alpha} F_\alpha(\mathbf{r}_0)\psi_\alpha(\mathbf{r}_1,\mathbf{r}_2)\chi_{SM}^{e^+-He}(0,(1,2)) \\
&+ \sum_{\beta}^{N_\beta}\{\psi_\beta(\rho_1)\phi_{1s}(\mathbf{r}_2) \\
&\times \left[G_\beta^{p-Ps-He^+}(\mathbf{R}_1)\chi_{SM}^{p-Ps-He^+}((0,1),2)\right. \\
&+ \left. G_\beta^{o-Ps-He^+}(\mathbf{R}_1)\chi_{SM}^{o-Ps-He^+}((0,1),2)\right] \\
&- \psi_\beta(\rho_2)\phi_{1s}(\mathbf{r}_1)\left[G_\beta^{p-Ps-He^+}(\mathbf{R}_2)\chi_{SM}^{p-Ps-He^+}((0,2),1)\right. \\
&+ \left. G_\beta^{o-Ps-He^+}(\mathbf{R}_2)\chi_{SM}^{o-Ps-He^+}((0,2),1)\right]\}. \qquad (2.52)
\end{aligned}$$

Note that in equation 2.52 para-positronium is denoted by $p-Ps$ and ortho-positronium is denoted by $o-P$. The pseudo-states for the atomic target and the positronium atom are generated by diagonalising the Hamiltonians using a square-integrable orthogonal Laguerre basis,

$$\left(\frac{\lambda_l(n-1)!}{(2l+1+n)!}\right)^{1/2}(\lambda_l r)^{l+1}e^{-\lambda_l r}L_{n-1}^{2l+2}(-\lambda_l r). \qquad (2.53)$$

Then the T-matrix can be determined in momentum space for the coupled-channels,

$$\begin{aligned}
T_{\gamma'\gamma}(\mathbf{q}_{\gamma_\prime},\mathbf{q}_\gamma) &= V_{\gamma'\gamma}(\mathbf{q}_{\gamma'},\mathbf{q}_\gamma) \\
&+ \sum_{\gamma''}^{N_\alpha+N_\beta}\int\frac{d\mathbf{q}_{\gamma''}}{(2\pi)^3}V_{\gamma'\gamma''}(\mathbf{q}_{\gamma'},\mathbf{q}_{\gamma''})\mathcal{G}_{\gamma''}(q_{\gamma''}^2)T_{\gamma''\gamma'}(\mathbf{q}_{\gamma''},\mathbf{q}_{\gamma'}), \qquad (2.54)
\end{aligned}$$

where the two-particle Greens functions $\mathcal{G}$ describe the relative motion between the two centres [6]. The T-Matrix can then be used to determine the differential scattering cross section in the normal manner. A series of elastic differential scattering cross section results [6] are compared to the current experimental results in Chapter 5.

2.5.5 Stochastic Variational Methods

The Stochastic Variational Method or SVM is a modification of the variational method [51], which uses stochastic techniques to reduce the complexity of the problem [52]. The wavefunction is expanded into a diagonalized basis set of the Hamiltonian [53],

$$\Psi = \sum_{i}^{K} C_i\psi_{SM_s}\left(\mathbf{x},A^i\right) = \sum_{i}^{K} C_i G\left(\mathbf{x},A^i\right)\chi_{SM_s}, \qquad (2.55)$$

where A^i is the matrix of Gaussian exponents and $\mathbf{x}$ represents the co-ordinates of all the particles [54]. Explicitly correlated Gaussians (ECGs) contain the spatial part of the basis

wavefunction [54],

$$G\left(\mathbf{x}, A^i\right) = \exp\left(-\frac{1}{2}\sum_{\mu,\nu=1}^{N'-1} A^i_{\mu\nu}\mathbf{x}_\mu\mathbf{x}_\nu\right) = \exp\left(-\frac{1}{2}\mathbf{x}^\dagger A'\mathbf{x}\right). \tag{2.56}$$

where N' is the number of interacting particles [54]. The stochastic nature of the method comes from the optimisation of the exponents by trial and error providing for fast convergence [55]. This method was used to predict the energy of the bound state between a positron and a doubly excited helium atom [14], and an experimental search for resonance structure due to the existence of the predicted state is presented in Chapter 6.

2.5.6 Configuration Interaction

The Configuration Interaction, or CI, is a method of approximating the target wave function by expanding it as a linear combination of atomic states with single-particle position states [56]. The electron orbitals are written as a product of a radial function and a spherical harmonic in the usual manner. The atomic wave function is generated using Clebsch-Gordon coupling coefficients,

$$|\Psi; LS\rangle = \sum_{i,j} c_{i,j}\langle L_i M_i l_j m_j|LM_L\rangle\langle S_i M_{S_i}\frac{1}{2}\mu_j|SM_S\rangle \times \Phi_i(atom; L_i S_i)\phi_j(r_0), \tag{2.57}$$

where $\Phi_i(atom; L_i S_i)$ is an antisymmetric wave function with good L and S quantum numbers. This approach can require a large L_{max} or maximum angular momentum to provide good results. Usually, a different method was used to approximate or extrapolate $L_{max} \to \infty$ [57, 58]. A variant of this method is used to verify the existence of positron-atom bound states, found with the SVM approach with the specific example of positron binding to excited states of helium being explored in Chapter 6.

2.5.7 Many-body Theory

Unlike the theoretical techniques discussed thus far, many-body theory begins with the Dyson equation [12],

$$\left(H_0 + \Sigma_\epsilon\right)\psi_\epsilon = \epsilon\psi_\epsilon, \tag{2.58}$$

where ψ_ϵ is the (single) quasiparticle wave function for the positron, ϵ is its energy, and H_0 is the Hamiltonian for the zeroth approximation of the central-field. The dynamics of the many-bodies are contained in Σ_ϵ,

$$\Sigma_\epsilon\psi_\epsilon = \int \Sigma_\epsilon(\mathbf{r}, \mathbf{r}')\psi_\epsilon(\mathbf{r}')d\mathbf{r}', \tag{2.59}$$

where $\psi_\epsilon(\mathbf{r}')$ are the positron eigenfunctions for the target atom or molecule. The positron-atom or positron-molecule bound state is determined by calculating the diagonal matrix

element,

$$\left\langle \epsilon' \left| \Sigma_E^{(2)} \right| \epsilon \right\rangle = \sum_{\nu,\mu,n} \frac{\langle \epsilon' n|V|\mu\nu\rangle\langle\nu\mu|V|\nu\epsilon\rangle}{E - \epsilon_\nu - \epsilon_\mu + \epsilon_n + i0}, \tag{2.60}$$

where V is the electron-positron Coulomb interaction, ν is all intermediate states, μ is all electron states, n is all hole states, and $i0$ is an infinitesimal positive imaginary quantity. Binding can occur when this second order term is negative, $\epsilon_b = \epsilon_0 < 0$. The binding energy to ground and exited-state configurations is determined by ,

$$\Sigma = \zeta\Sigma^{(2)}, \tag{2.61}$$

where ζ is adjusted to reproduce known binding energies in Be, Mg, Zn, Cd, Cu, and Ag, for a ζ of 2.0, 2.4, 1.8, 1.7, 2.4, and 1.9, respectively [59].

2.5.8 R-Matrix Approach

The R-Matrix method divides configuration space into two regions. The interior region is usually defined as a sphere of radius a encompassing the target states' electron density. Considering the electron scattering case, although this can be generalised for positron scattering, the basis functions of the Hamiltonian are expanded as [60, 61],

$$\Psi_k^{N+1}(x_1...x_{N+1}) = \mathcal{A}\sum_{ij} a_{ijk}\phi_i(x_1..x_n)u_{ij}(x_{N+1}) + \sum_i b_{ik}\chi_i(x_1...x_{N+1}), \tag{2.62}$$

where $\mathcal{A}$ is the antisymmetrization operator, $u_{ij}(x_{N+1})$ are continuum orbitals and x_n are spatial and spin coordinates. The continuum orbitals are generated by orthogonalizing the target atomic or molecular orbitals. States or pseudostates of the atom or molecule are incorporated via ϕ_i. The multi-centre components described by χ_i are quadratically integrable functions (L^2 functions). Coefficients a_{ijk} and b_{ik} are obtained by diagonalizing the matrix of order M,

$$\langle \Phi_k^{N+1}|\hat{H}^{N+1} + \hat{L}|\Phi_{k'}^{N+1}\rangle = E_k\delta_{kk'}. \tag{2.63}$$

with $\hat{H}^{N+1}$ the $(N+1)$-electron Hamiltonian and $\hat{L}$ the Bloch operator [62]. The R-Matrix is built at the boundary between the inner and outer regions [60, 61],

$$R_{ij}(E) = \frac{1}{2a}\sum_k \frac{\omega_{ij}(a)\omega_{jk}(a)}{E_k - E}, \tag{2.64}$$

where E_k (or the R-matrix poles) are eigenvalues and ω_{ik},

$$\omega_{ik} = \underbrace{\langle \phi_i Y_{l_i m_i} \Xi_{\frac{1}{2}}}_{Channel} |\Psi_k^{N+1}\rangle. \tag{2.65}$$

$\Xi_{\frac{1}{2}}$ is the spin-$\frac{1}{2}$ function. Thus the R-Matrix is composed of a set of scattering channels that, if sufficiently complete, will describe the scattering complex. Comparison of R-Matrix

results for differential and integral elastic scattering cross sections for positron scattering from H_2 [63], is given in Chapter 7.

2.5.9 Schwinger Multichannel Method

The Schwinger Multichannel Method, or SMC, is based on the Schwinger Variational Technique, which has been used in electron-atom and electron-molecule collisions [64] and then extended to positron-molecule collisions [65]. This general method uses the Lippmann-Schwinger form of the Hamiltonian,

$$\Psi^{\pm}_{k_m} = S_{k_m} + G^{\pm}_{P} V \Psi_{k_m}. \tag{2.66}$$

where S_{k_m} is the regular solution and $G^{\pm}_{0}$ is the Greens function projected onto the ground state. The scattering amplitude is written as,

$$f\left(\vec{k_f}, \vec{k_i}\right) = -\frac{1}{2\pi} \sum_{mn} \left\langle S_{\vec{k_f}} | V | \chi_m \right\rangle (d^{-1})_{mn} \left\langle \chi_m | V | S_{\vec{k_i}} \right\rangle \tag{2.67}$$

where

$$d_{mn} = \left\langle \chi_m \left| Q\hat{H}Q + PVP - VG^{(+)}_{p} V \right| \chi_n \right\rangle. \tag{2.68}$$

For this method, $|\chi\rangle$ is the variational trial wavefunction, Q is the projection operator onto closed states, P is the projection operator onto open states, V is the interaction potential, and $G^{(+)}_{p}$ is the Greens function projected onto the P space [66]. This method does not require the trial wave function $|\chi\rangle$ to satisfy a particular set of boundary conditions and thus it can be expanded in an L^2 basis. However, the range must be constrained in order to limit the interaction region (or collision centres) to a cubic region about the centre-of-mass [66]. In principle any trial wave function can be employed and (generally) previously proven wave functions are used, such as those derived from the Hartree-Fock formalism for H_2 [66]. Results from the SMC method are compared to the current experimental results in Chapter 7.

2.5.10 Complex Model Potential

The Complex Model Potential method describes the interaction potential in terms of three components,

$$V(r) = V_{st.}(r) + V_{pol.}(r) + iV_{abs}(r), \tag{2.69}$$

where $V_{st.}(r)$ is the static potential, $V_{pol.}(r)$ is the polarisation potential and $V_{abs}(r)$ is the absorption potential. The static potential is determined from an averaged electron charge density,

$$V_{st.}(r) = \left\langle \frac{\mathbf{Z}}{|\mathbf{r} - \mathbf{b}|} \right\rangle - 4\pi \int_0^{\infty} \frac{\rho(r')}{r_>} r'^2 dr', \tag{2.70}$$

where ρ is determined from the software package GAUSSIAN. The polarisation potential used is,

$$V_{pol.}(r) = -D_4(r)\frac{\alpha_d}{2r^4} - D_6(r)\frac{\alpha_q}{2r^6} - D_8(r)\frac{\alpha_o}{2r^8}, \tag{2.71}$$

where α_d is the dipole polarisability, α_q is the quadrupole polarisability and α_o is the octopole polarisability. The functions D_{2n}, for $n = 2, 3, 4$, are used to ensure that $V_{pol.} \to 0$ as $r \to 0$. The absorption potential is defined as [67],

$$V_{abs.}(r) = -\frac{1}{2}\rho\bar{\sigma}_b v, \tag{2.72}$$

where v is the local speed of the positron and $\bar{\sigma}_b$ is the average binary collision cross section [67, 68]. Solving the radial Schödinger equation,

$$\left[\frac{d^2}{dr^2} - \frac{l(l+1)}{r^2} + 2[E - V(r)]\right] u_l(r) = 0, \tag{2.73}$$

provides the solution $u_l(r)$ for the a scattering energy of E and angular momentum l. The scattering phase shifts are determined considering a finite region, typically 10 Bohr radii from the molecular centre,

$$tan(\delta_l) = \frac{r_+ u_l(r) j_l(kr_+) - r_+ u_l(r_+) j_l(kr)}{r_+ u_l(r_+) n_l(kr) - r_+ u_l(r) n_l(kr_+)}, \tag{2.74}$$

where j_l and n_l are the spherical Bessel and Neumann functions respectively. The scattering amplitude is determined by [15],

$$f(\theta) = \frac{1}{2ik}\sum_{l=0}^{l_{max}}(2l+1)[e^{2i\delta_l}]P_l(cos\theta) + f_4(\theta) + f_6(\theta) + f_8(\theta), \tag{2.75}$$

where the scattering amplitudes: $f_4(\theta)$, $f_6(\theta)$ and $f_8(\theta)$ correspond to the dipole, quadrupole and octopole polarisation potentials. Once the scattering amplitude is determined for a given scattering energy, the required scattering cross section can be calculated in the normal manner. The results of Reid *et al.* [15] for molecular hydrogen, using this approach, are compared to the current experimental results in Chapter 7.

2.5.11 Discussion

The difficulties of positron scattering from atoms and molecules stem primarily from two issues; target complexity and the interaction of the positron atom and the residual ion. Multi-centre techniques have been developed to explicitly describe these complex interactions with the greatest success observed in positron scattering from the rare gases. Various *ad hoc* techniques, such as the complex model potential, have had limited success (H_2) and give some physical insight as to when threshold effects may be negligible and a more simplistic description is valid. Specific comparisons of theoretical work compared to experimental results is given in later Chapters.

Chapter 3

Experimental Details

The study of positron scattering with atoms and molecules requires a source of positrons with a controllable energy, and an energy distribution sufficiently narrow to discriminate scattering features as a function of the incident energy. The associated apparatus should also posses the ability to resolve angular scattering. Previous theses (e.g. [69, 70]) from the ANU group, as well as some remarks in the Introduction of this thesis, discussed the work done to date to develop various types of positron sources used in low-energy (1 - 200 eV) scattering experiments. An excellent summary of this can be found in Surko *et al.* [22] The positron source used for the present experiments provided a positron beam with a variable energy and narrow energy width, and this chapter reviews the operational techniques used for the scattering experiments presented using a Surko-style, buffer gas trap.

3.1 Introduction

A positron scattering apparatus is dependent on the production of positrons with sufficiently low kinetic energy that they can be guided and focused with reasonable electric and/or magnetic fields. The exploration of partial scattering cross sections, of both atomic and molecular targets, requires an energy distribution sufficiently small to discriminate between excitation thresholds. Radioactive sources provide positrons with a very large distribution in energy (hundreds of keV), requiring cooling or moderation before guiding becomes effective. A series of moderation techniques have been used throughout the history of positron scattering experimentation, as discussed in the introductory chapter, with much of this work focused on primary energies larger than 10 eV due to the resultant energy spread of the beam [71].

Experimental systems using transition metal moderators (W or Ni) provided positron beams with energy widths between 150 and 500 meV, but with moderation efficiencies of ~ 0.1 % or less [72]. They also require processing involving annealing of the moderator foil or mesh, but when cooled to liquid nitrogen temperatures they can produce beams with energy widths down to 40 meV [73]. The discovery of solid rare-gas moderators provided moderation efficiencies of up to 1 %, but with an energy width between 1 to 2 eV [4]. This energy width is too large to conduct energy resolved scattering experiments at low energies (< 10 eV), but has enabled other techniques to be developed [74] to address that width.

Coupling a high efficiency rare-gas moderator with a Surko buffer-gas trap, allows for the creation of a pulsed positron source with a low energy spread [75]. The Surko trap (buffer-gas or Penning-Malmberg trap as discussed in chapter 2) has enabled accurate low-energy (< 10 eV) scattering experiments by providing a beam of positrons with a small angular acceptance and low energy width, in conjunction with new experimental techniques. The implementation of the current Surko-style trap system [76] is now discussed in all of its operational detail, for use in scattering experiments, and a schematic of the complete system is shown in figure 3.1.

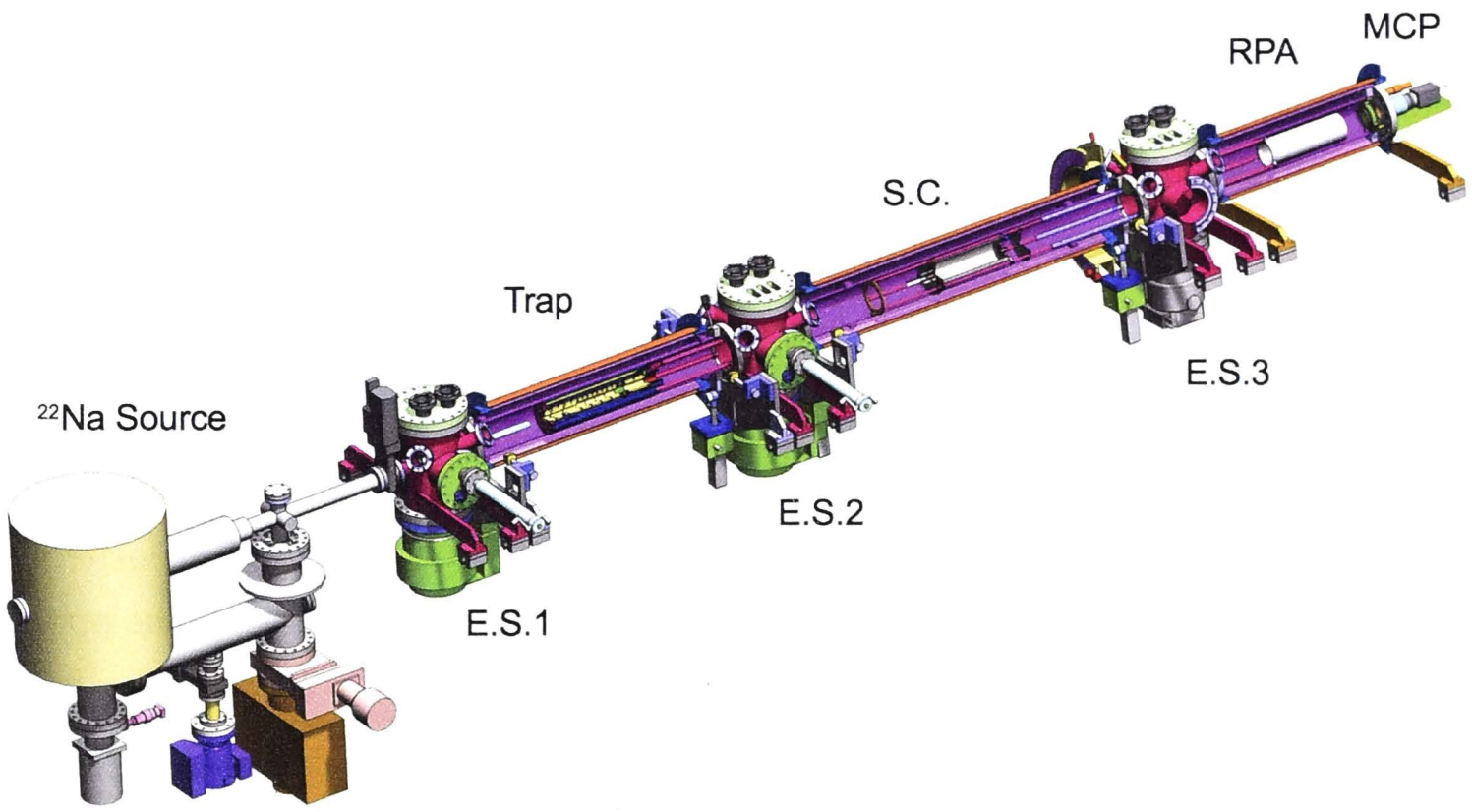

Figure 3.1: Solidworks render of the Positron beamline [76], showing a schematic of the relevant sections. The system consists of four sections (from left to right): ^{22}Na source stage (RGM-1), Surko Trap, Scattering Cell (S.C.), Retarding Potential Analyser (RPA) and Micro Channel Plates (MCP). Each section is separated by a pumping station (E.S.), with the first station immediately to the right of the source stage; E.S. 1, E.S. 2 and E.S. 3. The final detector assembly is shown to be an MCP stack coupled to a CCD camera, but this was not used for these experiments. The electron current from the micro-channel plates was in fact measured for the measurements described in this thesis. See text for discussion of each section.

3.2 Positron Source

The source stage (RGM-1) is a commercially available positron source and was purchased from First-Point Scientific [77]. This system consisted of a vessel to house the radioactive source, a cryostat to provide for the freezing of a moderator gas on to the surface of the source capsule, the required pumping to provide vacuum (UHV) and shielding from both the 1.2 and 0.511 MeV γ-rays from the source. The radioactive ^{22}Na was purchased from iThemba labs [78] and came as a sealed ^{22}Na capsule with a maximum activity of ~ 1.9 GBq (~ 50 mCi), see figure 3.2. Ultra high purity Neon (99.999%) was used to grow a solid Neon layer onto the Cu moderator cone shown in figure 3.2. The Ne moderator was

grown at a temperature between 7-9K. A small number of the positrons are moderated ($\sim$ 1 %) by the Neon, these low energy positrons follow a guiding magnetic field around the radiation shielding. This shielding is configured such that there is no line-of-sight to the source, but rather only low energy positrons are transmitted to the next stage. A positron beam with an energy spread of $\sim$ 2 eV was obtained from the RGM system shown in figure 3.2 and discussed below. The continuous positron current from the source and moderator combination was guided into the Surko trap via a guiding magnetic field. To measure the relative strength of the positron beam, these positrons were directed to the gate valve separating the positron source chamber from the Surko trap, and the resultant annihilation γ-rays were detected using a NaI(Tl) scintillator coupled to a photomultiplier tube.

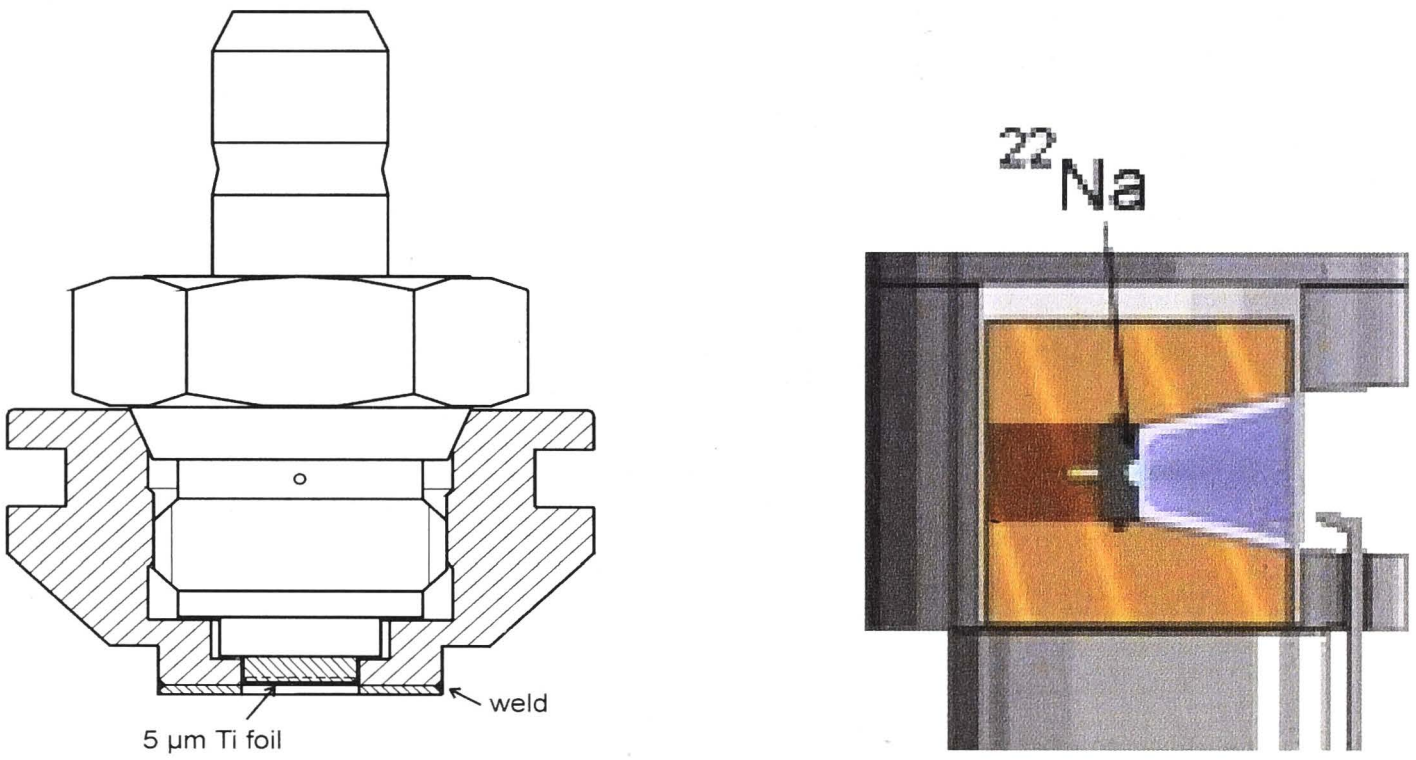

(a) Source Capsule (b) Cone

Figure 3.2: (a) Schematic of the source capsule containing the sodium-22 (^{22}Na) which is installed into the RGM-1 apparatus, (from `http://positron.physik.uni-halle.de/source.html`). (b) Schematic of the Cu source cone mounted onto the end of the Cryostat [69]. The moderator gas flows from the tube on the bottom right side on to the surface of the source. When the surface is sufficiently cold, the moderator begins to crystalize on the surface.

3.2.1 ^{22}Na Source

The sodium-22 (^{22}Na) is produced in a cyclotron and provided encapsulated in a sealed source from iThemba Labs [78]. The source capsule was designed by the Positron Laboratory of the Department of Physics of the Martin-Luther-University Halle, as shown in figure 3.2 (a). This source capsule design was used by First-Point Scientific and incorporated into their RGM-1, which allows for simple extraction of the source while maintaining proper shielding. As noted previously the source activity was $\sim$ 50 mCi or $\sim$ 1.9 MBq when obtained from iThemba Labs, and the activity decays with a half-life of 2.6 years. The source was removed for regular maintenance of the cryostat, thus over more than 3 years of operation the source capsule was removed/installed around 6 times. The source

capsule was housed in a Cu cone fixed to the cryostat (DE-204NB), or 'coldhead', as shown in figure 3.2 (b).

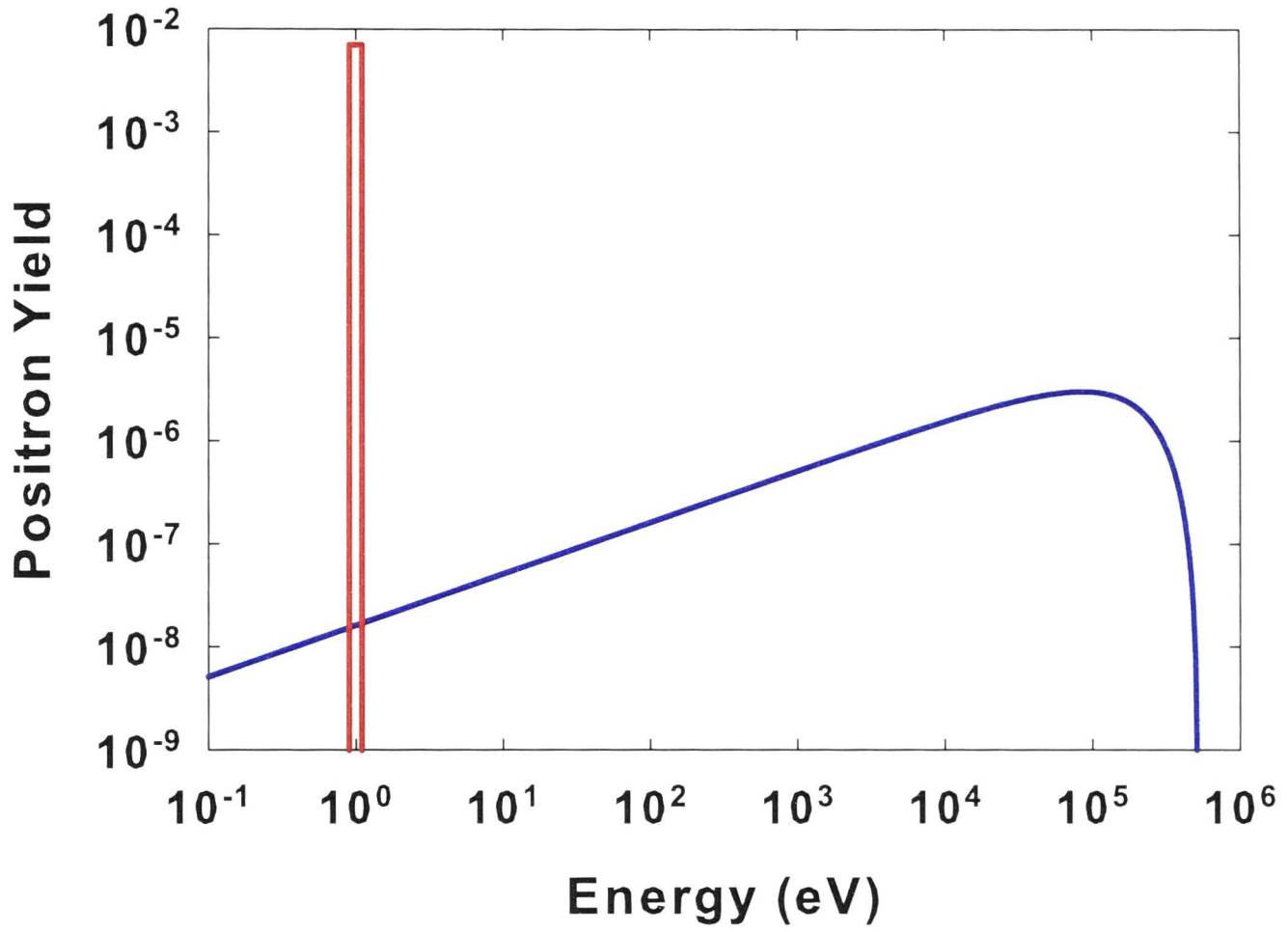

Figure 3.3: The probability energy spectrum (blue line) of the production of positrons from sodium-22 (^{22}Na) and the spectrum of moderated positron (red line), adapted from [21].

The ^{22}Na source provided positrons with a wide energy distribution like that shown in figure 3.3. Moderation, or cooling, of the positrons from the radioactive source was required to produce a tunable, narrow energy width beam. This moderation was provided by the frozen neon, which was sprayed onto the cone from a small nozzle pointed toward the source. The cone or source/moderator geometry plays a role in the overall moderation efficiency by providing a structure for gas to freeze upon forming the moderator. The design of various cones and their efficiencies was discussed by Mills [4] and the optimum suggested design is used in the RGM-1 system, resulting in a moderation efficiency of about 1 %. The RGM-1 positron source has several layers of radiation shielding materials; tungsten blocks, lead shot and elkonite blocks were used to provide protection from the 1.2 MeV γ-rays that are produced in the radioactive decay of ^{22}Na to ^{22}Ne. The moderated positron beam was guided through a shielding block using a set of paired defection coils (or saddle coils). This removed radiation exposure along the line of sight to the source. Another set of solenoidal coils transported the positron beam into the Surko trap.

Installation of the sodium-22 source required the RGM-1 to be brought up to atmospheric pressure. This was done using the vent valve on the turbo-molecular pump on the source stage allowing the source stage to be vented with dry nitrogen and thereby limiting the amount of atmospheric water and other impurities from streaming into the system. After installation of the source capsule containing the ^{22}Na source, the source

stage was pumped back down and baked to remove any water that absorbed on the surface of the chamber. The construction of the RGM-1 system incorporated an indium seal which begins to deform at 310 K. Therefore, during baking of the system, the cold head temperature was kept below 300K. It was found that growing a series of moderators gave improvements in their performance with each grow, indicating that the system was being further cleaned by the process of growing and evaporating moderators.

3.2.2 Rare Gas Moderators

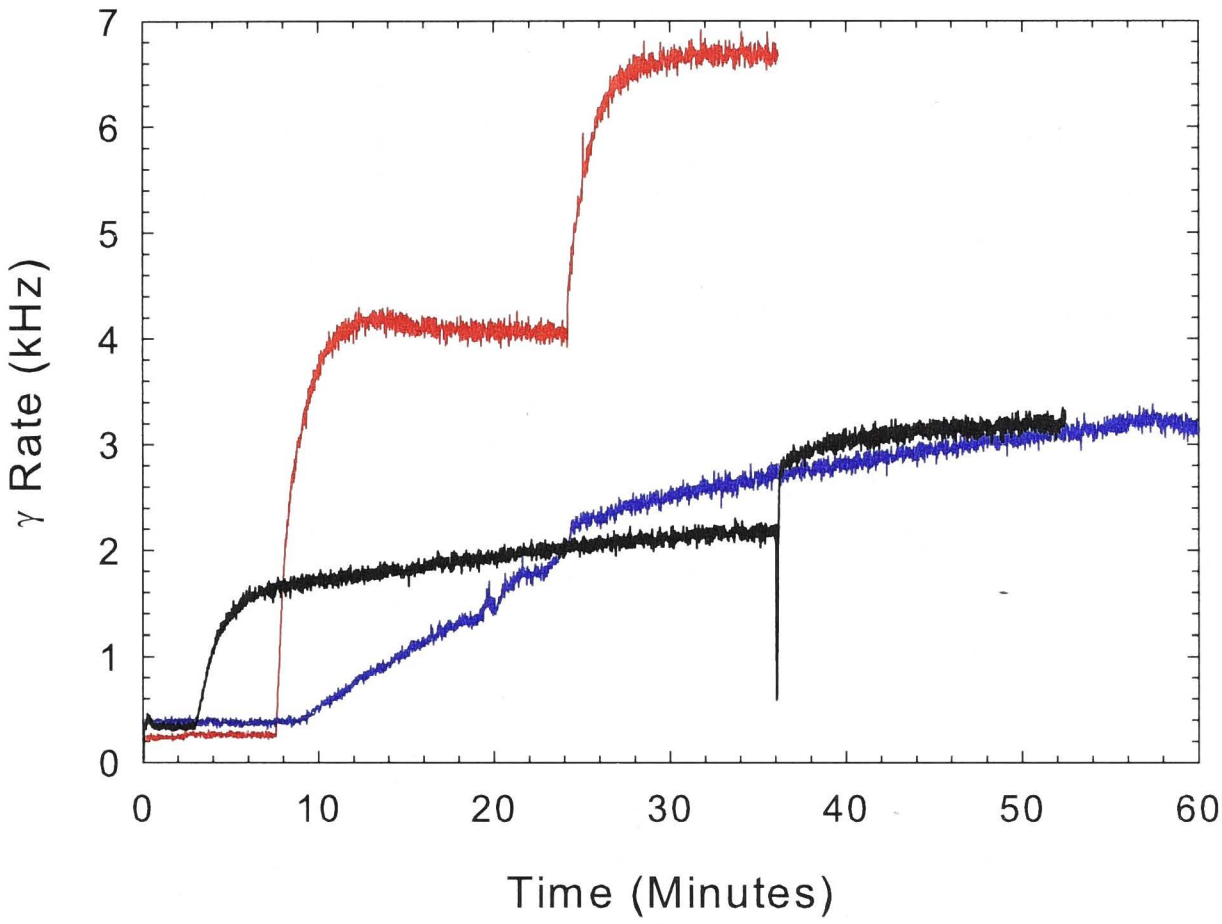

Figure 3.4: Example growth curves for Neon (red), Argon (black), and Krypton (blue) moderators for approximately the same source activity. The growing conditions were different, see text.

Table 3.1: Rare Gas Moderation Efficiencies ϵ_m for Neon [4] and Argon up to Xenon [79].

Atom	$\epsilon_m(\text{x}10^{-4})$	Mills ϵ (%)	Mills (ΔE)	Freezing Pt. (K)	Growing Temp. (K)
Ne	70	0.70(2)	0.58(5)	24.56	7-9
Ar	2.5	0.13(2)	1.7(2)	83.80	$\sim$ 20
Kr	1.6	0.14(2)	1.8(2)	115.79	$\sim$ 30
Xe	1.1	0.13(2)	3.2(4)	161.4	$\sim$ 50

For the majority of the experiments contained in this work, Neon was used as the moderator. However, at different times, Argon and Krypton moderators were also used when the cryostat could not maintain a sufficiently low and stable temperature to grow a Ne moderator reliably (7-9 K). A comparison of the freezing points, growing temperatures, moderation efficiencies and moderated beam energy width for the noble gases is provided in table 3.1, with a comparison of the growth profiles for Ne, Ar and Kr in figure 3.4. The growth profiles were studied using a CsI(Tl) scintillation crystal coupled to a photo-multiplier tube (Scionix Holland, Model: 25P25/10-E3-CS-110), at the vacuum gate valve separating the RGM-1 from the rest of the beamline. These growth profiles occurred with approximately the same source strength and the same γ-detector solid angle, but slightly different gas densities for each moderator gas during the growth of each moderator. No direct measurement of the moderation efficiency was determined, but the figure 3.4 can be used to estimate the moderation efficiency of neon in this system. Assuming that argon and krypton have a moderation efficiency of $2\text{x}10^{-4}$, the neon moderation efficiency of the current system is $\sim 5\text{x}10^{-4}$ which is significantly lower than reported by Mills [4]. A more detail exploration of moderation efficiency was not in the scope of this work.

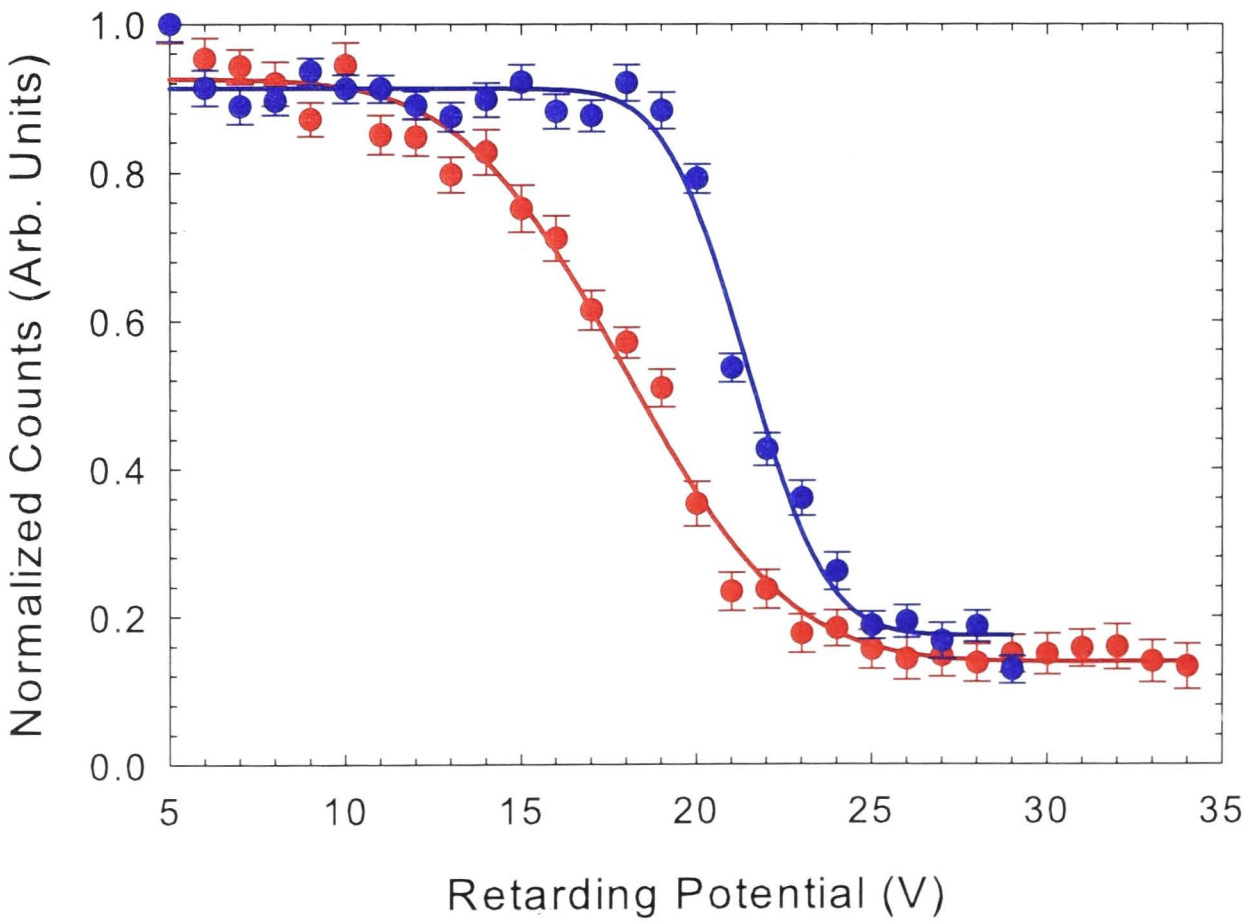

Figure 3.5: Measurements of the parallel energy width of an Argon moderated beam. The parallel energy spectrum at 530 G (or 0.053 T) is in red: solid circles, measured data; solid line, fit of energy spread (8.7 eV). The parallel energy spectrum measured at 100 G or (0.01T) is in blue: solid circles, measured data; solid line, fit of energy spread (4.3 eV).

A standard growth profile for the Ne (or Ar/Kr) moderator consisted of warming the cryostat sufficiently high in temperature to remove any Ne (or Ar/Kr) left from previous moderators. This was followed by a short pump out period before the cryostat was then returned to a temperature low enough to freeze neon (or Ar/Kr) on the Cu source cone.

Neon gas was then admitted to the system via the nozzle until the chamber pressure reached approximately 8x10^{-4} Torr. Previous work has shown that when the annihilation signal has plateaued the moderator had finished growing [4]. The neon feed can then be stopped and the excess gas removed from the system. The difference between the first and second plateaus seen in figure 3.4 is due to the attenuation caused by the moderator gas at a scattering energy of eV$_{mod}$, see Jones *et al.* [7] and Makochekanwa *et al.* [8].

The characteristic Ne moderator on this system has an energy spread of approximately 1.5 eV as measured in an axial magnetic field of $\sim$ 100 Gauss (0.01 T), whereas Mills measured the full width half-maximum to be 0.58 eV [4]. The magnetic field at the retarding potential analyser (RPA) could be adjusted to accurately measure the parallel energy width of the moderator using the same field magnitude as the source. A different field will have the effect of broadening the apparent energy spread, for reasons discussed later in Chapter 4, §4.1. The parallel energy distribution of an Argon moderator is shown, by way of example, in figure 3.5 and depicts the different observed distribution for different field strengths. This relationship will be discussed in the next chapter, but is worth noting here for the operation and tuning of the Surko trap, see next section.

The moderated positron flux was observed to decay with time. This happened both during operation of the trap and while the source and moderator were isolated from the buffer-gas trap. The gases used in the trap can back stream from the trap stage into the source stage (RGM-1) and freeze on the surface of the moderator during normal operation. When isolated from the trap, the background gas in the source vacuum chamber would freeze onto the moderator. Raising the temperature of the source cone, by running the cyrostat heater or by turning off the cryostat, allows the contaminant(s), and a small portion of the moderator, to evaporate. An example of removing the contamination and regrowing an Argon moderator is shown in figure 3.6. In this case, the moderator strength had decayed by a third in four days of operation, and this decay was recovered by cycling the cryostat temperature. This technique, however, was unsuccessful for Neon, because of insufficient control of the cryostat temperature between 7 and 9 K.

3.3 Positron Trap

The present positron trap, used to produce a high energy resolution pulsed positron beam, is adapted from the work of Murphy and Surko [3] for conducting low-energy positron scattering experiments [76]. The trap confines and cools positrons from the source moderator stage, resulting in a parallel energy width or resolution of $\sim$ 60 meV or better. Tuning of the trap electrodes and gas densities resulted in a range of beam energy widths, and the trap had a variable repetition rate, but was usually operated near 100 Hz.

The trap consisted of nine electrodes, shown in figure 3.7. Each electrode was constructed from oxygen-free high conductivity copper (OFHC), plated with gold and separated by polyether ether ketone (PEEK) spacers or ruby balls for electrical isolation. These cylindrical electrodes provided the longitudinal confinement of the trapped positrons and

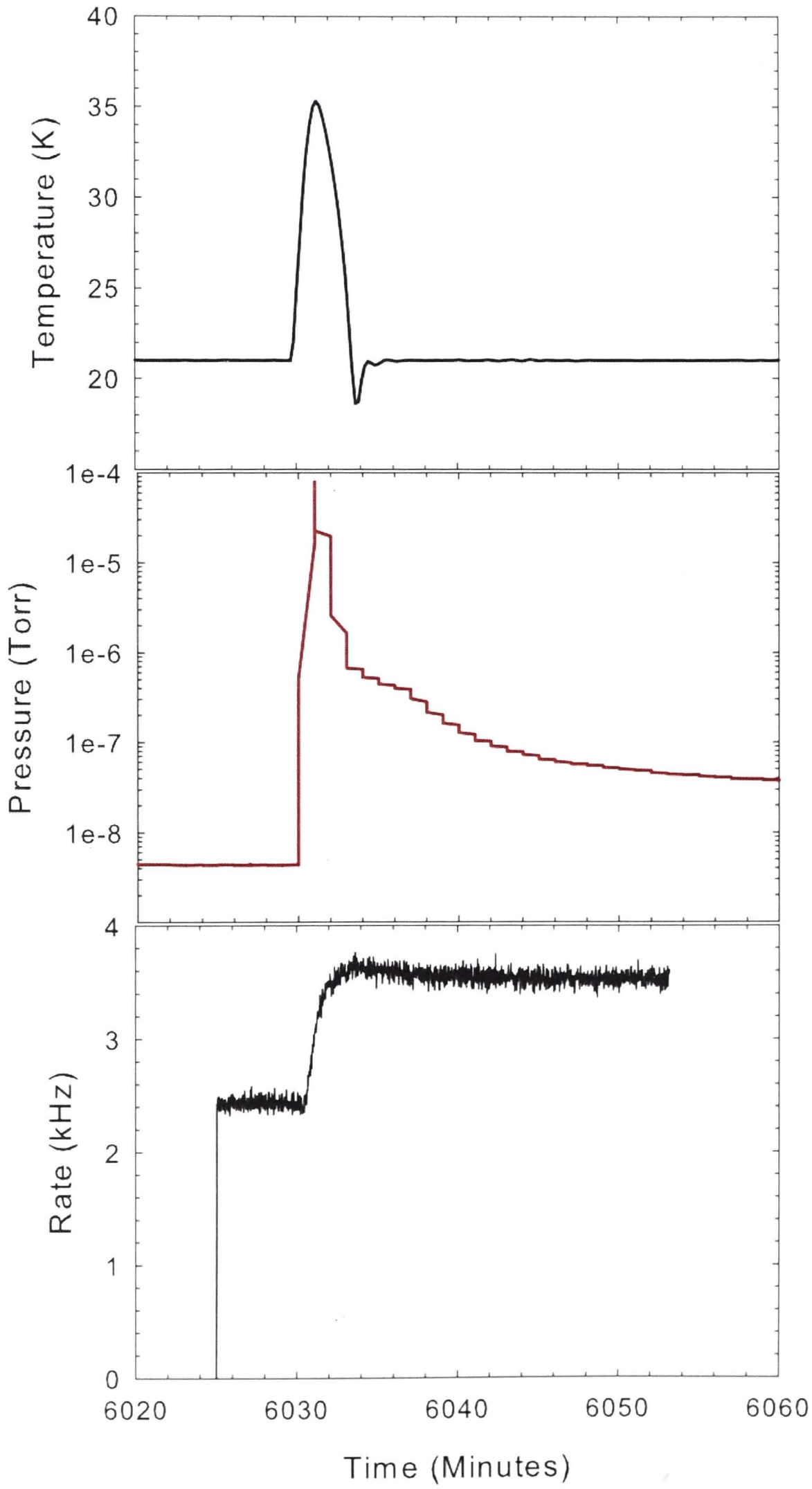

Figure 3.6: An example of thermal cycling of an Argon moderator. The top panel is the cryostat temperature, the middle panel is the source stage pressure measured using an ion gauge (no correction for sensitivity) and the bottom panel is the γ-ray counts of the moderated beam annihilating on the gate valve of the source stage. A very similar result is observed when Krypton is used as the moderator.

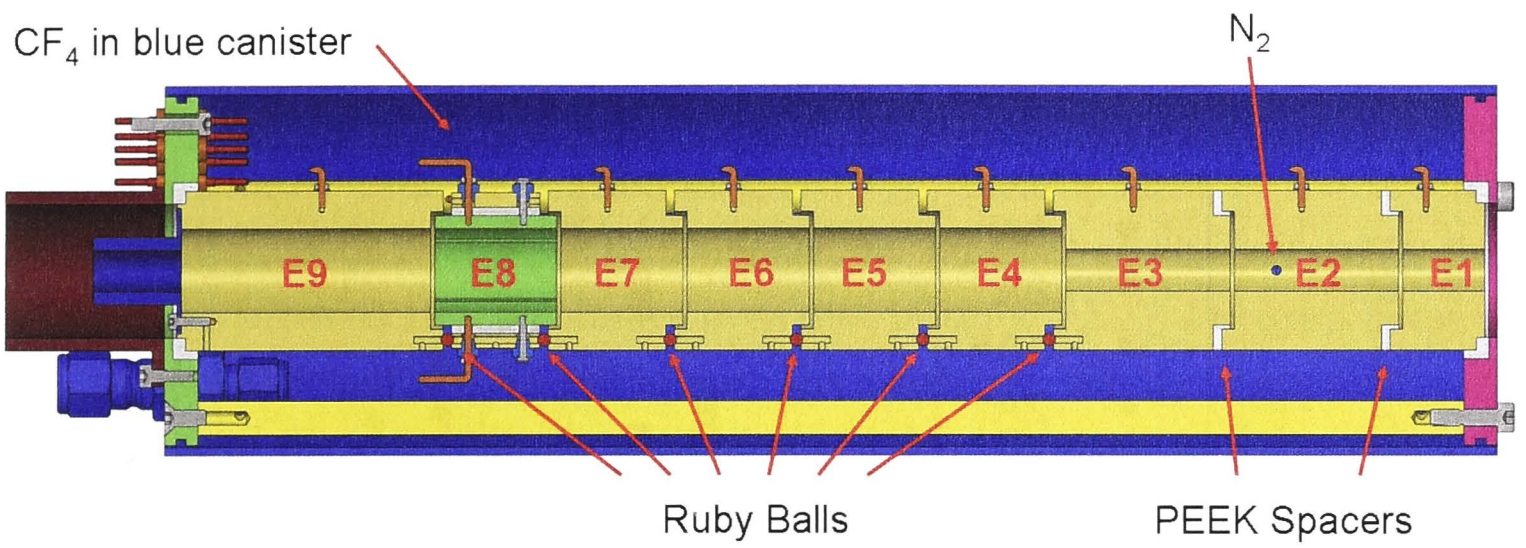

Figure 3.7: Schematic drawing of the trap electrodes. The green electrode is the segmented electrode and is divided into four pieces or quadrants. For a majority of these measurements the green or segmented electrode was in position E6 (E6 and E8 could be interchanged), see chapter 9 for an extended discussion.

set the scattering energy for positrons traversing the trap. Each electrode is connected to a high-voltage, fast amplifier (ElbaTech T-506) via coaxial electrical feedthroughs. Control of the electrode potentials is provided by a Labview program which assigns the potentials as a function of time, for all electrodes in the trap, via two high-speed 16-bit analog output cards (National Instruments PXI-6733). These outputs are connected to the input of the high-voltage amplifiers which provide either a 10x or 20x amplification with a maximum voltage range of $\pm$ 200 V.

A solenoidal magnetic field of 0.53 T (530 Gauss) was used to radially confine the positrons. The field was provided by a water-cooled solenoid which could be mechanically adjusted vertically and horizontally, to tune the alignment between the electric and magnetic fields of the trap. An azimuthally segmented electrode was used to apply a rotating electric field at radio frequencies (RF), this is also known as the rotating wall electrode, for compression of positrons confined in the trap. The operational details of the rotating wall electrode will be discussed later in chapter 9.

The guiding solenoid or beam tube on the RGM-1 is wound on the vacuum vessel itself, there is no mechanical adjustment to align the moderated positron beam with the entrance aperture for the trap. A differential pumping tube forms the beam defining aperture of the trap, but there is no physical, vertical or horizontal, adjustment since the two systems are connected via a conflat flange with no associated bellows. Addition of a trim coil, producing a magnetic field orthogonal to the positron beam direction, was made to provide vertical adjustment of the moderated positron beam at the entrance of the Surko trap (well removed from the previously mentioned saddle coils). A series of tuning curves is shown in figure 3.8 for various settings of the fixed beam tube magnet. It is clear that adjustment of the trajectory of the incident beam is required to optimise the operation of the trap. A similar exercise was attempted for a horizontal trim coil with little success, thus only a vertical displacement coil was implemented.

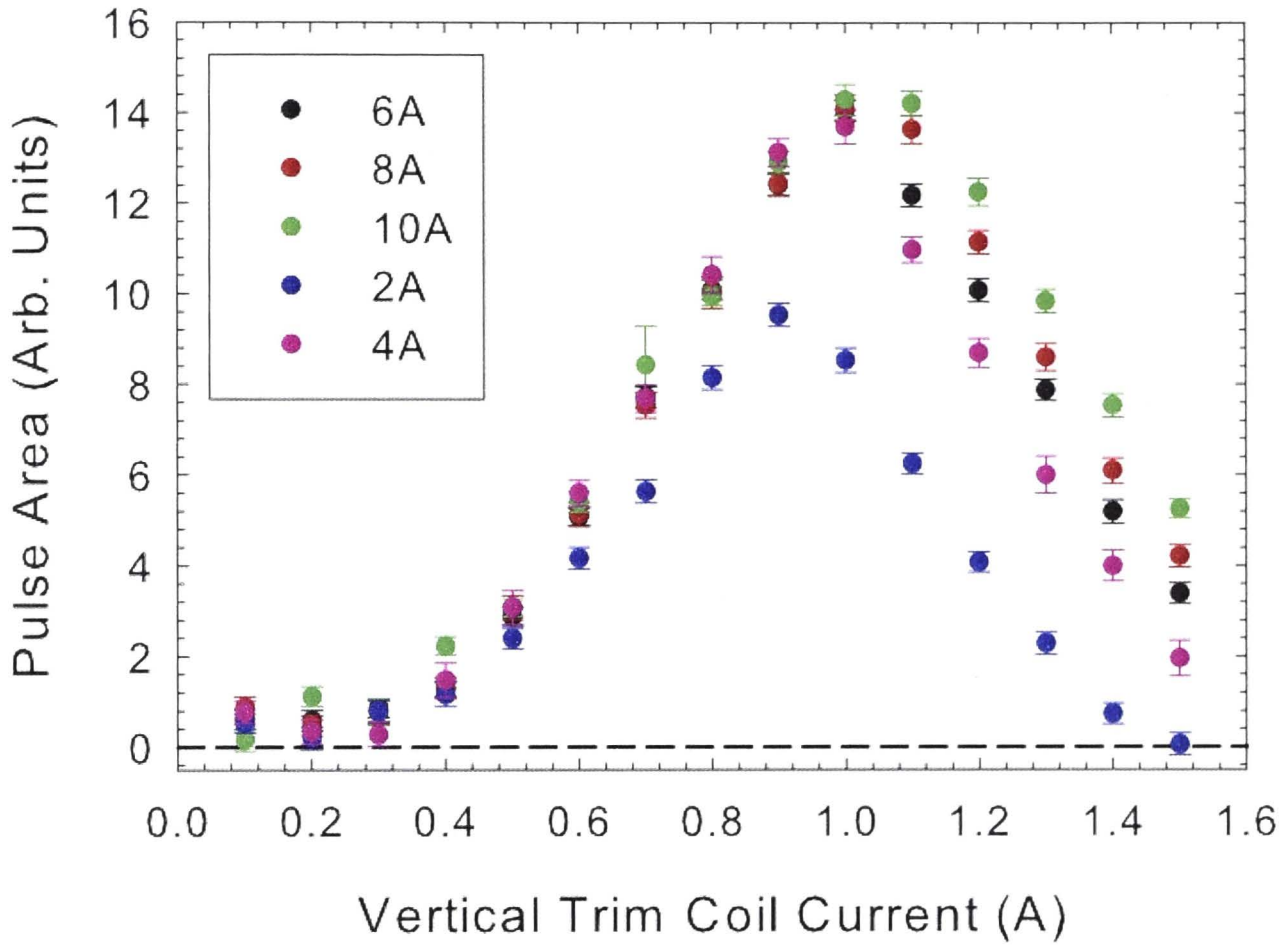

Figure 3.8: Tuning curves for various trap coil currents. The field strength is proportional to the current.

3.3.1 Trap Operation

The time structure of the positron beamline is dependent on three stages - the loading, cooling and dumping of the positrons. These 3 modes each have their own electrostatic potentials, dictating the dominant process occurring in the trap, and are shown graphically in figure 3.9.

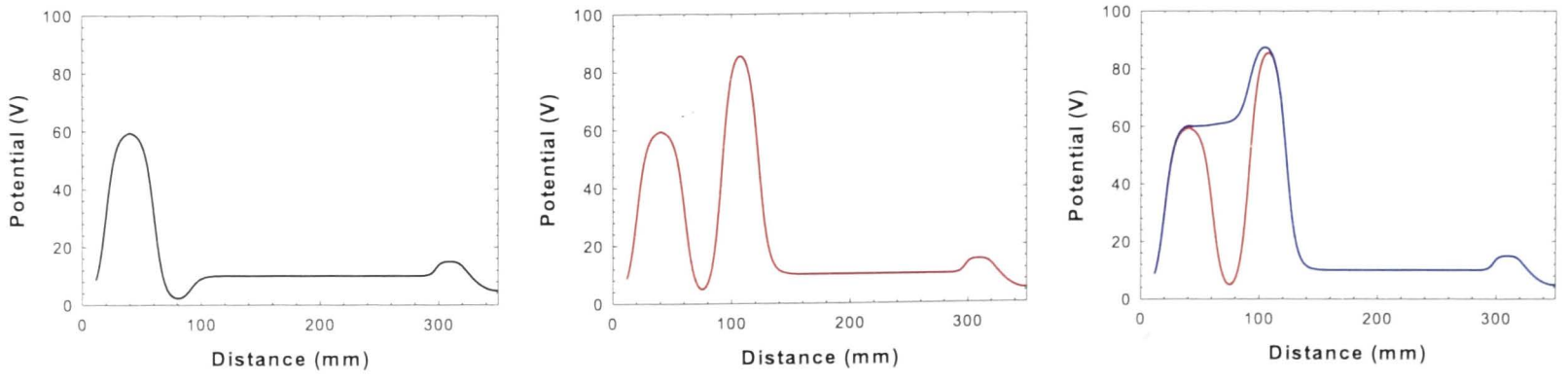

(a) Loading (b) Cooling (c) Dumping

Figure 3.9: A schematic diagram of the electrostatic potentials versus longitudinal dimention used for loading (a), cooling (b) and dumping (c) of positrons, which enter from the right side of the plot and exit on the left side.

Loading the Trap

Positrons must lose energy in inelastic collisions to become trapped in the potential well and this is facilitated with molecular nitrogen (N_2). Measurement of the two relevant electronic excitations of N_2 by positron impact, by Sullivan *et al.*, has shown that the $a\,^1\Pi_g$ excitation cross section dominates over that of the $a'\,^1\Sigma_u^-$. The trap potentials in the first part of the well are set initially so the scattering energy is approximately 8.8 eV. This is above the threshold for excitation of the $a\,^1\Pi_g$ state at 8.59 eV [31] and at the threshold for positronium formation (8.78 eV). The Ps formation (loss) and electronic excitation scattering (trapping) channels thus compete for positron flux. The unusual case of electronic excitation thresholds below the Ps formation threshold, as in N_2, is ideal for trapping. The scattering energy in the first stage of the trap is adjusted empirically to find the maximum in the trapped flux, before positronium formation dominates causing a decrease in trapped positron flux. The loading time and N_2 density were optimised empirically in previous work [69].

Cooling

During cooling, positrons trapped in the lower potential well are isolated from the rest of the trap by raising an electrode to form an electrostatic barrier. Positrons in the final section of the trap (electrode E8 in figure 3.7) lose further energy via vibrational and rotational excitation of CF_4 and N_2. CF_4 has a positron cooling time two orders-of-magnitude faster than N_2 [80], allowing the trapped positrons to cool on the order of milliseconds for the present trap configuration. Vibrational excitation of the dominant fundamental mode, ν_3 (159 meV), of CF_4 has been measured by Marler *et al.* [37] and it has a peak scattering cross section an order-of-magnitude higher than the peak excitation of the $a\,^1\Pi_g$ state of N_2. Positrons cool further by rotational excitations, allowing thermalisation of the trapped positrons with the room temperature trap gases. The cooling time could be adjusted, but typically was 1 to 5 milliseconds, given the CF_4 density that was optimised empirically as in previous work [69].

Dumping of the Positron Beam

The cold positron beam was then expelled from the trap by raising the bottom of the confining well to a potential larger than the potential of the final electrode (E9), but lower than the blocking electrode (E7), as shown schematically in figure 3.9. Accumulated positrons are then ejected from the potential well, or from the interior of electrode 8, and are prevented from traveling back toward the source due to the blocking electrode. The ejected positrons have an energy of $E_T = e(V_{E9} - V_{Chamber})$, where $V_{Chamber}$ is at ground or earth potential. The time dependent potential profile of electrode 8 (E8) in the dumping phase was logarithmic, which was found to give the most consistent results compared to a linear or stepped profile. This dump profile had the advantage of rapidly raising the thermalised positron beam near the transport energy and smoothly ramping

above the wall electrode, minimising any heating of the trapped positron cloud before being dumped. A typical positron dump duration was 3 milliseconds giving a total trap time of $\sim$ 15 milliseconds.

3.4 Scattering Cell

The scattering cell (SC) is fabricated from an OHFC tube and was plated with gold (Au). Each cell consisted of a tube which was clamped in place by two bulk heads, also constructed of gold plated OHFC. These bulk heads were electrically isolated from their mechanical supports by custom ceramic spacers. Three different scattering cell lengths can be used; 50, 100 and 200 mm. One gas feed line was connected to the scattering cell to provide the target gas and another line was connected to a capacitance manometer. The capacitance manometer, or Baratron (MKS Model #: 690A01TRA), was used to monitor the target pressure during the experiment and was maintained at a temperature of 45 degrees Celsius to minimise effects due to temperature fluctuations. This measurement was used to determine the absolute density in the scattering cell required for determining absolute scattering cross sections.

The energy of the positron beam traversing the system is determined by measuring the parallel energy distribution, as discussed below in §3.5. The center of the positron beam energy distribution measured using the SC, V_{sc}^{c}, is used to set the collision energy (E_c) within the SC,

$$E_c = e(V_{sc}^{c} - V_{sc}). \tag{3.1}$$

The target gas flowed out of the scattering cell via the entrance and exit apertures which were 4.5 mm in diameter, forming a beam of target atoms or molecules. The radial and axial profile of the atomic and molecular beams generated from apertures and capillaries has been measured and modeled [81, 82]. A gold plated cylindrical copper mesh was fixed to both the entrance and exit apertures, which extended beyond the radial and axial extent of the target gas outflow. This maintained the collision energy along the positron scattering path and ensured that the quantity nl was the product of the measured density and the physical length of the scattering cell [83]. A successful demonstration of this was the benchmarking of the positron-helium grand total scattering cross section [84].

3.5 Retarding Potential Analyser

The parallel component of the positron energy, see §4.1 of Chapter 4, was analysed using a cylindrically symmetric retarding potential anaylser (RPA). It consisted of a gold-plated OHFC tube mounted with the axis of symmetry parallel to the solenoidal magnetic field. The RPA was set to a potential, V_{RPA}, and only positrons with parallel energy higher than eV_{RPA} pass through and are detected. The RPA is used to measure the number of positrons as a function of V_{RPA} and the derivative of this measurement yields the parallel energy spectrum. The RPA is routinely used to determine the parallel energy width of the

positron beam from the trap. A measurement of the parallel energy distribution of the positron beam is shown in figure 3.10. Positrons accumulated and cooled in the trap have undergone many inelastic collisions in the process of thermalisation. The parallel energy width of the positron pulse is approximated using a Gaussian or normal distribution which is a complementary error function,

$$erfc(x) = 1 - \frac{2}{\sqrt{\pi}} \int_0^x e^{-t^2} dt. \tag{3.2}$$

Generally, the full-width at half maximum (FWHM) is used to report the parallel energy width which is determined from the standard deviation (σ) of the Gaussian,

$$FWHM = 2\sqrt{2ln2}\sigma. \tag{3.3}$$

Positrons that undergo scattering may lose a significant amount of parallel energy. Measuring the number of positrons as a function of V_{RPA} is therefore also used to determine which scattering processes the positron has undergone, as discussed in Chapter 4.

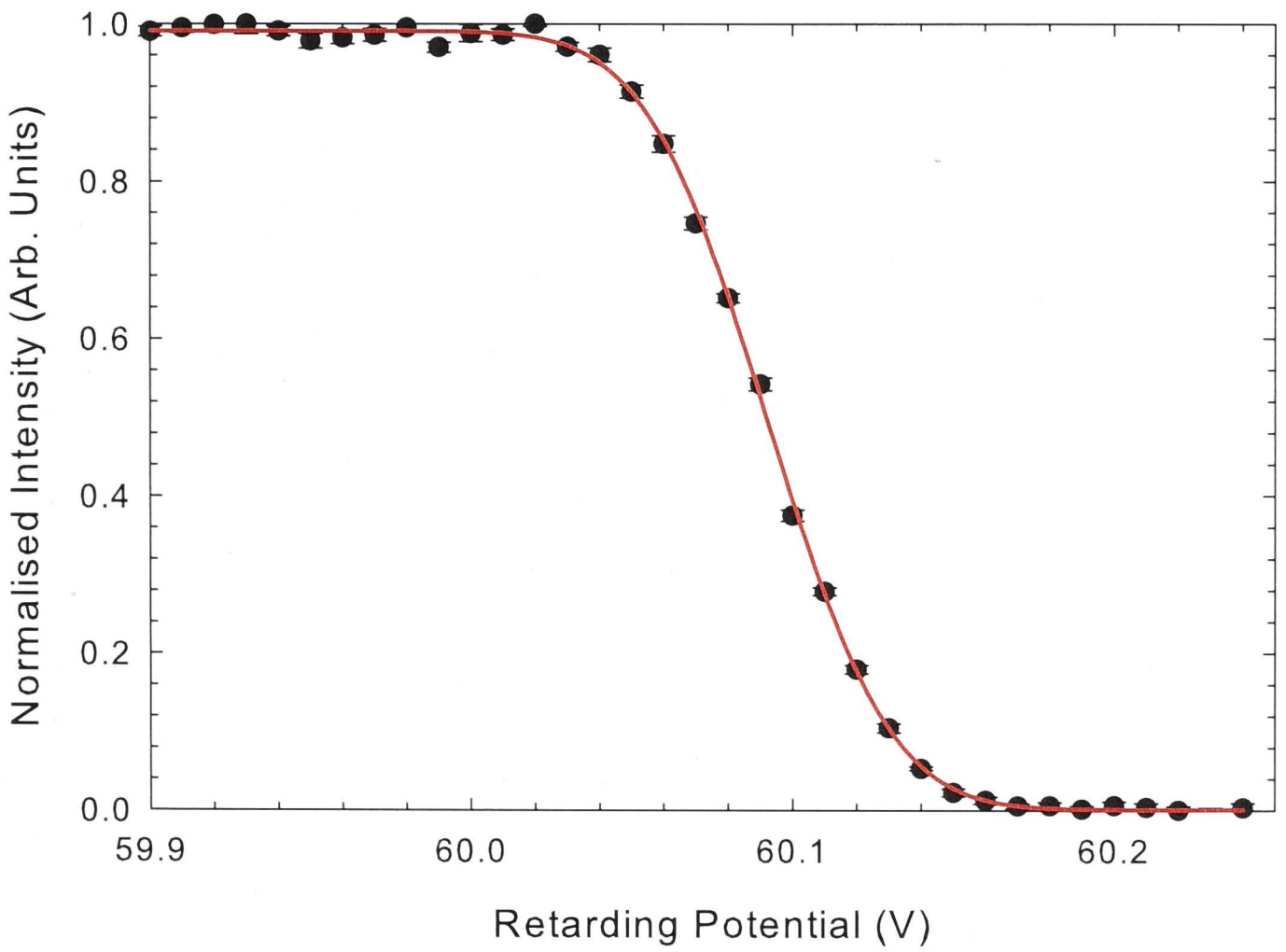

Figure 3.10: A measurement of the parallel energy width of the positron beam. The data (black points) is fitted using equation 3.2 (red line) and in this case the beam width is $\sim$ 70 meV (FWHM).

3.6 Positron Detection

The positron detection system consists of a double stack micro-channel plate (MCP) arranged in a chevron configuration and installed on a 6-inch conflat (CF) flange. The front of the MCP stack was biased negatively and the back of the stack was biased positively. Typically the bias on the front MCP was $\sim$ - 300 V and at the back of the MCP stack it was set to $\sim$ + 1700V to provide the maximum gain. A grounded mesh was added above the MCP stack, to shield the electric field from the RPA region, in an effort to reduce $\vec{E} \times \vec{B}$ effects and limit any alteration of the analysing field of the RPA by the MCP potential. The output of the MCP stack was capacitively coupled to a current-to-voltage amplifier (Femto HCA-1M-1M-C). This transimpedance amplifier converted the current pulse into a voltage pulse which was read into an oscilloscope card on the PXI-Chassis. The PXI-5114 was a 250 kS/sec digitiser card which allowed the voltage pulse from the amplifier to be recorded. A variable time window was used to ensure that the entire pulse was captured and was usually a millisecond in width. These pulses were integrated and background subtracted within the Labview Code to provide a measurement of the charge incident on the MCP.

3.7 Final Remarks

This implementation of a Surko style buffer-gas trap provides a pulsed positron beam with an energy width as low as 40 meV. It is coupled to a scattering apparatus which allows for the determination of the parallel energy of positrons which have passed through the scattering or gas cell at a specific energy. The parallel energy loss is subsequently used to determine scattering cross sections, as will also be discussed in the next Chapter.

Chapter 4

Analysis Considerations

The techniques used to determine scattering cross sections in a magnetically confined and guided positron scattering apparatus, from the measurement of the parallel energy loss of scattered positrons, are discussed in this chapter. Various constraints are reviewed, with specific examples given illustrating the limitations of the present technique.

4.1 Positrons in a Magnetic Field

The motion of a charged particle in an external field is governed by the Lorentz force ($\mathbf{f}$) law,

$$\mathbf{f} = q\left(\mathbf{E} + \mathbf{v} \times \mathbf{B}\right), \tag{4.1}$$

where q is the charge of the particle, $\mathbf{v}$ is the velocity of the particle, $\mathbf{E}$ is the electric field, and $\mathbf{B}$ is the magnetic field. In these experiments, the scattering region is contained in a solenoidal magnetic field which radially confines the positrons. Considering only the magnetic field, equation 4.1 becomes,

$$\mathbf{f_B} = q\mathbf{v} \times \mathbf{B}, \tag{4.2}$$

where the force ($\mathbf{f_B}$) due to the magnetic field is orthogonal to both the velocity and the field. This force leads to cyclotron motion of the positron in which the circular motion of the positron in a magnetic field is related to its velocity (perpendicular to the field),

$$r_c = \frac{mv_\perp}{q|\mathbf{B}|} = \frac{\sqrt{2mE_\perp}}{q|\mathbf{B}|}, \tag{4.3}$$

where r_c is the cyclotron radius and $E_\perp$ is the kinetic energy of the particle perpendicular to the magnetic field. The axis of the magnetic field determines a reference for the motion of the positron and this vector relationship leads to deconstruction of the kinetic energy into two orthogonal components, where the velocity component perpendicular to the field line results in the radial motion or gyration of the positron and the component parallel to the field is the axial motion. Two components of the total energy (E_T) can thus be defined; one parallel to the magnetic field and one perpendicular to the magnetic field

such that,

$$E_T = E_{||} + E_{\perp}. \tag{4.4}$$

$E_{||}$ is related to the parallel and total velocities so that,

$$E_{||} = \frac{1}{2}mv_{||}^2 = \frac{1}{2}v^2 cos^2\theta. \tag{4.5}$$

where θ is the angle between the direction of the total velocity and the axis of the confining magnetic field. If the magnetic field varies adiabatically (spatially or temporally) such that the total kinetic energy of the positron is conserved, the ratio of the kinetic energy orthogonal to the magnetic field is invariant or constant,

$$\gamma = \frac{|\mathbf{B}|}{E_{\perp}}. \tag{4.6}$$

As a result, a positron with a $E_{\perp}$ at one field magnitude $|\mathbf{B}|$ will have a different $E'_{\perp}$ at different field magnitude $|\mathbf{B}'|$ if the field changes adiabatically. A simple ratio, M, between two field magnitudes can be defined,

$$M = \frac{|\mathbf{B}'|}{|\mathbf{B}|} = \frac{E'_{\perp}}{E_{\perp}}. \tag{4.7}$$

As discussed previously in Chapter 3, the retarding potential analyser (RPA) is cylindrically symmetric with the axis parallel to the axis of symmetry of the solenoid. Therefore, only the parallel energy can be analysed using the RPA. For the beam energies (between 60 and 200 eV) and resolutions ($\sim$ 60 meV) considered in this thesis, the perpendicular energy is small, $E_{||} \gg E_{\perp}$, such that $E_{||} \sim E_T$.

For scattering experiments, the collision energy, E_c, is determined by the potential of the scattering cell (SC) as discussed in Chapter 3. It is the maximum amount of energy which can be lost in a collision within the SC,

$$E_{||}^{min} = E_{||} - E_c. \tag{4.8}$$

Positrons exiting the SC have a distribution of the parallel energy loss between $E_{||}^{min}$ and 0 eV, which is determined by the scattering process. Varying the RPA potential allows the measurement of the number of positrons transmitted as a function of the parallel energy of the positron, $I_c(E_{||})$. The method for determining the angular or elastic differential scattering cross section will be discussed below (§4.4).

By measuring the number of positrons which have undergone a particular loss of parallel energy, the grand total and partial scattering cross sections can be determined. The invariance of the ratio between the field magnitude and perpendicular energy allows for the distribution of the energy loss spectrum to be altered by changing the field, which is discussed below, to separate elastic from inelastic scattering (§4.5).

4.2 Grand Total Scattering Cross Section

The grand total scattering cross section (σ_{GTCS}), discussed in Chapter 2 (see also equation 4.9), was determined using the Beer-Lambert Law,

$$\sigma_{GTCS} = -\frac{1}{nl} \ln\left(\frac{I_m}{I_{OR}}\right), \tag{4.9}$$

where I_{OR} is the intensity of the unscattered beam, I_m is the intensity of the scattered beam, n is the density of the target and l is the length of the scattering cell. A schematic

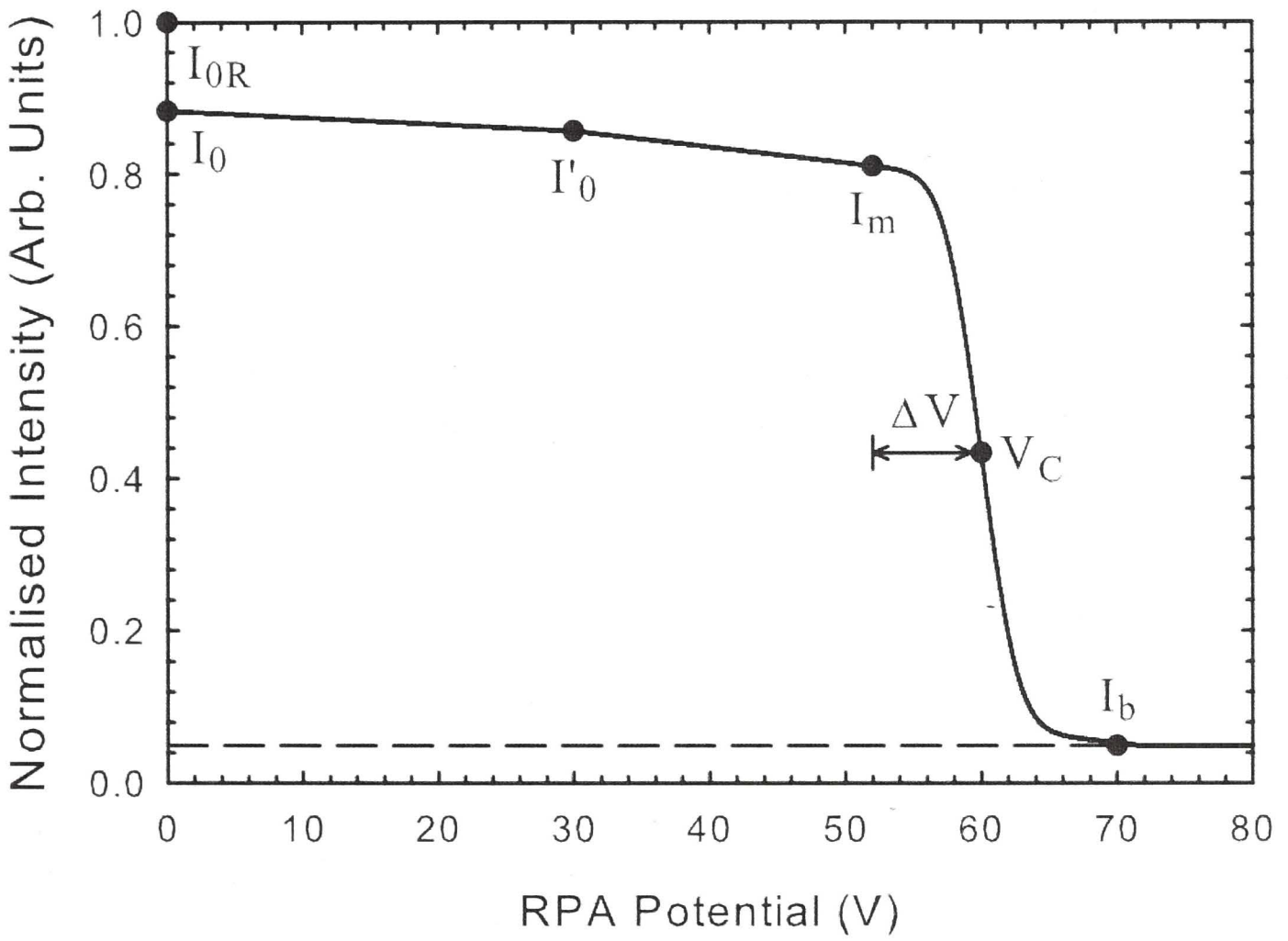

Figure 4.1: A schematic parallel energy loss curve indicating the parallel energy loss associated with each intensity used to calculate the various cross sections. A detail description of the intensities is given below, but briefly, I_{0R} is the intensity of scattered plus unscattered positrons, I_0 is the intensity of positrons which have not undergone positronium formation, I'_0 is the intensity of positrons which have not a specific scattering process (see below), I_m is the intensity of positrons which have not scattered and I_b is the background from the detector.

energy loss diagram is shown in figure 4.1. The retarding potential (V) is depicted with relation to the measurement of the beam intensities; I_{OR} and I_m. Generally, the amount of attenuation of the positron beam due to the target gas was set to < 10 %, but shown as $\sim$ 20 % in the figure 4.1. I_{OR} is determined by setting the gas cell to the scattering energy of interest ($E_{cell} = eV_{cell}$) and setting the retarding potential analyser (RPA) to zero, thereby allowing all positrons, scattered and unscattered, to be detected by the microchannel plate (MCP) assembly. Backward scattered positrons are reflected into the forward direction by an element just before the scattering cell. I_m is determined by setting the analysing RPA potential to just below the incident beam or ΔV below the beam energy, E_T, such

that the scattered beam is differentiated from the unscattered beam. The value of ΔV is chosen between 3 and 5 σ of the beam parallel energy width, see equation 3.3 of §3.5. This results in two measurements of the positron beam intensity, the total beam, scattered and unscattered, and the unscattered beam. Background measurements and issues relating to the finite energy width of the positron beam are discussed below (see § 4.7 and § 4.8).

4.3 Positronium Formation Cross Section

The binding energy of the positron-electron bound state or positronium (Ps), is 6.80 eV or 0.250 Hartrees. Positrons traversing the gas cell will only form Ps if their energy is above the formation threshold ($E_{Ps} = E_{IP} - 6.80eV$), as discussed in Chapter 2. The Ps formed in the scattering cell will have a maximum kinetic energy defined by the energy sharing with the residual ion [85]. The bound state of Ps is neutral and thus will not be confined radially by the magnetic field, resulting in diffusion of the Ps to the chamber walls where it will annihilate. A forward scattered positronium atom, with a kinetic energy of 200 eV, will traverse less than a metre (at the mean lifetime) before annihilating in flight (p-Ps, 0.74 mm and o-Ps, 0.84 m). Therefore few Ps atoms have sufficient energy to travel to the MCP before annihilating. This results in a loss of positrons from the beam and is dependent on the scattering energy. Measuring the number of positrons which have traversed the scattering cell below the threshold for Ps formation, and above this threshold, allows the positronium formation cross section to be determined, and the measurement to achieve this is shown schematically in figure 4.1. An attenuation factor can be determined which scales the grand total scattering cross sections [20],

$$\sigma_{Ps} = R_{Ps}\sigma_{GTCS}. \tag{4.10}$$

The parameter R_{Ps} is determined as a ratio of the total attenuation of the positron beam and that which is solely due to the formation of positronium,

$$R_{Ps} = \frac{I_{OR} - I_o}{I_{OR} - I_m}. \tag{4.11}$$

The ratio, R_{Ps}, describes the amount of positrons lost to the formation of positronium and thus the Ps formation cross section for any atom or molecule, which has an ionisation potential above the binding energy of Ps, can be determined using this method. Figure 4.1 shows a schematic diagram of an example measurement of the parallel energy loss, indicating each intensity required to determine R_{Ps} in equation 4.11, and thus the postironium formation cross section.

I_{OR} is a measurement of the entire beam intensity as defined in §4.2. I_o is a measurement of the beam intensity at the scattering energy of interest, with the retarding potential analyser set to zero such that the entire beam, scattered and unscattered, is measured by the detection system (MCP), but does not include positrons lost to Ps formation. If positrons are lost due to the formation of positronium at the scattering energy,

I_o will be less than I_{OR}. The definition of I_m is the same as that defined in §4.2.

4.4 Elastic Differential Scattering Cross Section

A positron which undergoes elastic scattering in the scattering cell (SC) loses energy in the parallel direction. None of the incident energy is lost to the target atom or molecule, but rather the motion relative to the field is altered such that energy is conserved, as given by equation 4.4. The scattering angle of the positron is related to the energy along the axis of the confining magnetic field,

$$\theta = cos^{-1}\sqrt{\frac{E'_{||}}{E_c}}. \tag{4.12}$$

The relation of the parallel energy loss to the scattering angle allows the elastic scattering cross section to be determined when only elastic scattering is possible, since the number of positrons can be measured as a function of the parallel energy loss, $I_C(E_{||})$. Consider a positron with initial energy components $E_\perp \sim 0$ eV and $E_{||} \sim E_c$. If the positron elastically scatters through angle θ, the relationship between $E_{||}$ and $E_\perp$ changes. For a total scattering energy of E_c, the energy balance becomes,

$$E'_{||} = E_c cos^2\theta, \;\; E'_\perp = E_c sin^2\theta. \tag{4.13}$$

By measuring the parallel energy loss the angular dependence can be determined via the mapping in equation 4.12, where θ is the scattering angle. The elastic differential cross section was determined using [38, 86],

$$\sigma_{DCS}(E_c, E_{||}) = \frac{1}{nl}\frac{I_s}{I_o}d\Omega, \tag{4.14}$$

$$= \frac{\sqrt{E_{||}E_c}}{\pi n l I_o}\left(\frac{dI_C(E_c, E_{||})}{dE_{||}}\right), \tag{4.15}$$

where I_s is the intensity of positrons scattered with energy $E_{||}$ and $d\Omega = 2\pi sin\theta d\theta$, for an unoriented target, where θ is the scattering angle as defined in equation 4.13. The scattering cell is set to a potential corresponding to a collision energy of E_c. The parallel energy loss intensity, $I_C(E_c, E_{||})$, is measured with the RPA. The derivative of $I_C(E_{||})$ is proportional the differential scattering cross section. The absolute normalization is determined from the beam intensity (I_o), number density (n), length of the scattering cell (l), scattering energy (E_c) and the parallel energy ($E_{||}$). The integral of equation 4.14 yields the grand total scattering cross section when only the total elastic scattering channel is open. Otherwise, it is the magnitude of the elastic scattering cross section.

The relationship between the parallel and collision energies and the scattering angle given in equation 4.12 is bounded between 0 and 90 degrees. Positrons which scatter at angles higher than 90 degrees are scattered in the backwards direction. These positrons

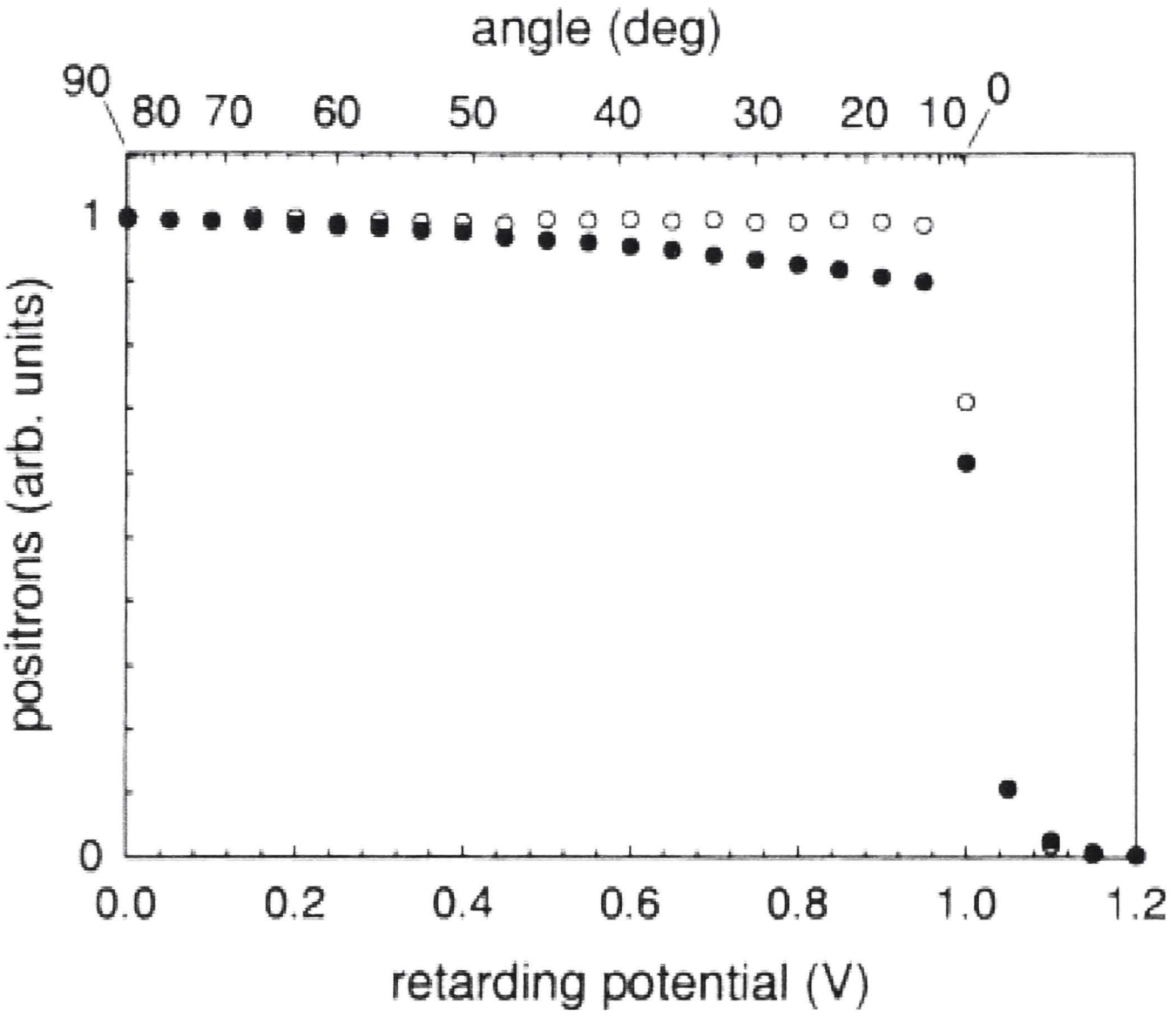

Figure 4.2: An example parallel energy loss curve with corresponding scattering angles from Sullivan *et al.* [38]. The open circles are the energy loss of the positron beam with no gas in the scattering cell and the filled circles correspond to gas in the scattering cell.

are reflected by the RPA prior to the SC and traverse the SC a second time. Hence, these positrons are 'folded' about 90 degrees so the measured elastic scattering cross section is folded about 90 degrees, and the cross section is actually a measure of scattering at $\theta + (180 - \theta)$ degrees. The target density is maintained as low as possible to limit multiple scattering effects or within the single scattering approximation.

4.5 Total Elastic Scattering Cross Section

The determination of the differential elastic scattering cross section was described above. In addition, the total elastic scattering cross section can be determined as a function of the incident positron energy. Positrons which have undergone elastic scattering are distinguished from those that have undergone other types of scattering by using the RPA, to discriminate positrons as a function of their parallel energy loss in combination with the adiabatic invariant given in equation 4.6. Figure 4.2 is an example of the parallel energy loss used to determine an elastic differential scattering cross section as discussed previously. The integral measurement is analogous to determining the grand total scattering cross section described previously in §4.2. Here the ratio of the number of positrons which are scattered elastically versus the total number of scattered positrons is used to determine

the total elastic scattering cross section,

$$\sigma_{Elastic} = R_{Elastic}\sigma_{GTCS}, \tag{4.16}$$

with

$$R_{Elastic} = \frac{I'_o - I_m}{I_{OR} - I_m}, \tag{4.17}$$

where I_{OR} and I_m have been defined previously and I'_o is the number of positrons in the beam which are either scattered elastically or are unscattered, see figure 4.1.

Various scattering processes are available at different incident energies so care must be taken to determine where this method is applicable. For atoms, in particular the noble gases, the elastic scattering cross section is effectively determined by subtracting the positronium formation cross section from the grand total scattering cross section below the first electronic excitation threshold, or until the end of the Ore gap as discussed in Chapter 2. Below the first electronic excitation only three channels are open: annihilation; which is negligible, positronium formation and elastic scattering. For the case of positron scattering from molecules, the total elastic scattering cross section can be determined below the first electronic excitation, but must be considered as a quasi-elastic scattering cross section since, for the experimental parameters used in this work, it includes vibrational and rotational excitations (§7.2.3).

Above the first electronic excitation the parallel energy loss contains both elastic scattering and scattering due to electronic excitation. The mixing of the two (or more) scattering channels in parallel energy loss results in equation 4.13 be modified as,

$$E'_{||}(\theta) = E_c cos^2\theta + \sum_n^N (E_c - E_n^i)\chi_n(\theta), \tag{4.18}$$

where χ_n correspond to the angular dependence of the n^{th} inelastic scattering channel and E_n^i is the threshold energy for the excitation of the n^{th} inelastic channel. The overlap of the elastic and inelastic channels can be solved by changing the magnetic field magnitude at the retarding potential analyser (RPA). This is possible because the ratio between the perpendicular energy and the magnetic field are a constant, or adiabatically invariant, due to the slowly changing magnetic field. Since γ is a constant, energy conservation can be used to determine the relationship between the parallel energy, which is determined by the RPA and the magnetic field, see equation 4.6.

When the magnetic field in the RPA is less than that in the scattering cell, $E_\perp$ is converted back to $E_{||}$, but the total energy loss remains fixed. This allows for the separation of the elastic and inelastic channels [38, 75] because the parallel energy loss due to the angular scatter is reduced, but the total energy loss due to the collision remains the same, E_c. The ratio of the magnetic field in the analyzer to that of the scattering cell, or M ratio described above in equation 4.7, determines the compression factor; the larger the

value of M, the greater the amount of compression,

$$E'_{||} = \frac{E_{||}}{M}, \tag{4.19}$$

The required M to separate the elastic scattering channel from electronic excitation is dependent on the scattering energy of interest and the threshold energy of the first electronic excitation. An example of this compression is shown in figure 4.3. When a high field ratio (M) is applied, the excitation threshold is seen as a step in the parallel energy loss. If the M ratio is high enough the elastic scattering can be compressed below the threshold (in the $E_{||}$ distribution), and the elastic and inelastic scattering channels can be separated. Judicious selection of parallel energies at which positron numbers are measured is required to accurately determine the cross section.

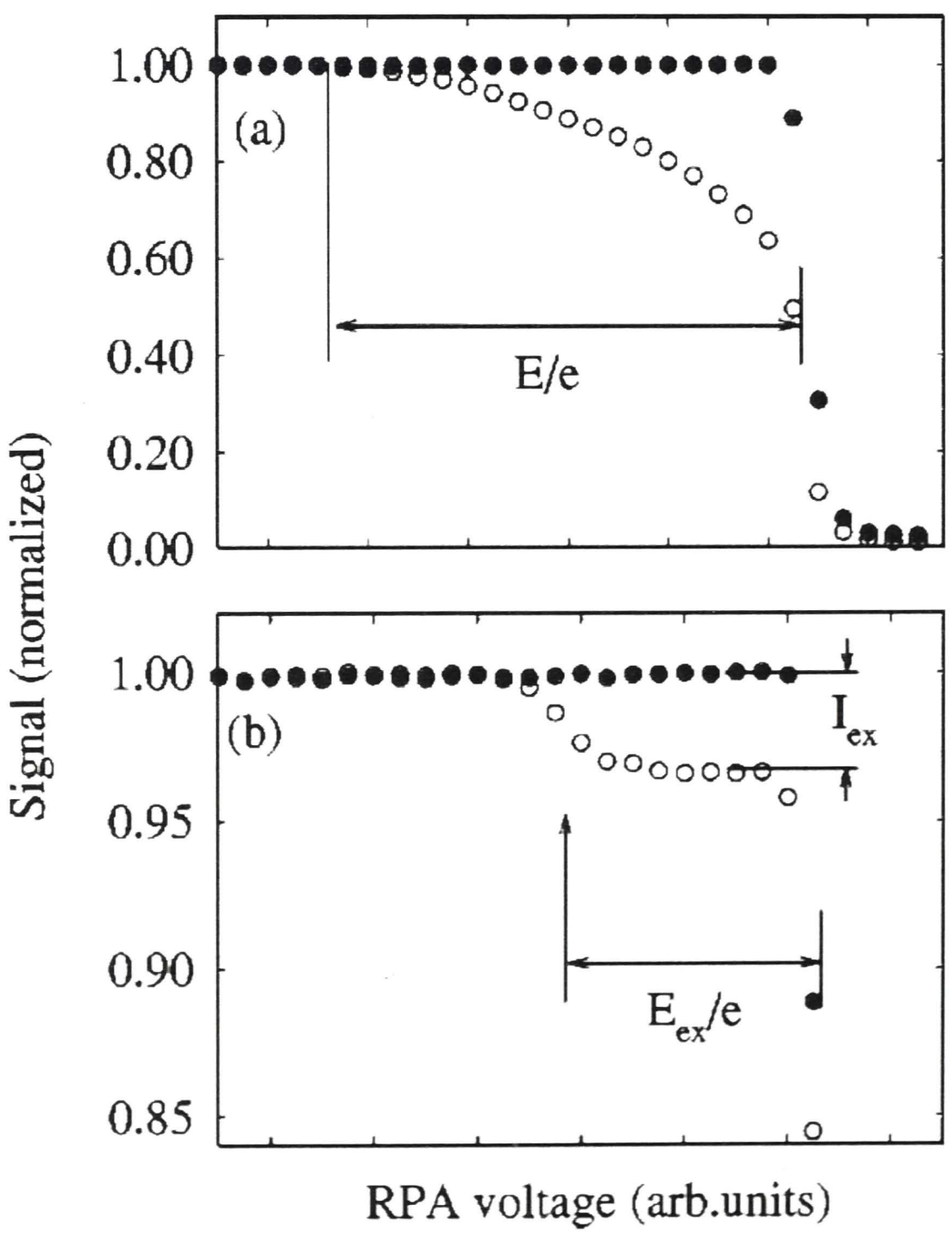

Figure 4.3: Parallel energy loss spectrum for two magnetic field ratios (M): (a) M = 1, and (b) M = 35: from Sullivan *et al* [38].

4.6 Total Inelastic Scattering Cross Section

The total inelastic scattering cross section can be determined in a similar manner to the total elastic cross section. A field ratio or M value between the retarding potential analyser and the scattering cell is used to compress the elastic scattering to below the first electronic excitation, completely separating elastic processes from energy loss collisions as discussed above. The expression used to calculate the total inelastic cross section from the experimental measurements is,

$$\sigma_{inelastic} = R_{inelastic}\sigma_{GTCS}, \tag{4.20}$$

with the ratio,

$$R_{inelastic} = \frac{I_o - I'_o}{I_{OR} - I_m}. \tag{4.21}$$

The intensity measurements in equation 4.21 are defined in the same manner as previously. Thus the ratio in equation 4.21 defines all positrons undergoing inelastic collisions normalized to the total attenuation. The total inelastic cross section can be measured using a moderate field ratio over a range of energies, but this range is dependent on the electronic configuration of the atom or molecule of interest. This cross section will contain all electronic excitations and ionisation processes for an atomic target, but will not contain vibrational or rotational scattering channels for a molecule. The same intensity data used to determine the total elastic scattering cross section can be used to calculate the total inelastic cross section. At high energies, well above the ionisation potential of an atom or molecule, the ionisation channel will likely dominate the total inelastic scattering cross section.

Table 4.1: Electronic excitation thresholds for positron scattering from Helium and Hydrogen.

Target	1^{st} (eV)	State	2^{nd} (eV)	State
He	20.6	$2\,^1S$	21.2	$2\,^1P^\circ$
H_2	11.3	$B\,^1\Sigma$	12.3	$C\,^1\Pi$

When the M-ratio is high enough, individual electronic excitation and ionisation processes can be resolved. This has been demonstrated for a number of targets, but of interest in this thesis are the results for helium [87] and molecular hydrogen [88], whose first two electronic excitation thresholds are listed in Table 4.1.

4.7 Systematic Effects and Uncertainty

Measurements of scattering cross sections using the retarding potential analysis requires a careful consideration of various systematic effects. A series of experimental limitations resulting in non-ideal measurement conditions and methods for removal are reviewed below.

Density Measurements

The target density, n, is determined from the measurement of the scattering cell (SC) pressure. The capacitance manometer determines the pressure by measuring the change in capacitance between a metal diaphragm and a fixed electrode. The manometer volume is maintained at a fixed temperature of 45 degrees C. A temperature compensated amplifier provides an analog signal which is coupled to an analog input of the data acquisition computer to read the SC pressure. Two additional parameters are required to determine the absolute value of the pressure within the SC and the uncertainty in the pressure. Firstly, the drift in the measurement of the zero of the manometer as a function of time. Secondly, the difference in the measured density at the manometer and the density in the scattering cell due to the difference in the temperature between them.

Density Measurements: *Baratron Zero Drift*

Despite temperature compensation, the measured zero value drifts with time and the effect of this drift on the density measurement depends on the absolute magnitude of the density. However, this drift can be measured and removed from the measurement of the density during an experimental run. As seen in figure 4.4, the zero drift has a primarily diurnal cycle. The peak-to-peak value can be used as the uncertainty on the zero value. The manometer is covered by an insulated box to mitigate against temperature fluctuations. Fluctuations in the zero value are $\pm$ 0.03 mTorr. If the zero is outside of this range, the manometer zero is reset by pumping on the system until the pressure is less than 10^{-6} Torr and reseting the manometer controller.

Practically however, the zero value is measured before and after a cross section measurement and it is removed from the measured value of the density. Generally the density in the scattering cell is set to provide $\sim$ 10 % scattering, and depending on the target of interest, the baratron zero value can be negligible or a significant fraction of the measurement, requiring an estimation of the uncertainty. This is done by measuring the baratron value with no gas admitted to the system before and after each experimental run to determine the magnitude of the drift. The uncertainty estimate from the drift has been found, under some circumstances, to dominate over the uncertainty on the manometer or Baratron reading and may be due to mechanical vibration in the experimental system rather than temperature fluctuations.

Density Measurements: *Thermal Transpiration*

Thermal transpiration, or the effect of a difference in the density measured between two connected volumes due to a difference in the two volume's temperature, is a systematic effect that can be compensated for, to a degree. In this case, it must be accounted for because the measurement volume or the capacitance manometer vessel is heated to 45°C and the scattering or target cell is at room temperature or 23°C. A correction can be

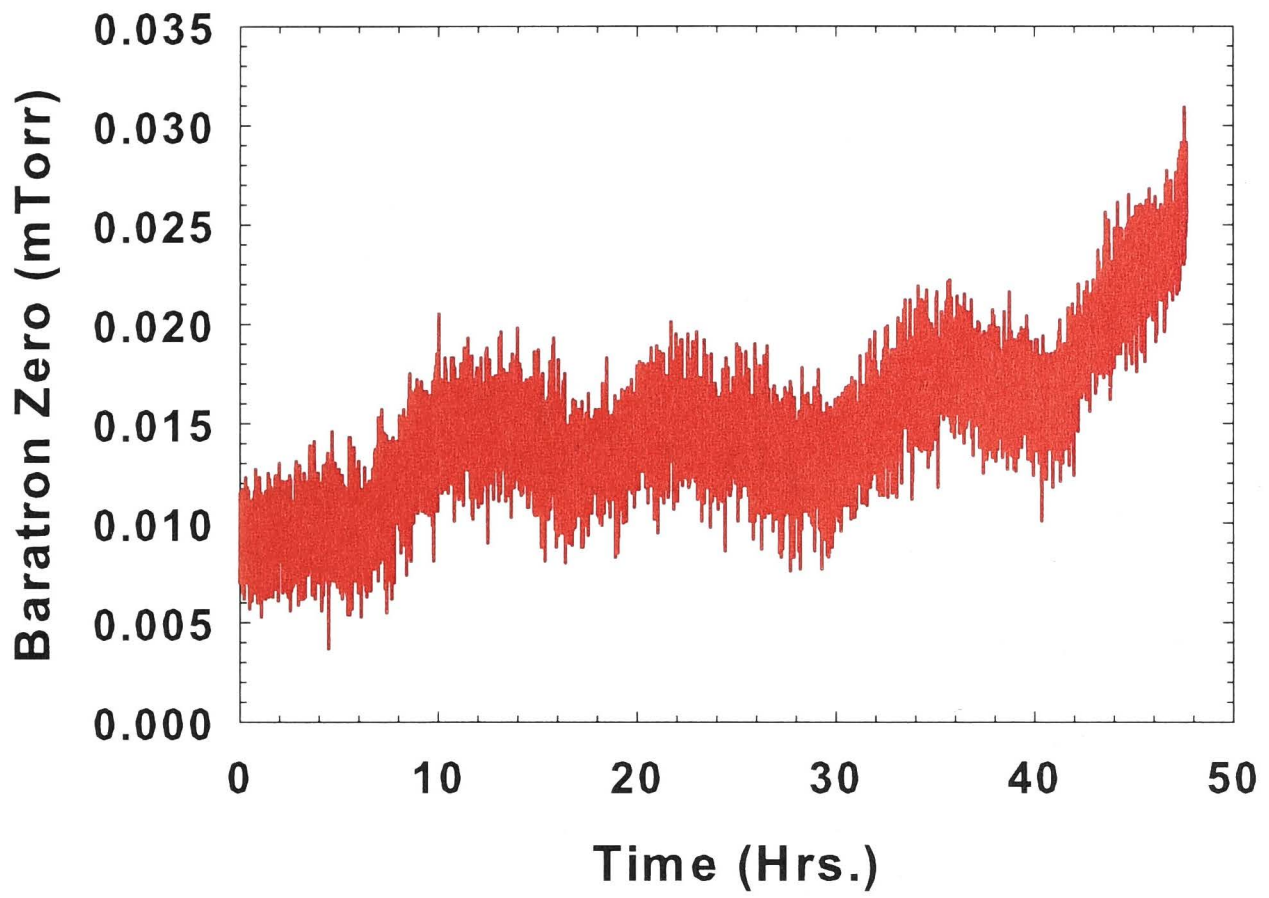

Figure 4.4: An example of the drift in the zero measurement of the Baratron or capacitance manometer pressure.

applied based on the work of Takaishi and Sensui [89], using the formula,

$$\frac{P_1}{P_2} = \frac{AX^2 + BX + C\sqrt{X} + \sqrt{T_1/T_2}}{AX^2 + BX + C\sqrt{X} + 1}, T_1 < T_2, \tag{4.22}$$

where $X = P_2 d$ and d is the diameter of the connecting tube. The coefficients A, B and C are,

$$\begin{aligned} A &= A^* \bar{T}^{-2} \\ B &= B^* \bar{T}^{-1} \\ C &= C^* \bar{T}^{-1/2}, \end{aligned} \tag{4.23}$$

and $\bar{T} = (T_1 + T_2)/2$. Taking T_1 to be the temperature of the scattering cell and T_2 to be the temperature of the capacitance manometer, the correction to the pressure for each target gas can be determined using the parameters in table 4.2. Not all atomic and molecular gases have thermal transpiration correction parameters, such as those in table 4.2, available in the literature, and thus an approximation based on an empirical trend can be used which only requires the collisional diameter of the target molecule,

$$\begin{aligned} A^* &= 1.4 \times 10^4 e^{0.507D}, \\ B^* &= 5.6 \times e^{0.607D}, \\ C^* &= \frac{110}{D} - 14. \end{aligned} \tag{4.24}$$

Table 4.2: Parameters for determining the effects of thermal transpiration on the measured pressure with associated units: A*, $[\times 10^{-5}(^{\circ}C)^2/Torr^2]$; B*, $[\times 10^{-2}(^{\circ}C)/Torr]$; C*, $[\sqrt{^{\circ}C/Torr}]$; Molecular Diameter (D), Å. [89]

Gas	Corrections %	A*	B*	C*	D(Å)
He		$1.4 \sim 1.5$	$1.2 \sim 1.1$	$18 \sim 20$	$2.15 \sim 2.17$
H_2		1.24	8.00	10.6	$2.68 \sim 2.69$
Ne		2.65	1.88	30.0	2.55
H_2O		1.44	0.91	9.91	4.60
NH_3		2	1	8	5
CH_4		14.5	15.0	13	4.09

The coefficients in equation 4.23 can be rewritten in terms of the target's collisional diameter, which can be obtained using a relation determined by Kestin and Leidenfrost [90].

$$\eta = \frac{5\pi}{16}\sqrt{\frac{mk_BT}{\pi}}\frac{1}{\pi D^2}. \tag{4.25}$$

This relates the viscosity of the target atomic or molecular gas to a collisional diameter, which allows the empirical relations of 4.24 to be used to calculate the thermal transpiration. Using either measured coefficients or those calculated from equation 4.24 and 4.25, the magnitude of this effect was no greater than 2 % for the atomic or molecular targets investigated in this thesis. Note that this effect was corrected for before the normalisation of the experimental data.

Trap Gases

One simple requirement of the parallel energy spectrum is that it has a slope of zero between V_{RPA} and $E_T/e - \Delta V$, with no gas in the scattering cell (SC). In terms of the parallel energy loss due to scattering, this corresponds to no positrons undergoing scattering which should be the case when no target gas is admitted to the SC. A non-zero slope in the parallel energy spectrum results in an effective non-zero background in the scattering cross section measurement determined by the methods outlined above. The Surko trap operates with N_2 and CF_4 continuously flowing from the interior of the trap to the exterior. Positrons exiting the trap scatter with this gas mixture in the transport region before the SC at a collision energy of E_T. A measurement of the parallel energy loss, the blue circles in figure 4.5, of the positron beam is performed to determine the background scattering from trap gases in the system before the target gas is admitted for measurement.

The majority of the gas from the trap is contained between the trap and the scattering cell. A teflon ring isolates, or considerably limits, the conductance between the upstream and the downstream section of the apparatus, isolating gases to the region between the trap and the scattering cell. The nl path length is relatively large up until the scattering cell which is evident by the blue circles in figure 4.5 where nearly 15 % of the incident beam is lost due to scattering with trap gases. Those positrons which have scattered prior

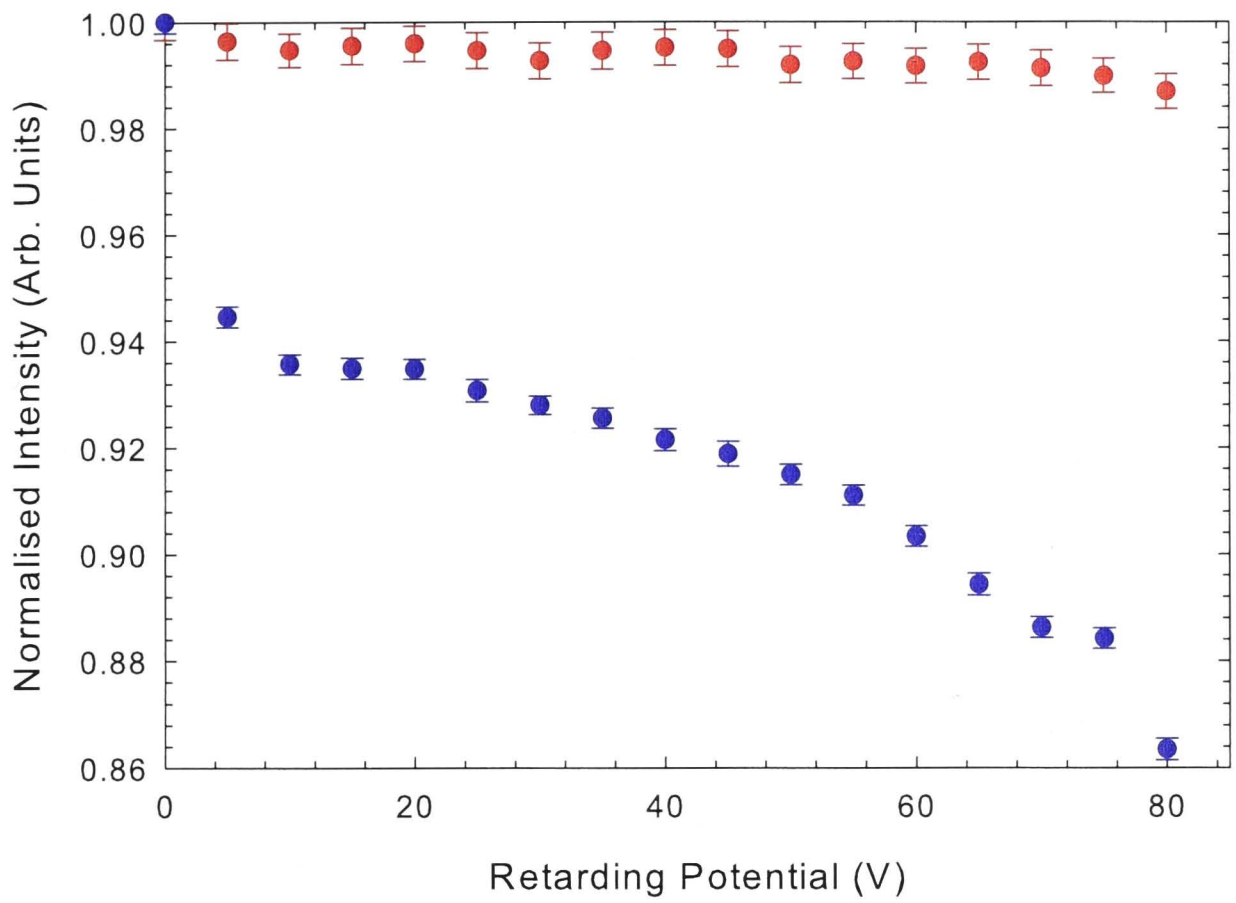

Figure 4.5: A measurement of the parallel energy loss of positrons: blue circles, a measurement of the scattering between the exit of the trap and the SC, and red circles, a measurement over the same parallel energy loss with the RPA just prior to the Scattering Cell set to reject positrons which have scattered.

to the SC are removed by setting the potential of the retarding potential analyser in front of the SC on the "knee" of the cutoff curve or at $\sim$ 80 V in figure 4.5. The resulting positron beam, red circles of figure 4.5, consists of positrons which have not scattered from the trap gases and a small portion which have scattered in the forward direction.

Target Gas

Target gas is expelled from the scattering cell (SC) during an experimental run. Positrons on the exit side of the SC will scatter with this target gas at a collision energy of E_T. This results in a background in the parallel energy loss. An example of this background is shown in figure 4.6, compared to an ideal parallel energy spectrum. Generally, the percentage scattering is set for the target gas at 10 %. The measured background in figure 4.6 is 0.2 %, which would correspond to a background of 2 % of the total scattering in this example. This background is energy dependent and must be measured so it can be removed, as it can change the energy dependence of a measured cross section.

Removal of Background

The atomic or molecular target's electronic configuration constrains the energies or potentials used to determine partial cross sections, as discussed in detail above. A stringent test of the above technique is the measurement about the threshold for a new scattering process, where the cross section is zero below the threshold and non-zero above. If a

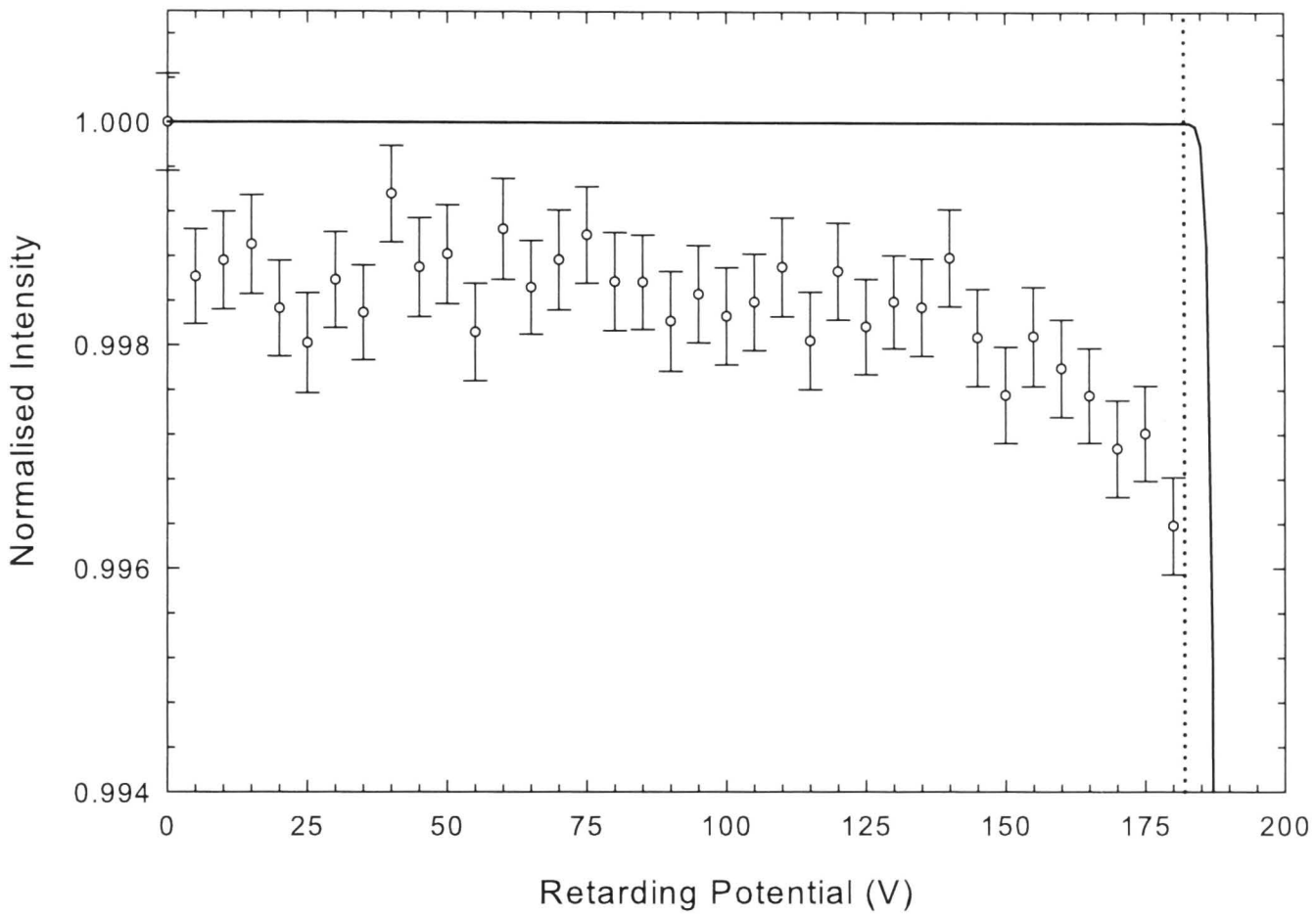

Figure 4.6: A measurement of the parallel energy of the positron beam with a non-zero background.

partial scattering cross section appears to be non-zero below threshold, a background is (likely) present. A prime example of this is shown in figure 4.7, where the total inelastic scattering cross section is measured in molecular hydrogen. As discussed previously, the total inelastic scattering cross section does not differentiate between electronic excitations and ionisation, but there is an energy range where the only contribution to the total inelastic cross section is the first electronic excitation. The raw, or uncorrected, measurement shows a non-zero cross section below the first electronic threshold at 11.3 eV. Since the uncertainty in the absolute energy calibration is $\pm$ 50 meV, the parallel energy loss is clearly indicating a non-zero value below threshold, however, there are no excitation channels open. When the target gas, H_2, is removed from the system and a "gas out" measurement of the parallel energy is taken, a small slope is measured. The gas out measurement is then used to correct the measured data by eliminating the background slope. When this is done, the corrected inelastic scattering cross section is zero, to within the uncertainty on the measurement, below the inelastic threshold as seen in the corrected data in figure 4.7. Above the threshold, the total inelastic cross section is consistent with the only existing measurement of the first electronic excitation from Sullivan *et al.* [34] until the onset of direct ionisation at 15.43 eV, see figure 4.7.

This background correction example requires two measurements; one with target gas and one without, thereby increasing the accumulation time for a particular measurement. It is possible however, to obtain such background information from the parallel energy loss of any measurement of a scattering cross section with only a slight caveat. Recall the

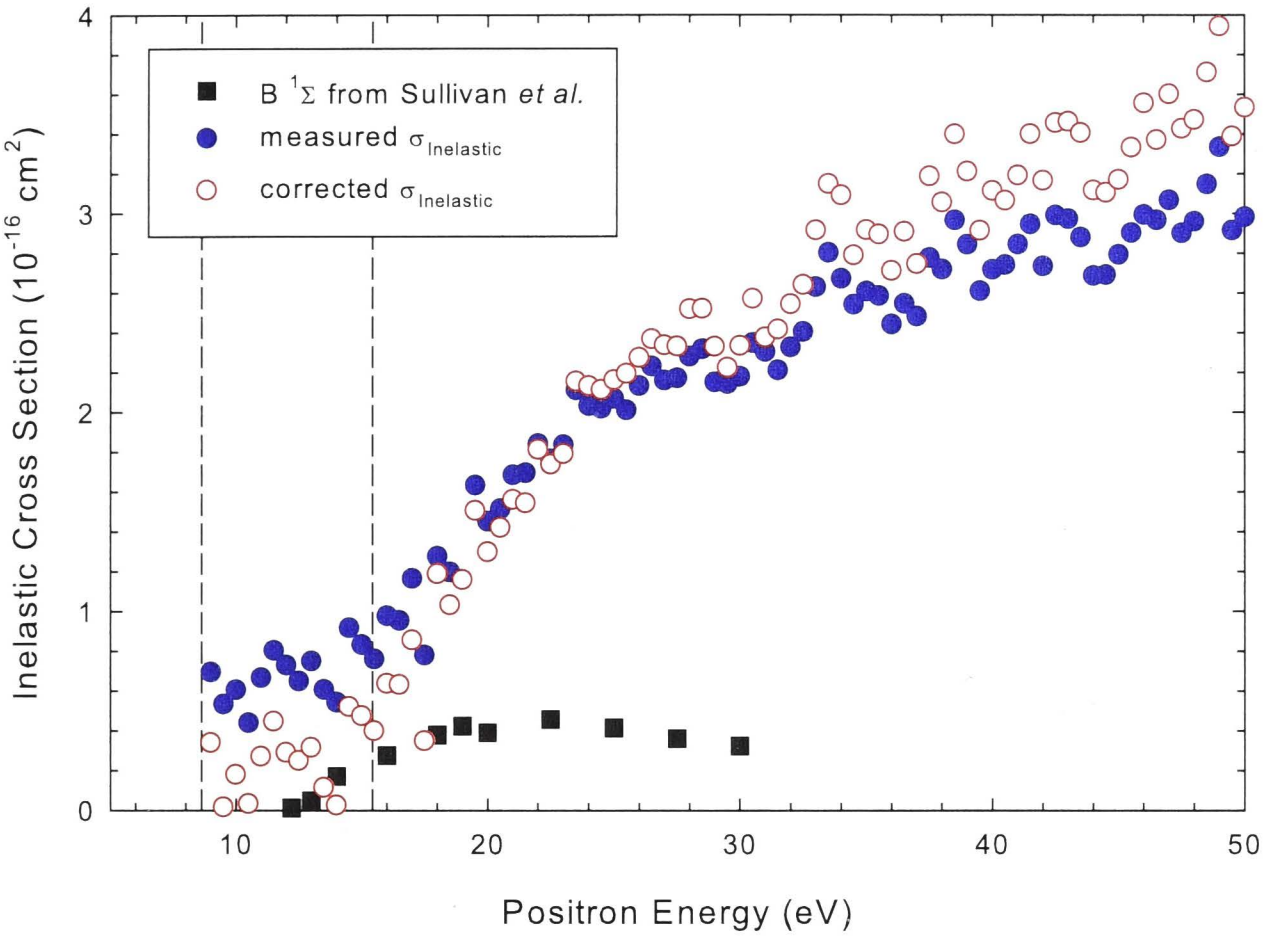

Figure 4.7: Comparison of an uncorrected and corrected measurement of the total inelastic scattering cross section in molecular hydrogen; solid blue circles; uncorrected measurement, open red circles; correction for linear background in the retarding potential or parallel energy loss curve. The error bars have been suppressed as the statistical nature of the data is evident in the scatter in the data. These measurements are compared to the $B\,^1\Sigma$ electronic-state results of Sullivan *et al.* [34].

energy loss diagrams from the preceding sections where intensities were measured for a particular parallel energy loss. Figure 4.1 recreates the previous parallel energy loss curve with a small background. For a scattering energy less than the transport energy, the positron can lose a maximum of the collision energy within the cell. A measurement at an energy loss equivalent to the transport energy in addition to a measurement at the collision energy will be equal if no background scattering is present in the system. Measuring these two intensities and assuming that the slope is linear (not necessarily the case, see chapter 5) allows for the removal of the background scattering present during the measurement. It is important to use intensities measured during the experimental run with the target present in the system, since the target gas may alter the magnitude of the background. However, caution must be taken in using the linear interpolation of the background when strong scattering channels such as ionisation are involved.

4.8 Angular Limitations

The positron beam has a finite energy width which is related to the angular distribution for a given collision energy, see §4.4 equation 4.12. Therefore, some portion of the forward

scattered positrons are not distinguishable from the beam. The minimum, or 'critical', angle that is measurable can be defined as,

$$\theta_c = asin\left(\sqrt{\frac{\Delta E}{E}}\right), \tag{4.26}$$

where, ΔE is the normal energy width of the positron beam and E is the scattering energy set by the potential on the scattering cell. As the scattering energy decreases, the amount of the angular scatter included in the total scattering cross section measurement decreases since the energy width of the beam is fixed, and becomes a significant portion of the scattering energy. Therefore, the experimental results will always be lower than the true cross section as discussed in Sullivan *et al.* [91]. Theoretical results can be used to estimate the percentage of the cross section which is missing. This method has been used in a number of publications [7–9, 92] and is also employed in chapter 7.

Positrons which scatter near 90° have a longer path along the scattering cell. If the collision energy is above the positronium formation threshold, these positrons may undergo another collision and form Ps, constituting a loss of positron flux. Those that are not lost, due to Ps formation, may scatter a second time into a different angle. This leads to a reduction in the measured scattering at high angles, which can only be mitigated by decreasing the percentage scatter and thereby increasing the accumulation time. Specific examples will be discussed in chapter 5. Both the inability to distinguish the unscattered beam from forward scattered positrons at low parallel energies and loss of the scattered positrons near 90°, result in the measured elastic differential scattering cross section being distorted with regards to its true angular behaviour.

For integral measurements, such as the grand total scattering cross section, only the missing elastically scattered positrons at forward angles, which cannot be distinguished from the incident beam, lead to an underestimation of the GTCS. An example of this for molecular hydrogen is given in chapter 7. There a series of elastic differential scattering cross sections are compared to theoretical results to provide an estimate of the missing component of the cross section [34].

4.9 Statistical Uncertainty

The positron beam is pulsed at a rate of $\sim$ 100 Hz, as discussed in Chapter 3. Due to the decay of the moderator, also discussed in Chapter 3 and shown in figure 4.8 (a), the desired cross section is measured on a time scale much sorter than the decay time. The duration of a single measurement scan, in energy for example, is $\sim$ 1 minute. Each positron intensity is measured $\sim$ 100 times, and summed. The uncertainty due to the decay of the moderator is negligible since the sampling time is much less than the decay time. The pressure in the scattering cell is read out from the Baratron, once per scan. This is used to determine the cross section for the single measurement scan. A typical measurement will consist $\sim$ one thousand scans and a histogram is shown in figure 4.8 (b), where the histogram of the raw

data is compared to the histogram for the moderator decay corrected data. The normal or Gaussian nature of the corrected data is clearly seen and has been fitted using a normal distribution. The cross section is determined from the mean of all the measurements or scans, and the statistical uncertainty of each measurement is determined by the standard deviation [93],

$$\sigma \simeq \sqrt{\frac{1}{N-1}\sum_i (x_i - \bar{x})^2}, \tag{4.27}$$

where N is the number of scans.

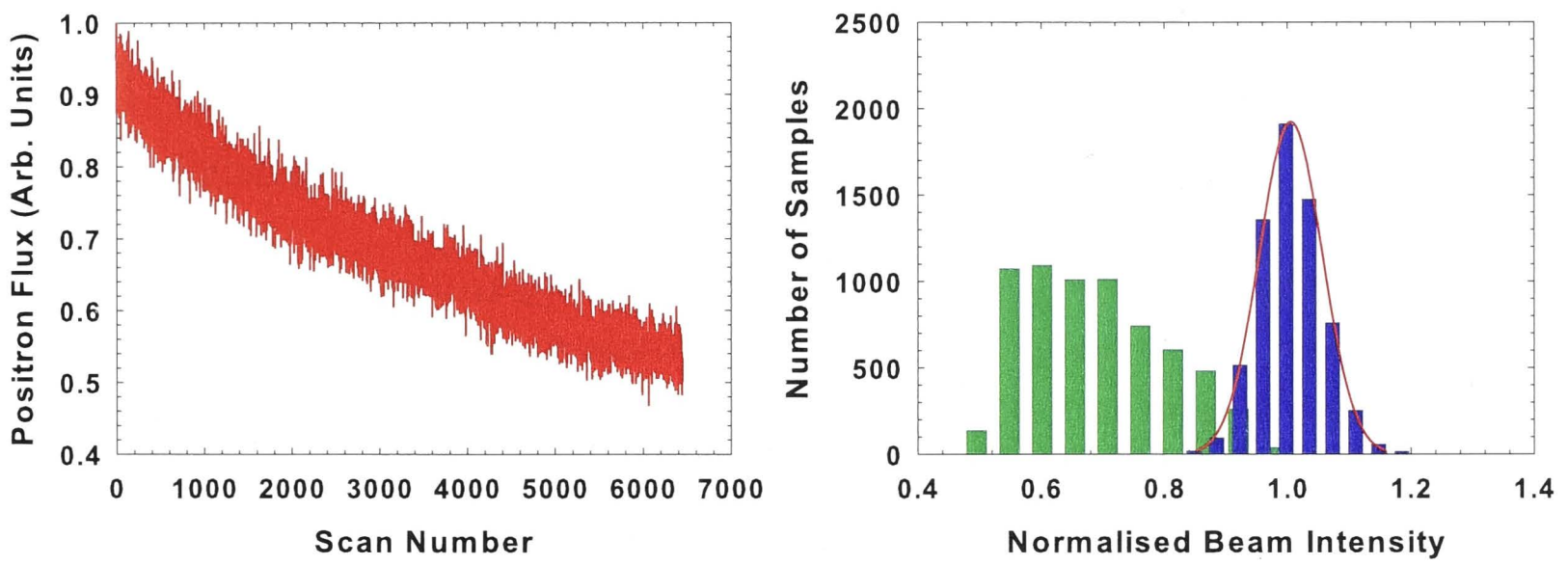

(a) Measured Intensity

(b) Histogram of the Measurement

Figure 4.8: (a) An example of moderator decay observed in the measurement of the beam intensity (red line). (b) Comparison of the histogram of the intensity measurement without (green) and with (blue) correction for the moderator decay. A Gaussian, or normal, distribution, has been fitted to the experimental data.

4.10 Final Remarks

All data presented subsequently has been carefully analysed with the above considerations in mind, and the uncertainties presented are absolute, unless otherwise stated. Any effect of the limitations in this experimental technique will be treated as part of the discussion of the results in the following chapters.

Chapter 5

Helium Elastic Differential Cross Sections

5.1 Introduction

Positron interactions with the helium atom are amongst the most fundamental investigations of the interaction of antimatter with matter. Experimentally, they provide the most tractable studies of a simple atomic system, which can in turn be used to test contemporary quantum scattering theory. In recent years, results from four state-of-the-art theoretical calculations [50, 87, 94, 95] of positron scattering from the helium atom have converged to within around 10 %, or better, of the total elastic cross section measurements of Mizogawa *et al.* [96]. In a recent review article by Surko *et al.* [22] and in Buckman and Sullivan [97], the experimental work of Mizogawa *et al.* [96], the Kohn variational calculations of Van Reeth and Humberston [98], and the many-body calculations of Gribakin and Ludlow [12], are regarded as amongst the first "benchmark" results in positron collision physics. More broadly however, agreement between state-of-the-art positron scattering experiments from the noble gases; neon, argon, krypton, and xenon, are not in as good an agreement below the positronium formation threshold, and the disagreement can be as high as 30 % [7–9]. There are no other comparable case studies of low-energy scattering of positrons, from an atom or molecule, where there exists this level of accord between experiment and theory.

In the case of the more mature field of electron scattering experiments, helium has provided a broad suite of data that can confidently be compared with state-of-the-art theories [99]. The level of agreement has been uniformly excellent across a range of energies and scattering processes and, as a result, has benefited and aided the development of experimental and theoretical techniques. In recent years a similar scenario has emerged in low-energy positron interactions where much experimental and theoretical progress has occurred in the investigation of the helium total elastic cross-section, as mentioned above. The next, and obvious, step in this process of comparison of experiment and theory is to consider angular differential cross sections (DCS) for elastic scattering. While grand total scattering cross sections can be measured with high absolute accuracy they do not necessarily provide the best platform for comparison with theory as they involve an integration over all scattering angles of the DCS. It is possible that quite different

DCS, when integrated, can lead to a value of the total cross section which lies within the "benchmark" error boundaries of state-of-the-art total scattering measurements. Thus, in principle, measuring absolute differential cross-sections provides a more rigorous test for benchmark theoretical models.

The agreement between theory and experiment, in the notoriously difficult region above positronium formation threshold, has improved recently following some significant theoretical and experimental developments [100]. In particular the development of the two-centre convergent close coupling (CCC) approach [100] has seen a much improved level of agreement with experiment for the total scattering cross section in this region, over that previously provided by a single-centre CCC expansion [50].

The positron-atom scattering system provides experimentalists with the ability to study a number of discrete energy regions where the dynamics of the process are likely to be quite different. These regions include; below the Ps formation threshold, where only elastic scattering is possible, at and above the Ps threshold but below the first inelastic threshold (the Ore gap) where Ps formation is the only other channel open, and above the threshold for inelastic (excitation and ionization) processes. It continues to be a challenge for theorists to predict the interplay between two (or more) open scattering channels, and the recent experiments on cusp formation, in the total elastic cross section at the Ps threshold, demonstrate this quite clearly [7]. It is also a challenge to accurately calculate Ps formation as there are several centres of symmetry in the final state that have to be dealt with. The higher (intermediate) energy range is also particularly interesting for positron-atom scattering because in many cases the combined cross-sections for Ps formation and ionization become appreciably larger than the elastic cross section and, as a result, cross channel absorption effects may manifest themselves significantly.

Low energy DCS measurements for positrons scattered by atoms were first performed on Argon by Coleman *et al.* [101]. The only published DCS data for absolute elastic positron scattering from helium is that of Chaplin *et al.* [102] who used a Time-of-Flight (ToF) technique at energies between 40-80 eV. In the present work we present absolute ("folded") DCS at several energies between 1 and 30 eV, where the folded nature was discussed in Chapter 4.

5.2 Experimental Considerations

The techniques used to determine the elastic or angular differential cross section were discussed in Chapter 4, and a few of those considerations will be expanded upon as they are of utmost importance in understanding the comparisons between experiment and theory.

The maximum energy that can be transferred from $E_{\parallel}$ to $E_{\perp}$ in an elastic scattering event is the collision energy, E_c, which corresponds to a scattering angle of 90°. Positrons scattered at 90° have infinite scattering path length (l), since they remain stationary, orbiting about a fixed point inside the scattering cell. Likewise, the scattering path lengths are greatly increased for those scattered near 90°. These positrons will either undergo a

second scattering event which could include Ps formation, and thus loss from the beam, if that channel is open. Using theoretical estimates of differential cross sections for the angular region near 90° shows that measurements above $\sim$ 80° may not be accurate. Figure 5.1 are the results of a Monte Carlo simulations using theoretical Argon DCS at two energies which had markedly different angular dependences [38]. For a reasonably forward peaked DCS, the "measured" shape is approximately correct with only slight deviations at angles approaching 90°, whereas, for a relatively flat, or s-wave dominated DCS, the discrepancy is dramatic. Positrons scattered into angles above about 75° appear to scatter a second time into more forward angles thereby inflating the measured forward angle scattering. The comparison between the two scattering probabilities (0.1 and 0.2) is distinguishable in the top panel, but not in the bottom panel and also appears to be DCS dependent or shape dependent. Of course, the density cannot be decreased to zero since the attenuation is proportional to that quantity, and is related to the obtainable uncertainty, as discussed in Chapter 4, so a compromise must be reached.

Since Ps formation is a particle-loss process (in terms of a magnetically confined positron beam), we are able to measure the elastic cross-section directly through the Ore gap region, up to 20.62 eV in helium. For measurements above the first singlet excitation threshold ($2\,^1S$ at 20.62 eV) a field ratio, between the magnetic field at the SC and that at the RPA, is required to compress the parallel energy loss or angular scattering below this threshold such that the two processes are separated, as explained in Chapter 4. The field ratio also increases the parallel energy distribution of the incident beam resulting in a degradation of the angular resolution and the minimum forward angle which can be measured. The first electronic excitation in helium is relatively high in energy, allowing a correspondingly small field ratio to be used to determine the angular scattering at 30 eV, for example. Therefore, the degradation is small and does not significantly affect the results in this case.

Path Length

The positron traverses the scattering cell in a helical path governed by the equations of motion for a charged particle in a magnetic field. This helical path can be related to the perpendicular and parallel energies through the gyroradius and conservation of energy, respectively. When the grand total scattering cross section is calculated (in the integrated experiment), the path length is assumed to be the linear length of the scattering cell (L) or the length along the guiding magnetic field because the field strength is large enough that the physical length of the scattering cell is much larger than the gyroradius or $r_g \ll L$. The beam defining aperture is 4.5 mm and the scattering cell aperture is 5 mm so that even at perpendicular energies of 60 eV, positrons near the edge of the aperture radially will still be transmitted unless they scatter more than once, which will depend on the density and the value of the differential scattering cross section.

Any alteration of the path length of the positrons through the scattering cell from the geometric length will alter the measurement of the absolute differential scattering

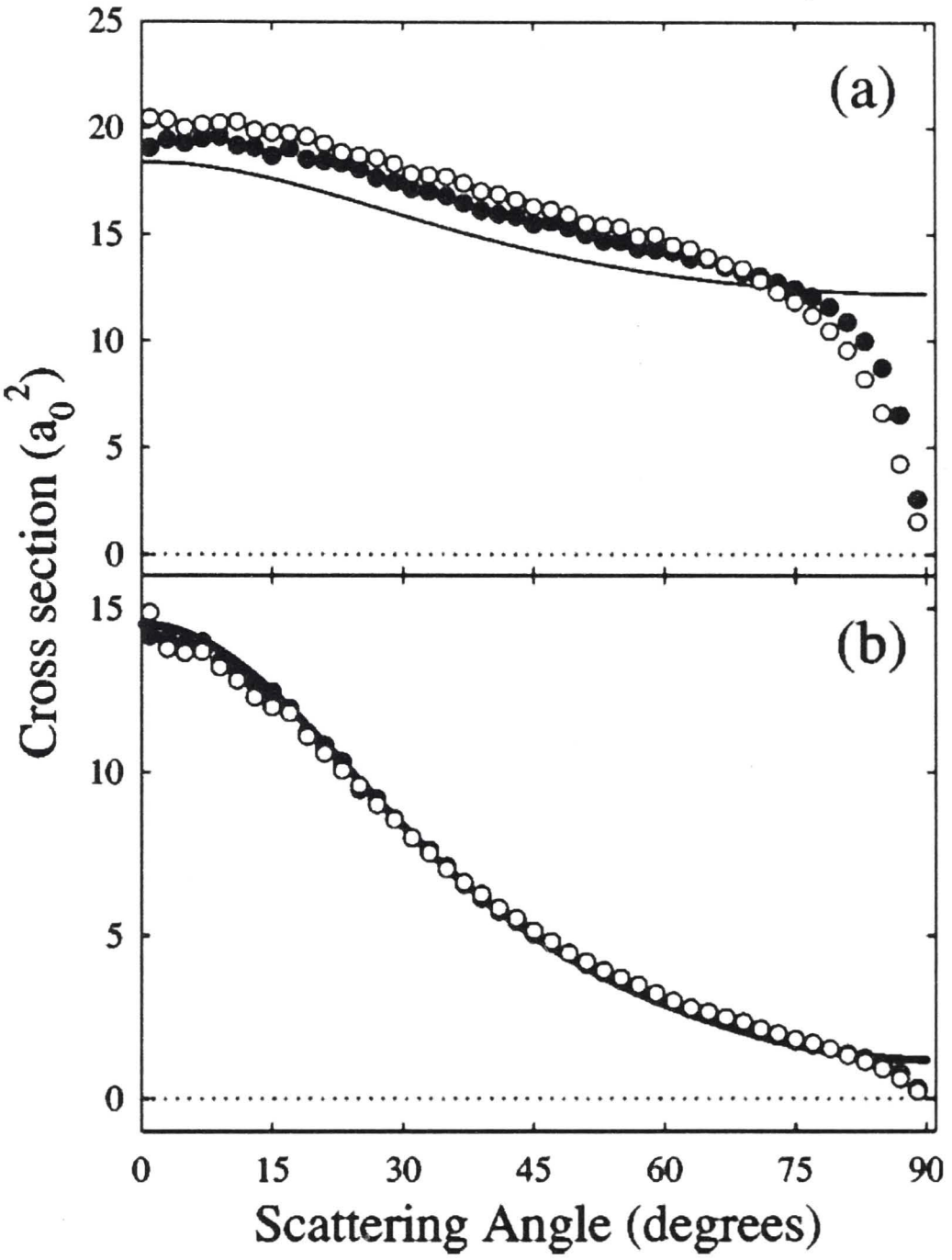

Figure 5.1: A figure from Sullivan *et al.* [38] showing the results of Monte Carlo simulations for two different elastic differential scattering cross sections in Argon. The top panel (a) is a model DCS which has an appreciable magnitude near 90° and bottom panel (b) is a model DCS which has little magnitude near 90°. The open circles are a scattering probability within the cell of 0.2 and the closed circles are a scattering probability of 0.1.

cross section from the true result, and is of particular importance if this alteration has an angular dependence. This was explored by Sullivan *et al.* [38] using a Monte Carlo simulation using a model DCS. A series of model angular scattering cross sections was used to measure the effective path length due to the angular scattering of the positron from a target. It was found that a nearly flat model DCS resulted in a sizable correction to the path length, whereas, for forward peak angular scattering functions, this effect was smaller, see 5.2. These results demonstrate the difficulty in measuring differential angular scattering which is nearly constant, as a function of scattering angle.

5.3 Theoretical Considerations

The present measurements are compared against a number of theoretical models including a two-centre convergent close coupling approach (CCC), a Kohn variational (KV) calcu-

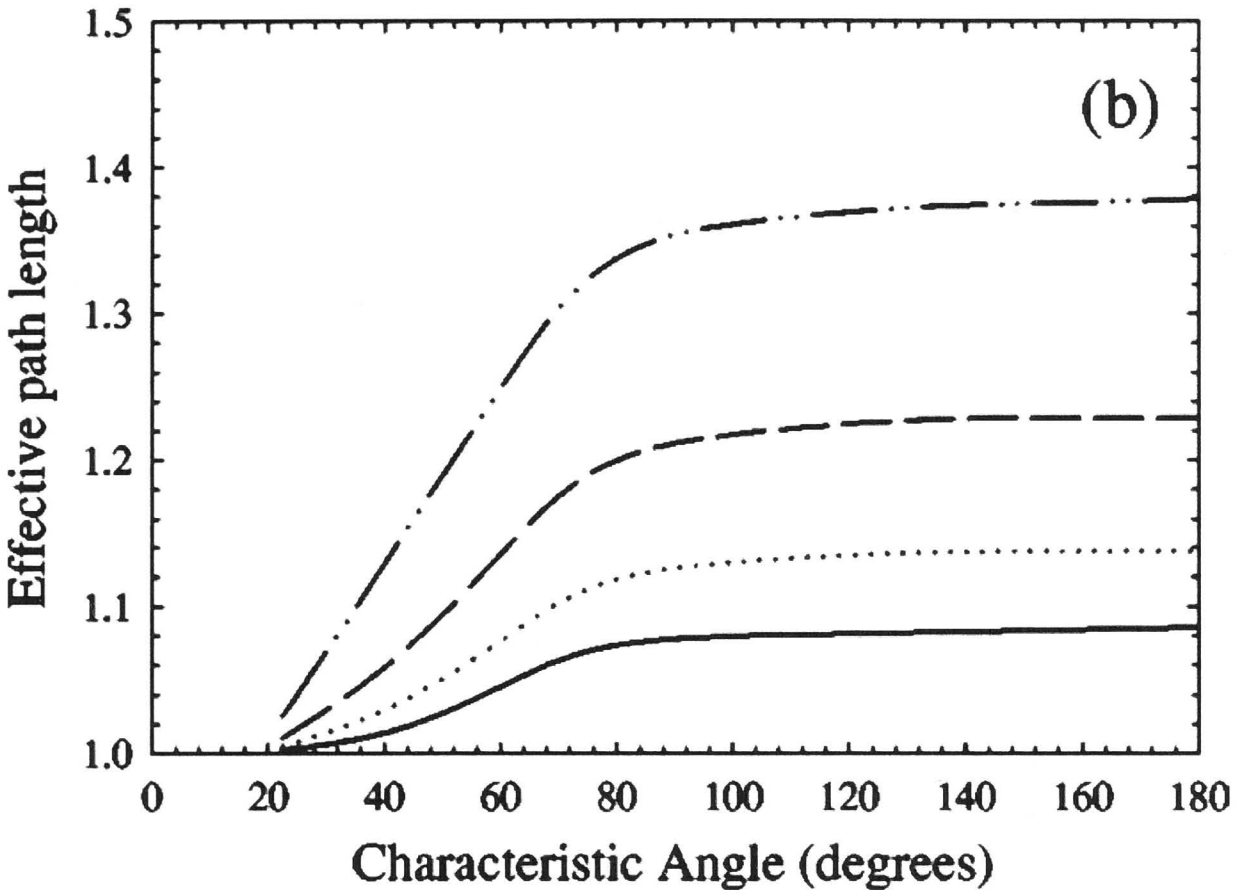

Figure 5.2: Monte Carlo simulation investigating the increase in the path length from Sullivan *et al.* [38]. Effective path length for various total scattering probabilities: solid line; 0.05, dotted line; 0.1, dashed line; 0.2, and dot dot dashed line; 0.4.

lation and a polarized orbital approach (POA). A short discussion of these methods is contained in Chapter 2. The CCC and KV calculations have been described previously in the literature [98,100]. The elastic differential cross sections presented here using the POA were calculated using a non-relativistic polarized orbital method which is an extension of a previous POA calculation. In the original polarized orbital approach of McEachran *et al.* [46], the static potential was calculated using the Hartree-Fock wave functions and an infinite number of multipoles were included in the polarization potential. Here the static potential is calculated using the more accurate frozen-core extended Hartree-Fock procedure and, since helium is not very polarizable, only the dipole and quadrupole polarization potentials are included. Furthermore, both these polarization potentials were scaled to yield the best values in the literature for the dipole and quadrupole polarizabilities, namely $\alpha_d = 1.384$ au and $\alpha_q = 2.282$ au. (The unscaled values of these polarizabilities are $\alpha_d = 1.322$ au and $\alpha_q = 2.326$ au.). The CCC do not reproduce the experimental polarisabilities, with larger discrepancies than those observed in the POA results. These discrepancies are generally decreased or removed by including more states with high angular momentum [6]. Many versions of the CCC method have been used to obtain total and differential scattering cross sections and, with the inclusion of more configurations, and in particular the addition of the multi-centre approach, comes better agreement with experimental results and the very accurate low energy theoretical results of Humberston [98].

5.4 Results

A series of elastic differential cross sections were measured from 1.7 to 30 eV, spanning from the R-T minimum to above the ionisation potential. The measurements include investigations near the positronium formation threshold and in the Ore gap. Comparison is made to the available theory with discrepancies discussed in terms of both experimental and theoretical limitations.

Below Positronium Formation

Comparison between the present high-resolution measurements and the various folded calculations are reasonably good at all energies, but most particularly at energies below 10 eV, presented in figure 5.3. At 1.7 eV, the position of the Ramsauer-Townsend minimum in the total cross section, the folded DCS for the experiment and various calculations are all in reasonably good agreement with each other. However, the most recent, accurate measurements, solid black dots in figure 5.3, indicate a small difference in the angular dependence at forward angles.

The agreement between experiment and theory is nearly as good at an energy of 5 eV, but some differences are evident at this energy. Available theoretical results [100, 103] both indicate that the DCS is nearly a constant between 80 and 90° whereas the current results tend to zero, which is consistent with systematic affects effecting high scattering angles, as discussed previously 5.2.

As the energy increases further, the discrepancies between the theoretical and experimental results become significant. Two different experimental results are shown in figure 5.3 for 10 eV with the red data having a scattering percentage of 10 % and the black data having scattering percentage 3 %. These two results show markedly different energy dependence due to the loss of positrons at high angles rescattering into low angles, as discussed in §5.2. Despite decreasing the scattering percentage in an attempt to eliminate this issue, agreement is still not obtained between experiment and theory. Both theoretical results [100, 103] have a minimum, but at very different scattering angles and due to experimental limitations, no definitive preference for one of the two can be seen.

The agreement between results is much better at 15 eV, see figure 5.3. Whilst the experimental results tend to zero when approaching 90°, which implies an inflation of the forward angles, this appears to be a small effect, and is consistent with §5.2. It appears that both theories and the experimental results have a minimum between 30° and 40°. The agreement at 15 eV is remarkable considering the large discrepancies in the results at 10 eV since both measurements (in black) were taken with scattering percentage of 3 %. This agreement between experimental results appears to be due to the more forward peaked shape of the DCS, as demonstrated with the Monte Carlo results of Sullivan *et al.* [38] in figure 5.1.

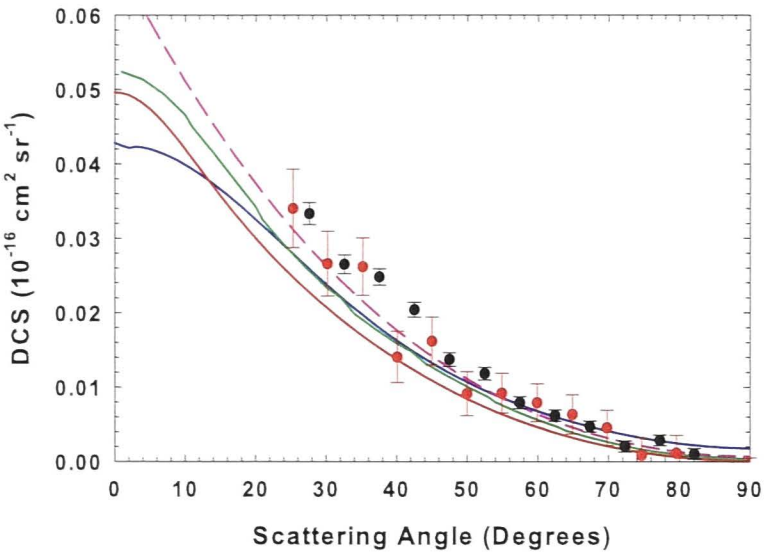

(a) 1.7 eV

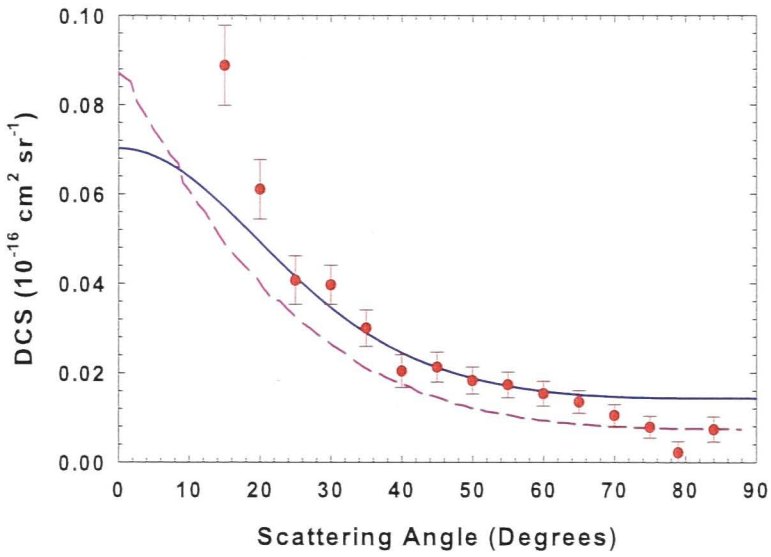

(b) 5 eV

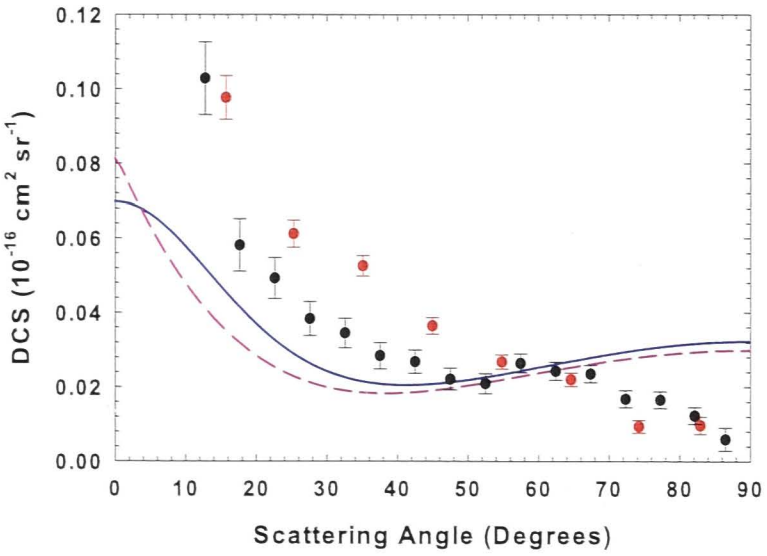

(c) 10 eV

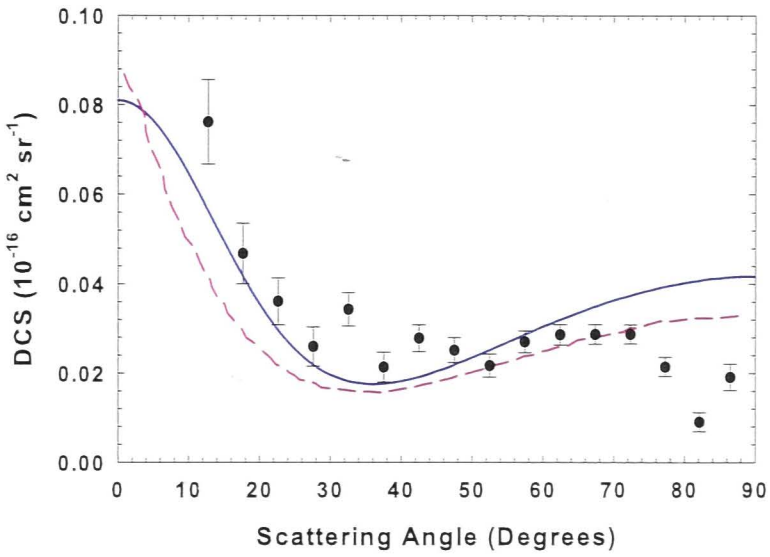

(d) 15 eV

Figure 5.3: Comparison of experimental and theoretical results for positron elastic differential scattering from He. (a) at 1.7 eV: solid circles; current experimental results (red from [70], and black are current results), dashed magenta line; theoretical results (ROP) of McEachran *et al.* [103], solid blue line; theoretical results (single-centre CCC) of Bray [104], solid red line; theoretical results (CCC) of Utamuratov *et al.* [100] (two-centre CCC) and solid green line; theoretical results (KVM) of Van Reeth [105]. (b) at 5 eV: solid circles; experimental results from [70], dashed magenta line; ROP and blue line; two-centre CCC (c) at 10 eV: solid black circles; current experimental results for 3 % scattering, solid red circles; experimental results for 10 % scattering, solid blue line; two-centre CCC and dashed magenta line; ROP. (d) at 15 eV: solid circles, current experimental results; dashed magneta line, ROP; solid blue line, two-centre CCC.

Measurements in the Ore Gap

The experimental elastic differential scattering cross section at the positronium formation threshold is shown in figure 5.4, and compared to the theory of Utamuratov *et al.* [100]. The two are in good agreement between 15 and 70 degrees. As with other DCS results, the experimental results tend to zero at high angles as discussed in §5.2. The magnitude of the Ps formation cross section at threshold is zero and as a result, the loss of positrons that are scattered at high angles to Ps formation should be small and instead they should rescatter to more forward angles as is the case below the Ps formation. This is evident by the measurement of the DCS tending to zero as the scattering angle goes to 90 degrees, which is an indication of multiple scattering, as discussed in §5.2.

The experimental results for the elastic differential scattering cross section for two scattering energies in the Ore gap are shown in figure 5.4 from [70]. The results at the threshold for Ps formation are compared to a CCC [106] calculation, with reasonable agreement between the two results. The results at 20 eV are compared to CCC [106] and ROP [103] calculations. There are differences between the CCC and ROP results, as might be expected since the CCC calculations have included Ps formation channels whereas ROP does not, which is reflected in their reported GTCS. Reasonably good agreement is seen between the experimental and CCC results at 20 eV considering the same assumptions are applied previously, with regards to scattering at 90 degrees. Here, again, the measured DCS tends to zero as the scattering angle increases to 90 degrees.

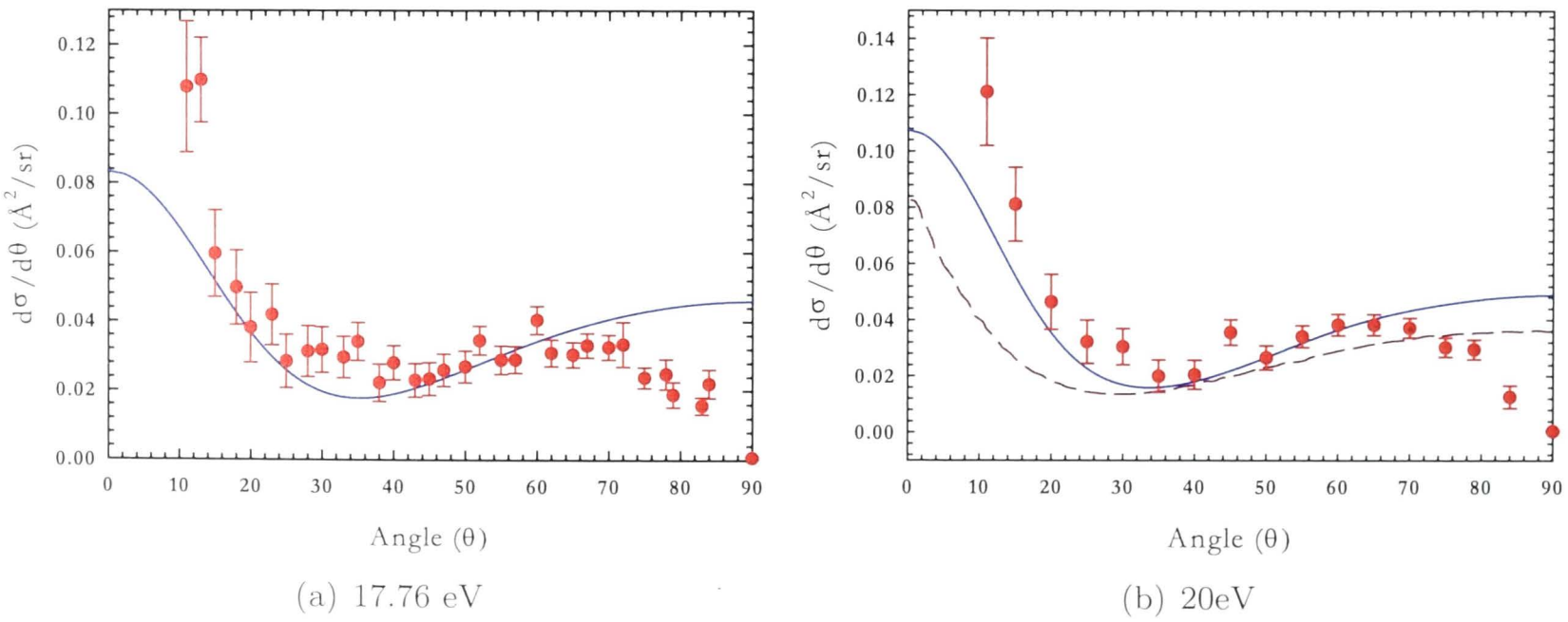

(a) 17.76 eV

(b) 20eV

Figure 5.4: Comparison of experimental and theoretical results for positron elastic differential scattering from He, (a) at 17.76 eV: solid circles, experimental results from Caradonna [70]; solid blue line, theoretical results of Utamuratov *et al.* [100] (CCC). (b) at 20 eV: solid circles, experimental results from Caradonna [70]; theoretical results of McEachran [103] (ROP); theoretical results of Utamuratov [106] (CCC).

Measurements Near Ionisation and Above

Above the Ore gap, but below the direct ionisation threshold, the only scattering channels open are the elastic, positronium formation and the (singlet) electronic excitations. In order to measure the elastic DCS, a magnetic field ratio between the SC and the RPA must be used to compress the parallel energy loss such that elastic scattering is separated from the electronic excitation, as discussed previously in Chapter 4. For the DCS results at 24 eV shown in figure 5.5 a field ratio of 1.5 was used. At 24 eV, the sum of the first two electronic excitations in He ($2\,^1S$ and $2\,^1P$) is 9 % of the grand total scattering cross section [87]. The DCS results are compared to ROP calculations [103] and show general agreement from 30 to 75 degrees, but again, the measured DCS tends to zero as the scattering angle approaches 90 degrees, indicative of multiple scattering.

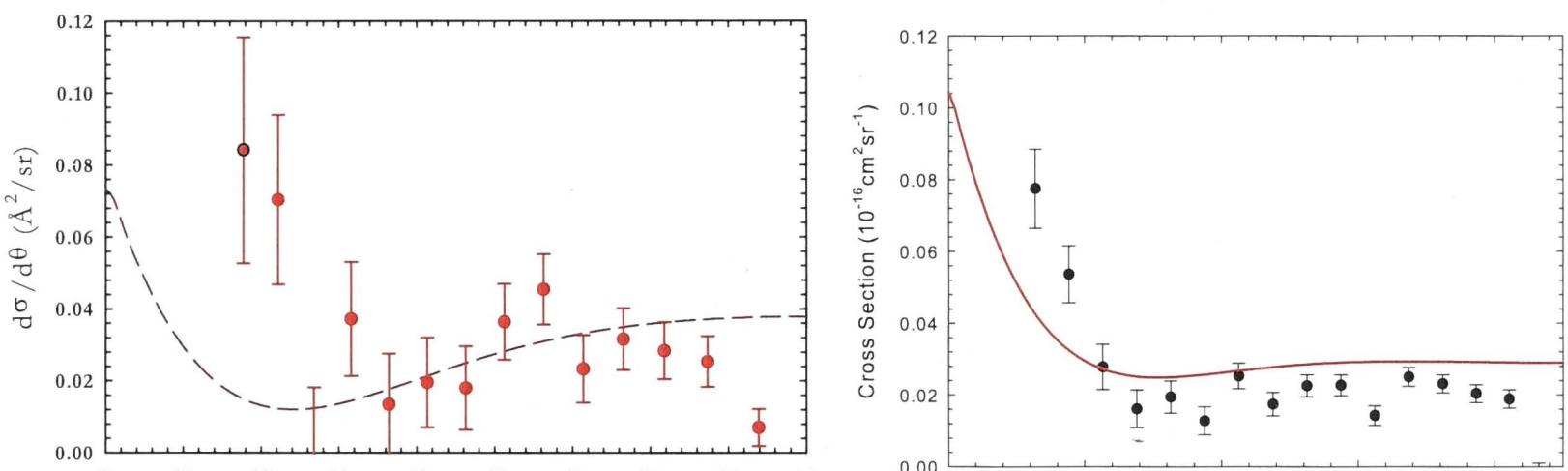

(a) 24 eV (b) 30 eV

Figure 5.5: (a) Comparison of experimental and theoretical results for positron elastic differential scattering from He at 24 eV: solid red circles, experimental results from Caradonna [70]; dashed magenta line, theoretical results of McEachran *et al.* [103] (ROP). (b) at 30 eV: solid black circles, current experimental results; solid red line, theoretical results of McEachran [103] (ROP).

For measurements at 30 eV, a magnetic field ratio of 5 was used and the resulting differential scattering cross section is presented in figure 5.5. General agreement is seen between the experiment and theory, but the experimental results are more forward peaked and show lower values at higher angles. The roll off at high angle is the smallest in angular extent of any of those considered so far which is likely due to the fact that the DCS is more forward peaked, along with the low scattering percentage of 3 %. At 30 eV the Ps formation cross section is half of the grand total scattering cross section and thus the strongest open partial channel. Therefore, it is reasonable to assume that the Ps formation channel could have an influence on the elastic scattering channel. Recent work by McEachran and Stauffer [10] has shown that the positronium formation channel has a marked effect on the forward scattering angles bringing their theoretical results into better agreement with the experimental results for Krypton and Xenon. Future theoretical work on the helium system will likely go at least part of the way towards rectifing the difference between the two results.

5.5 Discussion

While, there is some agreement between experiment and the various theoretical results in the overall shape of the differential cross section (DCS), discrepancies still exist. This is at least partly the result of multiple scattering due to the scattering percentage being too high. These effects are evident at a scattering probability as low as 3 %, but also depend on the angular dependence of the DCS. However, there are some energies where the experiment provides confirmation of new theoretical techniques in an energy region where calculation of the DCS is complicated by the positronium formation channel. It is clear that positronium formation strongly influences the elastic differential scattering cross section as evidenced by the large differences in the theoretical results, which do not include Ps formation, at 20 eV, seen in figure 5.4. Here the results of CCC, which have included Ps formation, more closely compare to the experimental results, despite the fact that the scattering percentage was too high, resulting in large discrepancies at high scattering angles.

Phase-shift Analysis

In principle the partial waves of a particular scattering event can be determined by fitting the analytical form of the elastic differential scattering cross section to the experimental data, and this is a goal of high-precision measurements of the elastic differential scattering cross section. This would allow projection to forward angles beyond the minimum angle discernible by the experimental apparatus, as well as providing an even more sensitive test of theory. One method involves fitting the experimental data using the partial-wave formalism, see Chapter 2, §2.5.1. This has previously been achieved for electron scattering from atoms [107,108]. The number of angular data points from the measurements discussed in this thesis are few, so only the first three terms, or partial waves, are considered,

$$\sigma_{dcs} \approx \frac{1}{k^2}\left(a_0|P_0(cos\theta)|^2 + a_1|P_1(cos\theta)|^2 + a_2|P_2(cos\theta)|^2\right). \tag{5.1}$$

A nonlinear fitting procedure was used in an attempt to determine the amplitudes of the first three partial waves in equation 5.1. Higher partial-waves (from $l = 4 \ldots 10$) were determined using an approximate form of the phase-shifts from Fraser [109]. The nonlinear technique was applied to the experimental results at a collision energy of 1.7 eV, figure 5.6, but was found to be unstable under small changes of the input parameters yielding wildly different results. Recent work by McEachran *et al.* [103] has shown that the first three partial waves can, in principle, be extracted from the experimental elastic differential scattering cross section by considering the folded nature of the cross section, and allows the method of least squares to be applied in determining the first three phase-shifts.

Partial-wave phase-shifts have been calculated by McEachran [103] and are plotted in figure 5.6 (a). A series of DCS measurements were taken at energies where the phase-shifts are markedly different and are plotted with the associated ROP calculation in figure 5.6 (b). The s- and p-wave phase shifts are changing significantly between the experimental

measurements, whereas the d- and f-wave phase shifts are nearly constant. While small differences in the measured DCS are observed, the experimental results are not sensitive to the differences displayed by the theoretical results. The variations in the experimental results are only just larger than the reported uncertainty and are unable to detect the change in the phase shift.

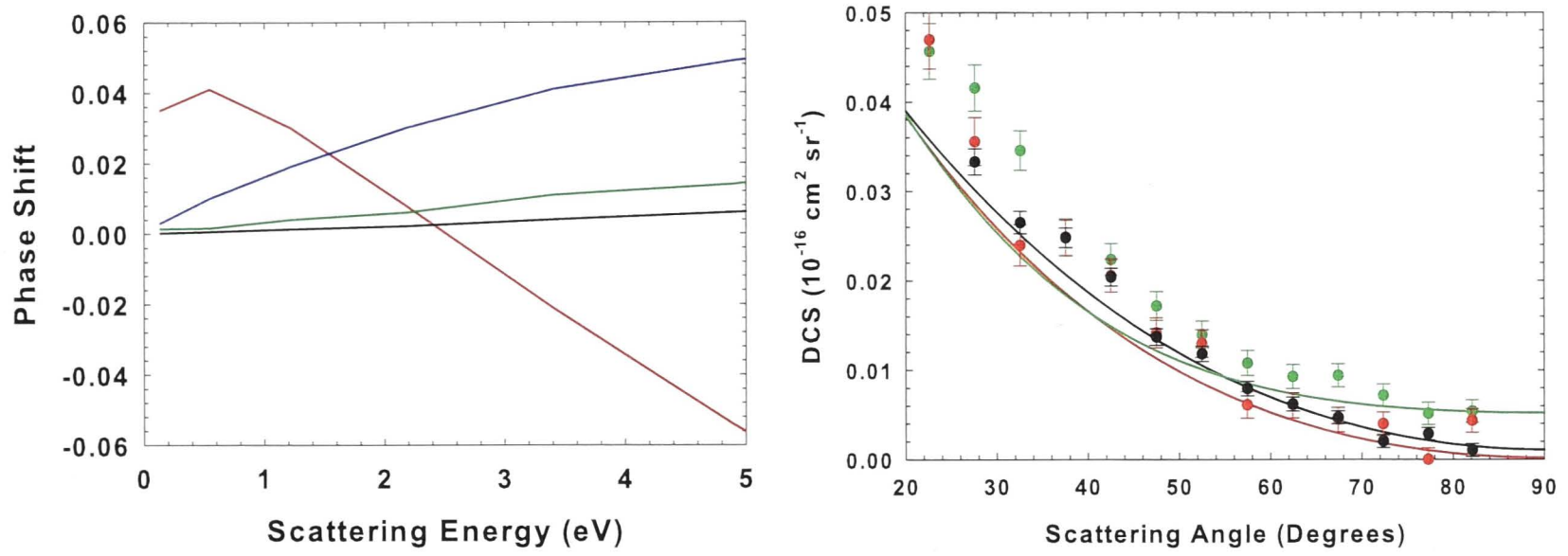

(a) Calculated phase shifts

(b) Various Collision Energies

Figure 5.6: Comparison of calculated phase shifts and measured elastic differential cross sections for positron-He scattering: (a) Phase shifts for l = 0,1,2,3 (red,blue,green,black) from McEachran [103] below 5 eV. (b) Comparison of current experimental (solid circles) DCS and theoretical DCS results for 1.7 eV (black), 2.5 eV (red), and 4 eV (green).

5.6 Conclusion

We have shown that state-of-the-art experimental and theoretical results for elastic differential scattering of positrons from helium are largely in agreement only when considering the systematic effects affecting the experimental data, particularly at low incident energies and at energies below the Ps formation threshold. Disagreements between experiment and theory above the Ps formation threshold reflect the difficulty of incorporating the description of this process accurately in theoretical calculations, as evidenced by the large difference between theoretical results, including and not including the Ps formation channel. The two-centre CCC calculations are in better agreement above the Ps formation threshold, whereas the ROP calculations, which do not consider Ps formation, are markedly different. Recently, addition of a model Ps formation channel to ROP calculations for Krypton and Xenon have shown the importance of incorporating this scattering channel in calculating the elastic differential scattering cross section.

The experimental differential scattering cross sections reported in this thesis are unable to explore the angular dependence to sufficiently low angle and with sufficiently small uncertainty to definitely distinguish between the various theoretical results, except for one instance above the Ps formation threshold at 15 eV. Overall the experimental results are in

the best agreement with the multi-centre CCC calculations both below and above the Ps threshold. Despite the general agreement these experimental results do no meet the goal of 'benchmarking' the elastic differential scattering cross section for the positron-helium system. The signature of multiple scattering is evident in all the experimental data to differing degrees even at a scattering percentage of 3 % within the scattering cell. Future measurements at lower scattering probabilities will be required to elucidate this issue, which will require longer acquisition time or higher positron flux.

Chapter 6

Search for Bound States in the Doubly Excited Helium System

This chapter reviews the search for resonance structure due to the existence of a positron bound state in the doubly excited helium system. Recent theoretical work has suggested that positrons should bind to a number of helium doubly excited states. This chapter reviews the theoretical background of positron binding to atoms and provides the results of our experimental search for associated resonant structure due to those bound states. Extension of this work to other systems is discussed.

6.1 Introduction

Recent calculations by Bromley *et al.* [14] have indicated that the $He(2s^2\ ^1S^e)$ doubly-excited state will bind a positron. The $e^+He(2s^2\ ^1S^e)$ state has a predicted binding energy of 0.447 eV with respect to the $He(2s^2\ ^1S^e)$ state. Binding of a positron to the He $2s^2$ state has been predicted to give rise to two resonances in positron scattering from ground state helium: $e^+He(2s^2\ ^1S^e)$ at 57.3716 eV and a $^2P^0$ shape resonance just above the $He(2s^2\ ^1S^e)$ threshold at 57.8485 eV. To search for these predicted resonances, low-energy positron scattering experiments were performed to measure the grand total scattering and positronium formation cross sections in the energy region about the double-excitation state thresholds.

Theoretical calculations have predicted that many different atoms are capable of binding a positron, to both the ground and electronically excited states of both atoms and molecules. For atomic systems, these states have binding energies ranging from 13 meV (e^+Na) to 0.50 eV (e^+Ca), but are unstable to positron-electron annihilation and therefore have short lifetimes [110]. Large Feshbach resonances have been observed in annihilation cross sections corresponding to the formation of positron-molecule bound states, providing strong evidence that such states also exist for molecules [111], but this has not been observed for positron-atom binding.

Previous studies of low-energy positron scattering from atoms have yielded no resonant structure due to the existance of positron-atom bound states [112, 113]. Early investigations have been performed with a relatively low resolution ($\Delta E \geq 0.5$ eV) and low intensity

positron beams, with the result that narrow or weak features in the cross sections were likely to be undetectable. In more recent years, the energy resolution available for positron scattering experiments has been improved significantly [74] but a high-resolution (ΔE $\sim$ 25 meV) investigation of H_2, N_2, CO and Ar [114] found no sign of predicted quasi-bound states, or resonances, in particular as predicted for H_2 in the total scattering cross section. Here the attachment was predicted to manifest itself as a Feshbach resonance. The search in Ar was limited to the excitation thresholds of the $3p^5$ ($^2P_{3/2}$) 4s (J=1) and $3p^5$ ($^2P_{1/2}$) 4s (J=1) states. No evidence was found for the existence of any resonances, and an upper limit on the resonance strength could be experimentally set at 6.3 $a_0^2 meV$ [114].

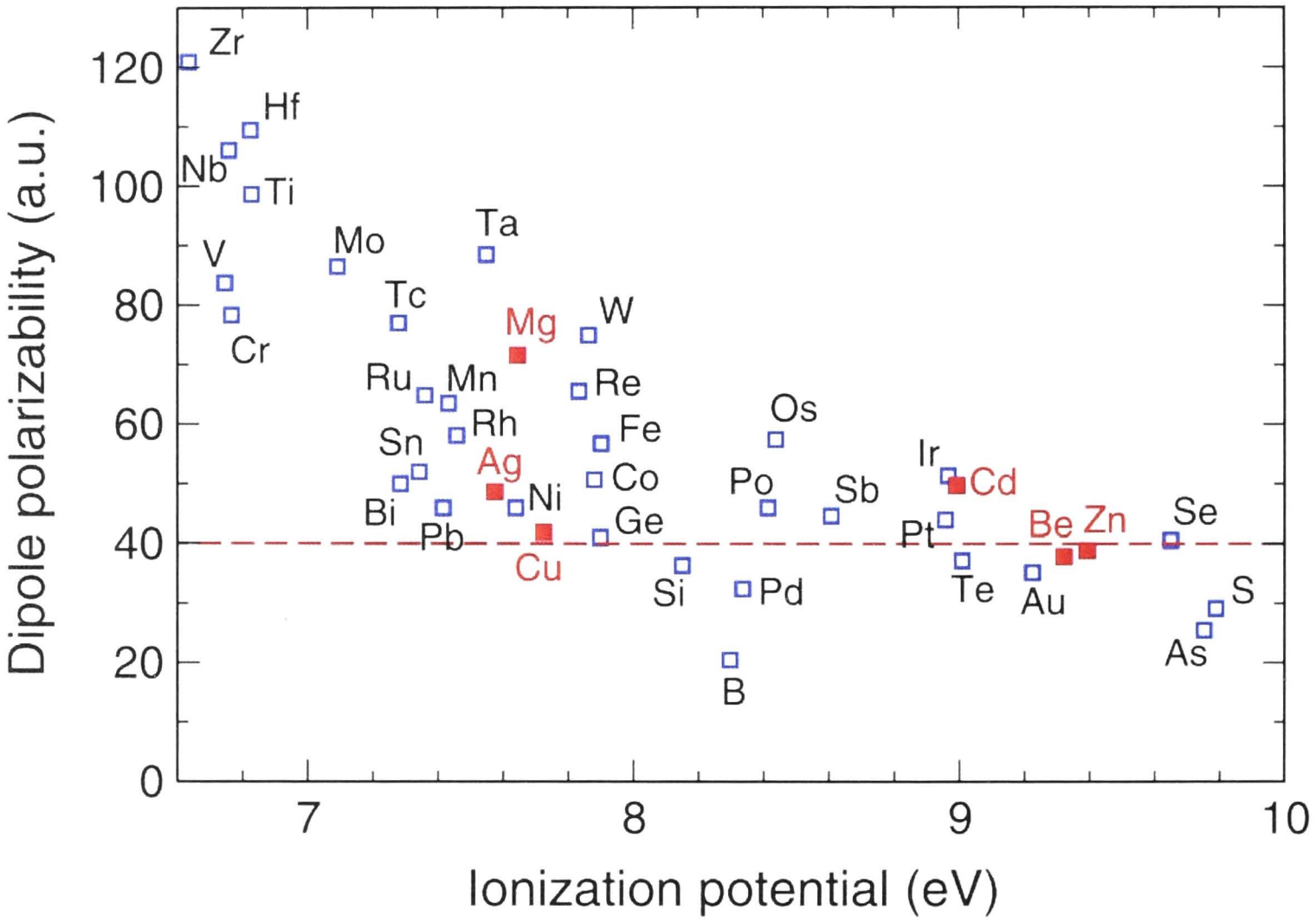

Figure 6.1: Dipole polarisability α_d versus ionisation potential for transition metals from Dzuba *et al.* [59]. The horizontal dashed line indicates the transition between binding (above) and nonbinding (below) atoms predicted at $\alpha_d = 40$ a.u..

Positron-atom bound states with higher binding energies are more suited to experimental study, but nearly all the atoms with high predicted binding energies are solids at room temperature. For example, some of the most promising candidates for the experimental search for positron-atom binding are open-shell transition metals (e.g. Fe, Co, Ni) due to their high dipole polarizabilities and moderate ionisation potentials [59, 110], see figure 6.1. Since single scattering positron experiments must use gaseous targets, atoms such as these transition metals provide an experimental challenge compared to the bulk of previous positron scattering studies. However, positron binding to excited states of gaseous targets provides a new area to be explored.

The current search was motivated by recent calculations performed for positron binding

to the helium doubly-excited states [14]. In their paper, Bromley *et al.* note the similarities in energetics of the doubly excited state(s) of helium to the ground state of the Mg ion, suggesting the likelihood that these state(s) can bind a positron. They also point out the similarity between the dipole polarisability (α_d) of the He $2s^2$ (76.2 a_o^3) and Mg $3s^2$ (71.3 a_o^3) states. Positron binding was found to be possible for model alkali atoms with dipole polarisabilites greater than 23.5 a_o^3 [110]. The current study explores the region about two of the predicted resonant positions; the bound state of e^+He ($2s^2\ ^1S^e$) and the ^2P_o shape resonance just above the He($2s^2\ ^1S^e$) state energy. We report on the measurement of total and positronium (Ps) formation cross sections in these regions.

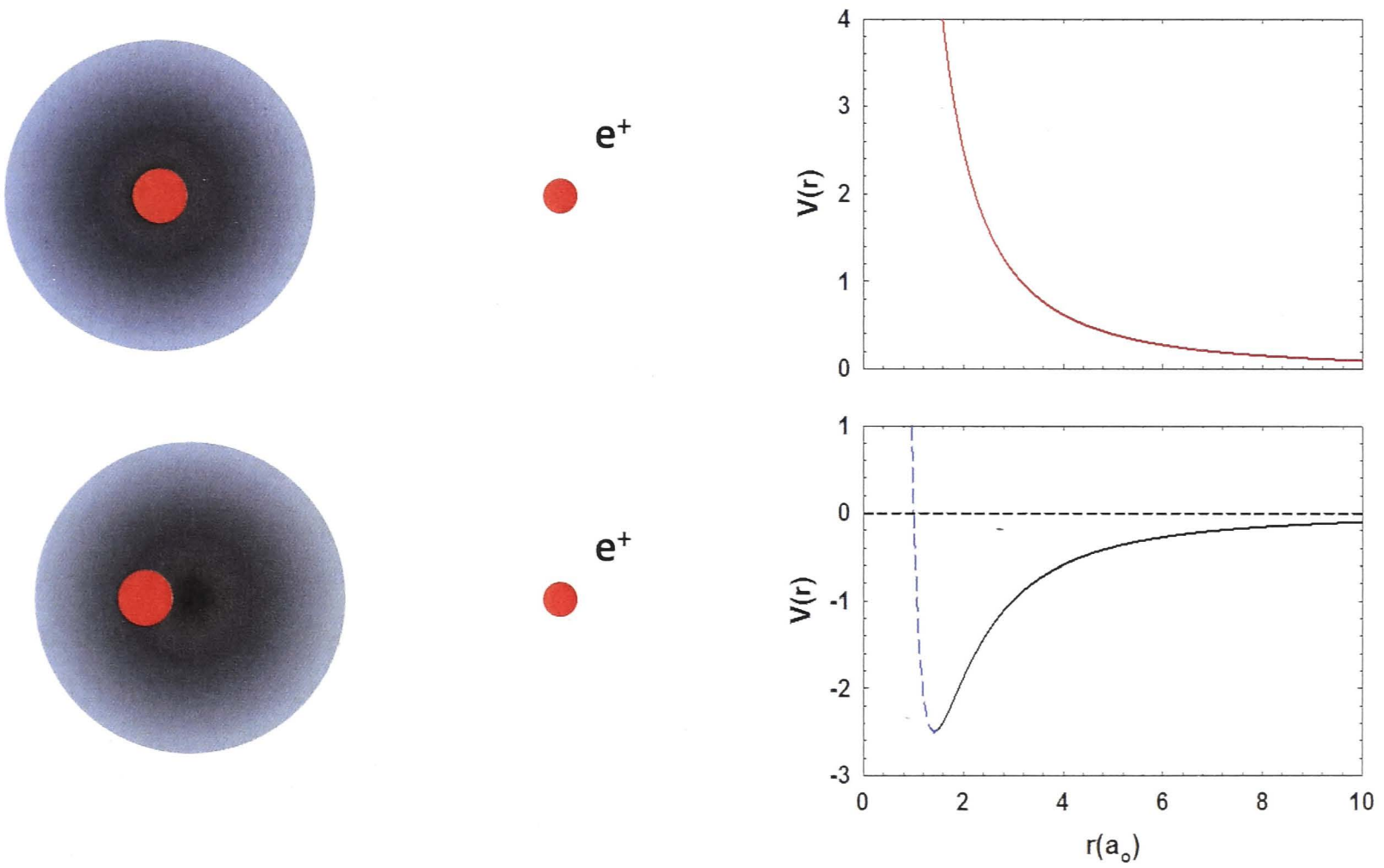

Figure 6.2: The static (top) and polarisation (bottom) potentials and their corresponding positron-atom configuration, adapted from [115].

6.2 Theoretical Description

At first glance it may seem counter intuitive that a positron can bind to a neutral atom and this is true for the static case. But if the positron is in motion or is moved closer to the atom, it can polarise the atom and it is this polarisation potential that is the mechanism for binding. For example, figure 6.2 shows both the static and polarisation potentials. In the static case the interaction is completely repulsive, but when the atom is polarised due to the presence of the positively charged positron, a minimum in the potential appears which potentially allows for binding. As the complexity or number of electronic configurations of the target increases, so too does the complexity of the calculations required to determine if a positron can bind to an atom. The general requirements for positron binding or the

formation of positronic atoms have been determined in terms of the physical parameters determined from the electronic configuration of the atom. A review of these requirements allows for the review of trends in positron binding to atoms.

Positron binding to a neutral atom has been described in two possible regimes and binding can be considered as a linear combination of the two possibilities. The wave function describing the bound state or positronic atom can be described heuristically [11, 54],

$$\Psi = a\Phi(atom)\phi(e^+) + b\Omega(atom^+)\omega(Ps), \tag{6.1}$$

where the two terms are used to describe the two possible configurations. The incident positron polarises the atom and binding can occur via the polarisation potential and the unitary charge of the positron. This is similar to the mechanism for the binding of an electron to form a negative ion [35] where the electron displaces the electron cloud to 'see' the positively charged core, thus providing an attractive potential for binding. Alternatively, the positron can ionise the atom in the process of forming positronium and the resultant positronium and the residual ion can bind via a similar minimum in the polarisation potential. Each of these types of binding are highly target dependent, but the general criterion for binding can be described in terms of the atomic ionisation potential (IP) and the positronium binding energy of 6.8 eV (or 0.250 Hartrees).

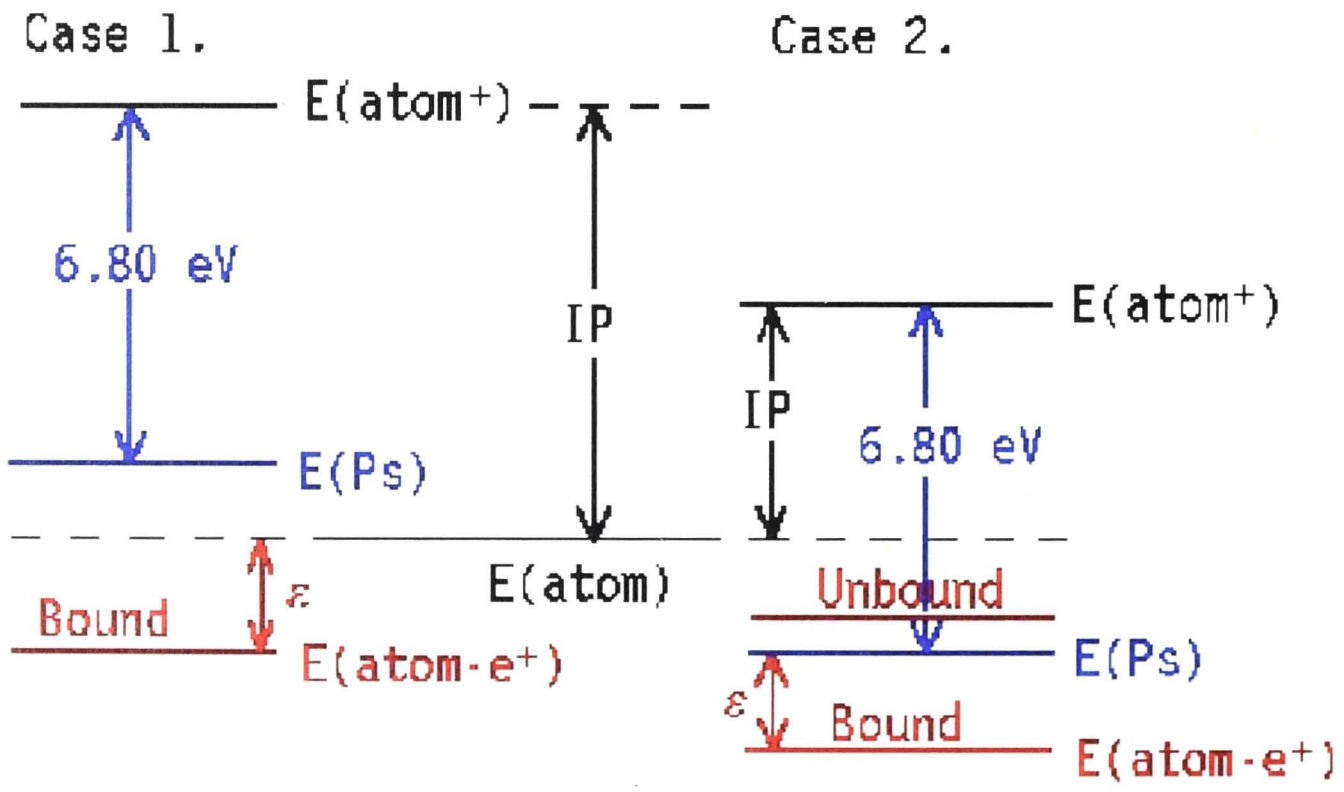

Figure 6.3: Schematic energy levels for the two binding cases from [115], see text for further details.

A schematic energy level diagram of each case is shown in figure 6.3. Case 1 is the configuration in which the ionistaion potential is larger than the Ps binding energy and a positron will bind to the atom temporarily if the binding energy is below the ground state energy of the atom. Case 2 is the configuration in which the ionisation potential is smaller than the Ps binding energy and a Ps cluster binds to the residual atomic ion if the bound

state energy is lower than the difference between the IP and 6.80 eV. There exists a third case in which the atomic target is excited, replacing the ground state atom in cases 1 and 2, such that the binding is determined with reference to the excited state energy [116]. These states provide a manifold of possible bound states, but if we constrain ourselves to the case of the two electron atom, helium, the first possibility is the lowest doubly excited state or $He(2s^2)$.

Figure 6.4 from Bromley *et al.* [14] is an energy-level diagram comparing the doubly excited states of helium to the helium negative ion states, and those of the calculated positron bound states. As can be seen from the energy level diagram, the positronic complexes are lower in energy than the corresponding neutral excited state energy thus indicating that the states are bound. Considering the description above, note that the bound states are lower than the energy of formation of positronium from the excited helium atom or put another way, the formation of Ps from the excited helium ion (He^+ 2s ion). Thus any atomic target which has excited states which exist more than 6.80 eV below the excited ionic threshold could support binding. As these positron bound states are similar to negative ion states, the observation of negative ion resonances with the appropriate configuration for positron binding would strongly imply the possibility that the system supports positron binding. The similarity to negative ion resonances also suggests the size of corresponding negative ion resonances should provide a guide for the expected size of the resonance feature in positron scattering.

A variety of excited states have been investigated theoretically which support a positron-atom bound state. Positron binding to excited states has been predicted for He, Li, Cd, Be [13,14,116]. A subset of these states are shown in figure 6.5, from Bromley *et al.* [116], including the model alkali ground state atom which is the comparison generally made to specific target ground states and/or excited states. Figure 6.5 shows the theoretical positron-atom binding energies versus the parent atomic ionisation energy [110]. The solid circles were determined using SVM, the solid diamonds were determined using CI_{pol}-bases, and the solid triangles are results of other calculations. The dashed line is a model $^1S^e$ e^+-alkali atom system [11].

6.3 Search for Bound States

The search for resonant structure requires the resonant strength to be quantified in some manner. This is convenient for setting detection limits on calculated or postulated resonance structure. Energy resolution and statistical uncertainties limit the sensitivity of these measurements to resonances in the cross sections. The upper bound on the resonance strength can be estimated (95 % confidence level) [34] by

$$\sigma_r \Delta E_r < 2\sigma_{rms} \Delta E_b, \tag{6.2}$$

where E_r is the energy width (FWHM) of the resonance, σ_r is the magnitude of the resonant cross section, E_b is the energy width (FWHM) of the positron beam, and σ_{rms} is

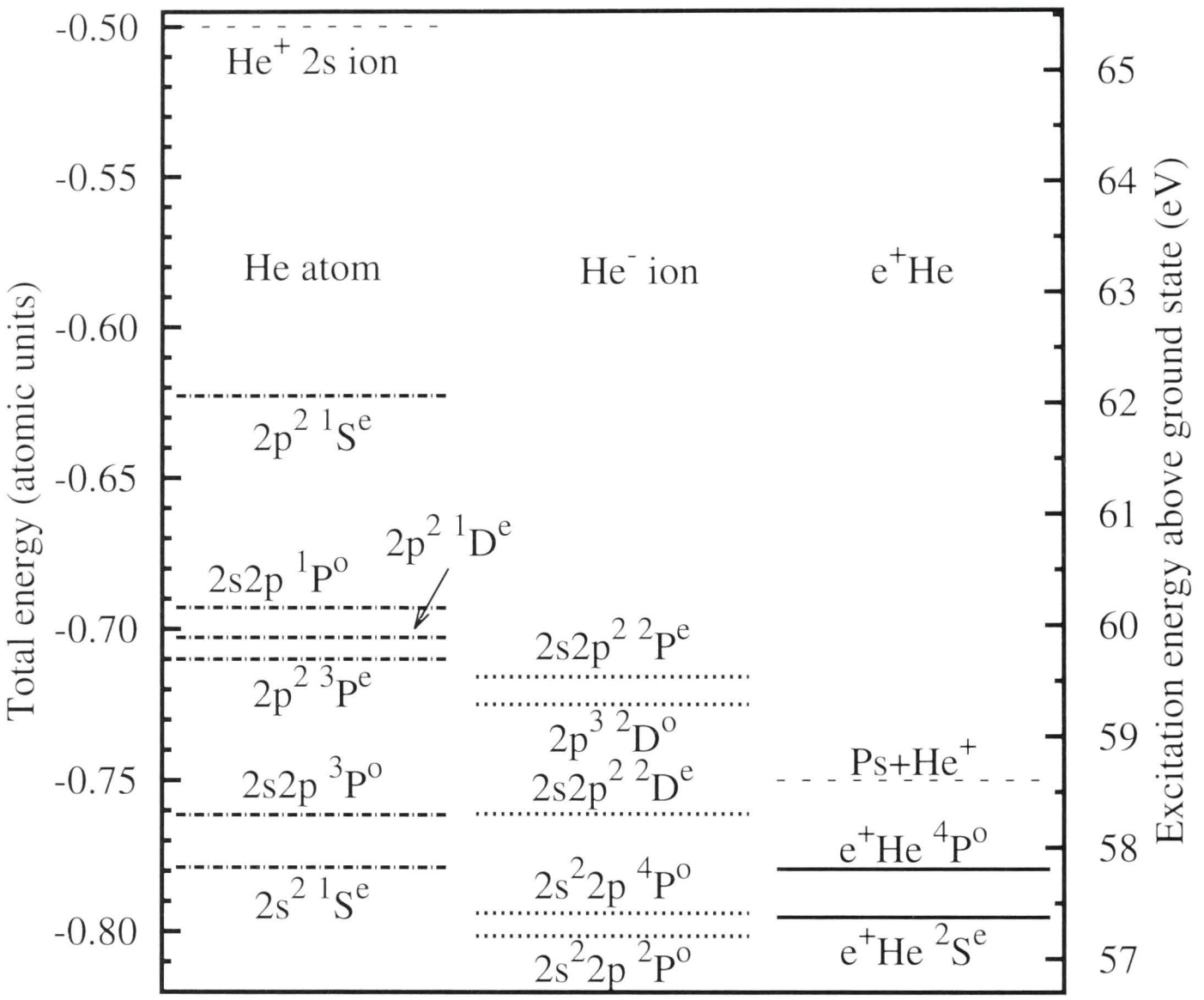

Figure 6.4: Energy level diagram from Bromley *et al.* [14] showing the doubly excited states of helium and the states with an attached positron. Comparison is also made to the states of the helium negative ion.

the statistical uncertainty (one standard deviation) of the cross section data. This assumes that the resonance structure is Gaussian or a symmetric peak in the cross section.

Measurements were made of the grand total and positronium cross sections at energies around the two predicted resonance positions: 57.3716 eV (for $e^+He(2s^2\ ^1S_e)$) and just above the $He(2s^2\ ^1S^e)$ threshold of 57.8485 eV (for the $^2P^\circ$ shape resonance) [14]. The energy step size in the measurement was 20 meV and the parallel energy width was 60 meV. Figures 6.6 and 6.7 show the present results for both energy regions. The statistical uncertainties in figure 6.6 range from 0.7 % (grand total) to 3.1 % (Ps), and in figure 6.7 from 1.3 % (grand total) to 6.4 % (Ps). No resonant features are observed in these cross sections with this energy resolution and these statistical uncertainties.

Using equation 6.2 it is possible to place an upper bound on the resonance strength at each of these energies. For the predicted $e^+He(2s^2\ ^1S^e)$ resonance the upper bound is 1.14 $Å^2$meV for the grand total and 1.12 $Å^2$meV for the Ps cross section. For the predicted $^2P^\circ$ shape resonance this is 2.06 $Å^2$meV for the grand total and 2.08 $Å^2$meV for the Ps cross section. These upper bounds are summarised in table 6.1.

Based on previous measurements of electron resonances in this energy region, Bromley *et al.* [14] compared positron attachment to the case of electron attachment, suggesting

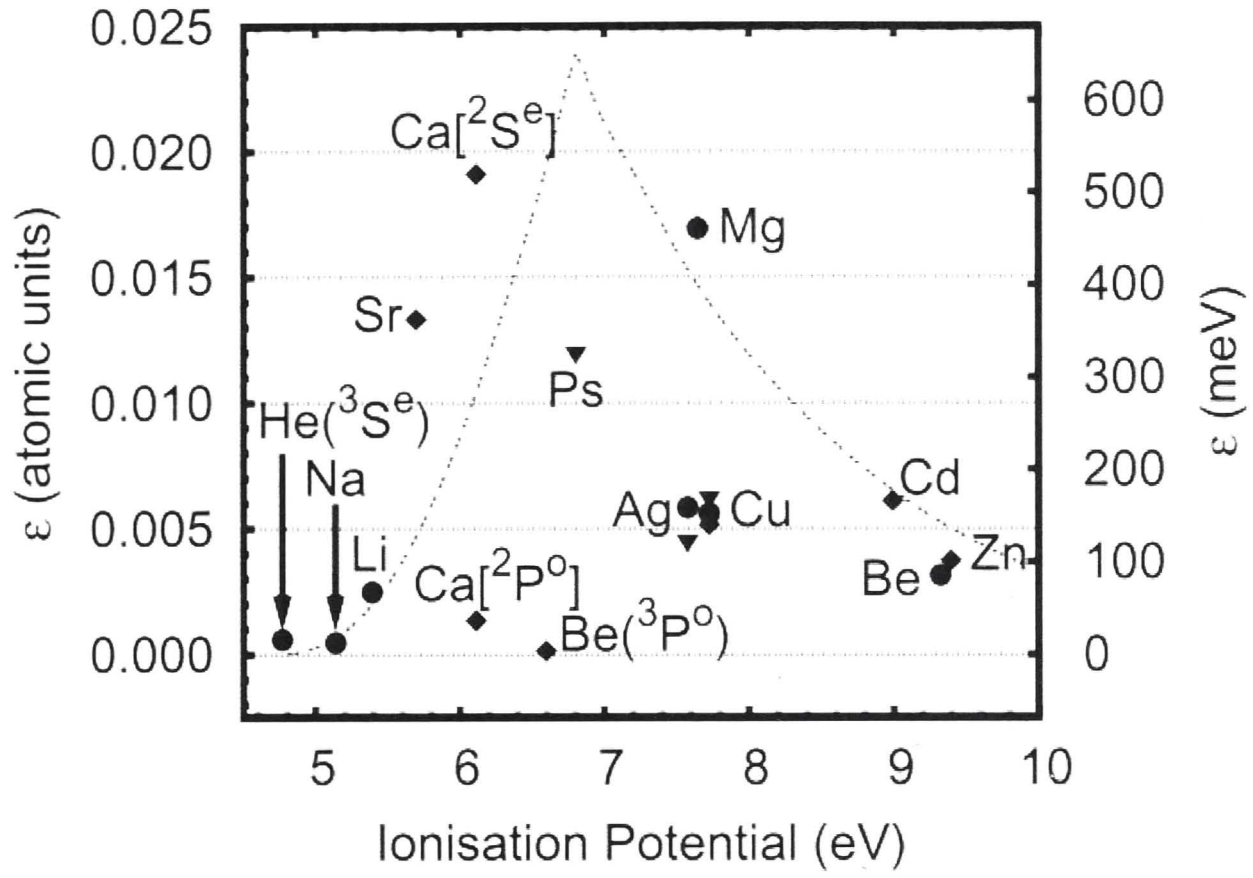

Figure 6.5: Comparison of excited states, supporting binding to ground states which, have been shown to support binding from Bromley *et al.* [116]. The solid black circles were computed with the SVM, the solid black diamond are CI_{pol}-based, the solid black triangles are other calculations. The total $^{2S+1}L^{\pi}$ symmetries are implicit: the one-e$^-$ atoms are $^1S^e$, the two-e$^-$ atoms are of $^2S^e$. The (...) indicate the excited parent state symmetry, the [...] are the overall symmetry. The line is a model $^1S^e$ e$^+$-alkali atom system [116] and references therein.

Table 6.1: Summary of Resonance Searches

Energy Range (eV)	Cross Section	Upper Bound on Resonance Strength (Å^{2}meV)
57.23 - 57.63	Grand Total	1.14
	Ps	1.12
57.62 - 58.16	Grand Total	2.06
	Ps	2.08

these positron bound states are detectable. Using available experimental and theoretical results we calculated the expected resonance strength. The magnitude of the observed electron resonance in the ion yield for the He($2s^2$ $^1S^e$) state was determined to be 0.8 % of the total ion current by Quéméner *et al.* [117]. Using the results of Fromme *et al.* [112], for ionisation of helium by positron impact, who predict the magnitude of the ionisation cross section in this energy region to be 0.38 Å^2, we can determine an approximate resonance strength of 0.21 Å^{2}meV using equation 6.2. This resonance strength is more than 5 times smaller than our upper limit for measurements of the total and positronium formation cross sections about the He($2s^2$ $^1S^e$) state energy.

The similarity of the temporary negative ions to temporary positron bound states, in the lowest doubly excited states of helium, begs the question of whether or not the higher-lying doubly-excited states can support such bound states. In principle, similar

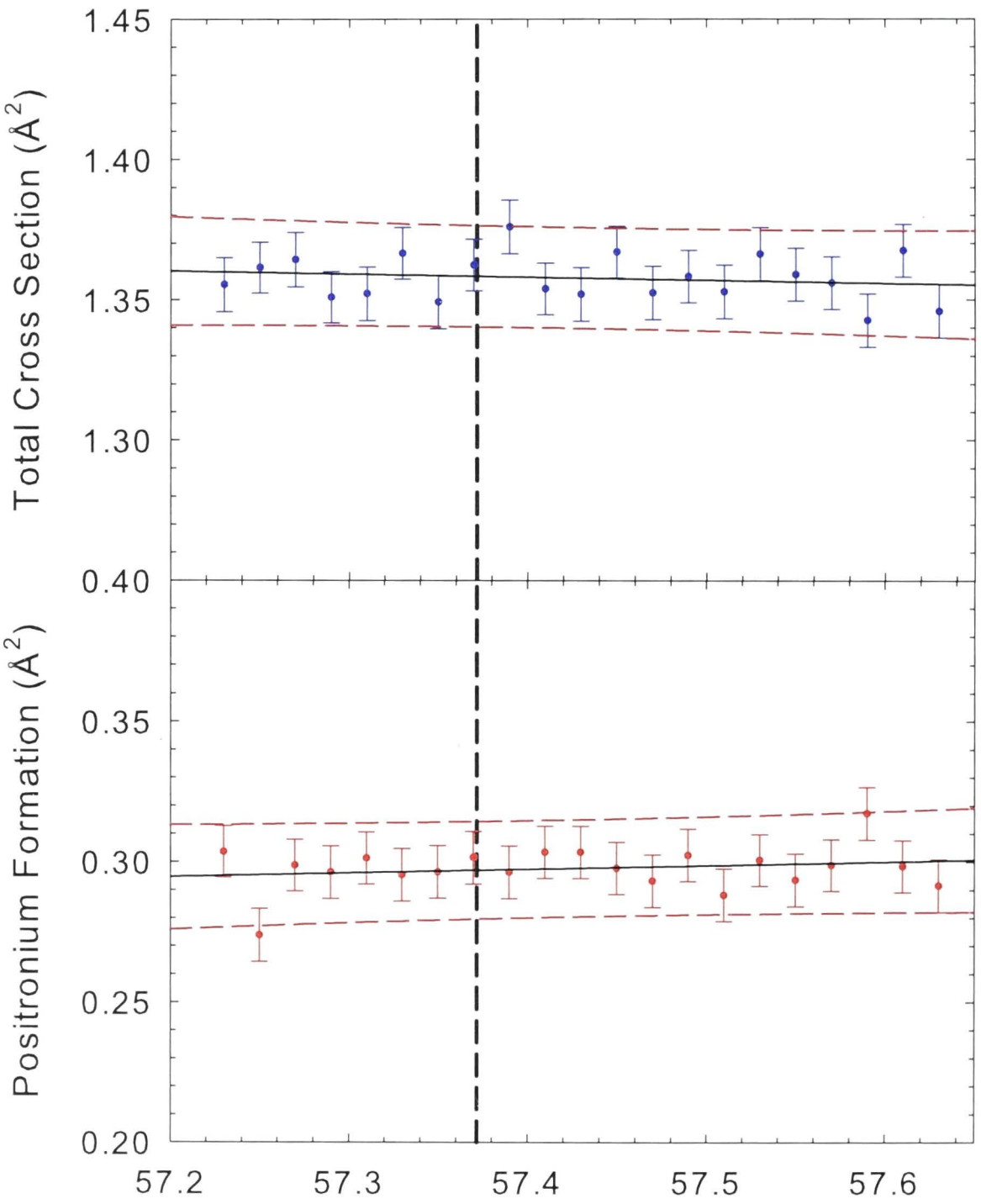

Figure 6.6: Cross sections: top panel, grand total scattering; bottom panel, positronium formation (Ps). The theoretically predicted location of the $e^+He(2s^2\ ^1S_e)$ state is indicated with a vertical dashed line at 57.3716 eV. The red dashed lines are the 95 % confidence intervals and the solid lines are linear fits through the data.

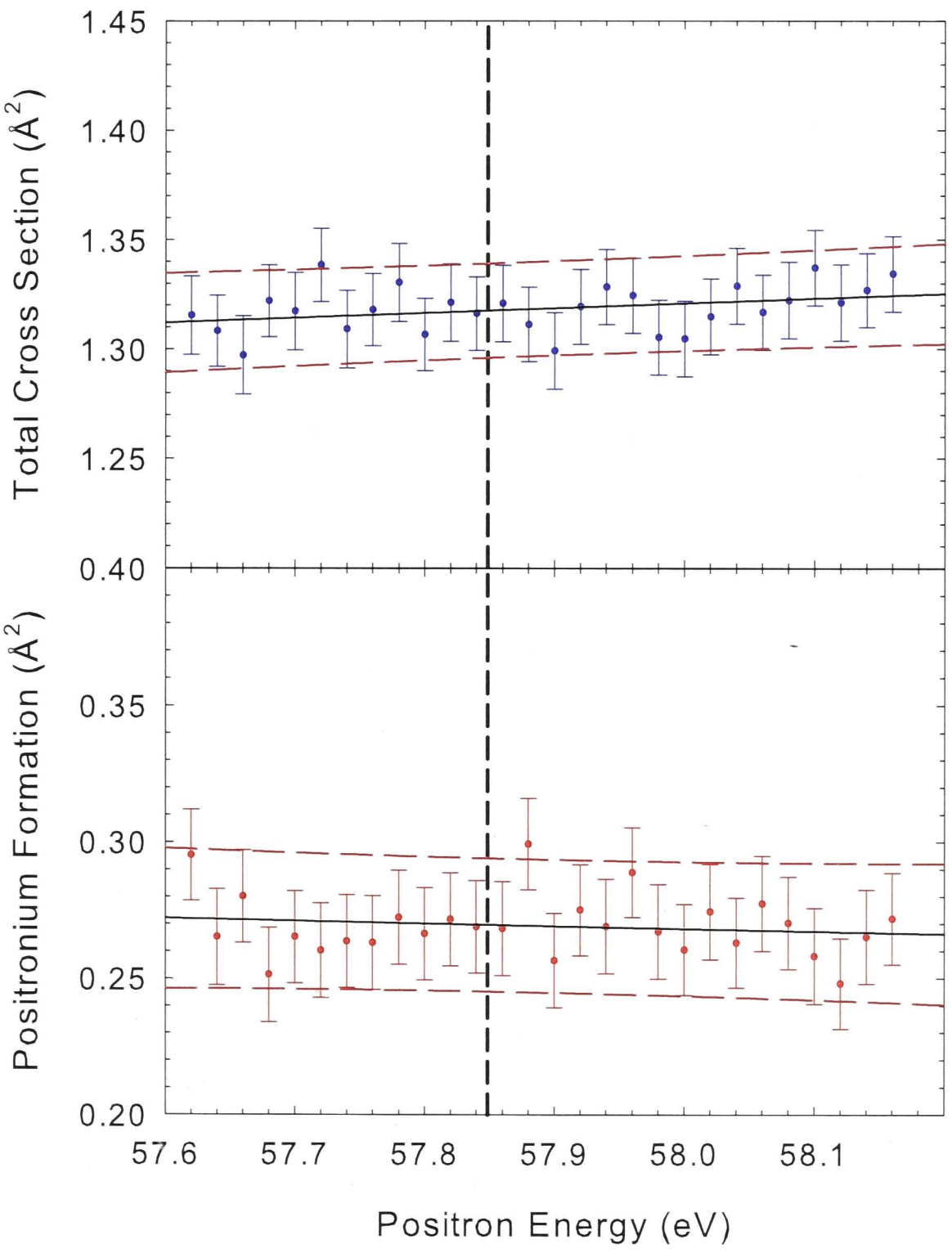

Figure 6.7: Cross sections: top panel, grand total scattering;bottom panel, positronium formation (Ps). The predicted theoretical location of the He($2s^2\ ^1S_e$) state at 57.8485 eV is indicated with a vertical dashed line. The red dashed lines are the 95 % confidence intervals and the solid lines are linear fits through the data.

configurations occur in all the noble gases and negative ion resonances are observed, thus temporary binding of positrons to doubly-excited state in the series of noble gases should exist. However, the strength of negative ion resonance features as a percentage of the grand total scattering cross section decreases as the excited state energy approaches the ionisation limit. Therefore, these potential temporary bound states are likely to result in resonances which are even smaller in magnitude than for the lowest excited state, pushing them farther away from the detection limit of this type of experimental search.

6.4 Conclusion

In conclusion, measurements of the grand total and positronium formation cross sections for He have been made in two different energy regions to search for resonances associated with the He $2s^2$ state. Whilst no clear resonances were observed, upper bounds have been placed on the strength of these resonances ranging from 1.12 to 2.08 $Å^2$meV. This suggests that these resonances are either too narrow or too weak to detect with the current experimental arrangement and technique. It is possible that these resonances would be more pronounced in a different partial cross section (e.g. annihilation, direct ionisation, or electronic excitation) warranting further study in the future as experimental techniques improve.

The addition of excited state binding of positrons to atoms adds another series of possible targets in which verification of our theoretical understanding can be tested. These targets are much more readily accessible experimentally due to the target atoms being gaseous at room temperature, but the magnitude of the resonances associated with binding is still in question. As has been seen with this study, and the implication from the similarities with resonances related to temporary negative ion states, these resonance structures are most likely fractions of a percent of the grand total scattering cross section. As experiments are only now becoming possible with uncertainties down to single-digit percentages, only upper limits will likely be set until another means of detection is undertaken, such as the measurement of the annihilation rate as a function of the incident energy as is the case of measurements for positron interaction with molecules [118].

Chapter 7

Positron Scattering from Molecular Hydrogen

This chapter presents experimental total and partial cross sections for positron scattering from H_2. The total scattering and positronium formation cross sections are reported between 0.5 and 200 eV. Total elastic and inelastic scattering cross sections are reported for energies between the positronium formation threshold and 50 eV. The elastic differential scattering cross sections are reported at 1, 3, 5, 7 and 10 eV. Previous results, both experimental and theoretical, are compared to these results, with particular attention paid to the region below the positronium formation threshold. Systematic effects in both the present and previous results are discussed in the context of the observed discrepancies in experimental results.

7.1 Introduction

Molecular hydrogen is the simplest neutral molecule and it has been extensively studied in a range of lepton collisions, but the results for positron scattering from H_2 are still incomplete in comparison to the electron. An example of this is the lack of scattering information for rotational excitation, and only limited data for vibrational [119] and electronic excitation [34] processes. This is largely due to the historically limited availability of high resolution positron beams, with the concomitant difficulty in resolving discrete partial cross sections.

It has been 40 years since Coleman *et al.* and Hoffman *et al.* [120, 121] published the first low-energy total cross sections for positron-H_2 scattering. Since then, there have been a number of experimental and theoretical results. At energies above the positronium formation threshold there is general agreement in both the magnitude and energy dependence of the total cross section on the experimental side within the stated uncertainty, if not for the limited number of theoretical calculations available. Below the positronium threshold, this is not the case. In this energy region there are a broad range of reported results, both experimental and theoretical, which are in apparent disagreement with each other, with the recent results of the Trento group [122] noticeably higher than any other calculation or measurement.

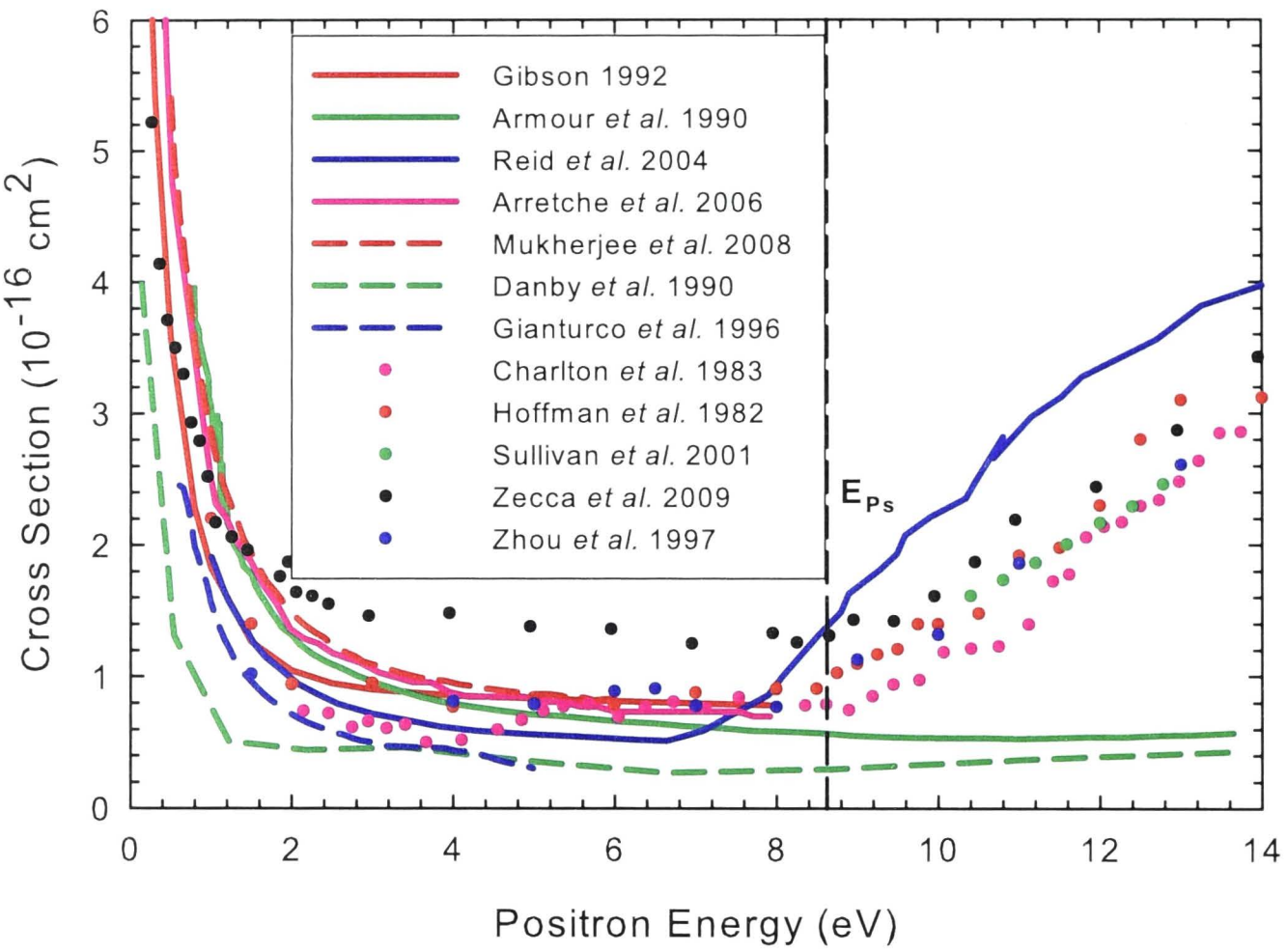

Figure 7.1: A comparison of the available experimental and theoretical results preceding the current results for the grand total scattering cross section (σ_{GTCS}) of positrons from molecular hydrogen (H_2). Experimental data: black points, Zecca *et al.* [122]; red points, Hoffman *et al.* [121]; magenta points, Charlton *et al.* [123]; green points, Sullivan *et al.* [114]; blue points, Zhou *et al.* [124], theoretical data: solid red line, Gibson *et al.* [125]; solid green line, Armour *et al.* [126]; solid blue line, Reid *et al.* [15]; solid magenta line, Arretche *et al.* [17]; dashed red line, Mukherjee *et al.* [127]; dashed green line, Danby *et al.* [18], dashed blue line, Gianturco *et al.* [128]. The vertical dashed line indicates the threshold energy for the formation of positronium at 8.643 eV.

Figure 7.1 shows the state of theoretical and experimental results for the total scattering cross section for positron-H_2 scattering before the present measurements were made, including a range of theory and experiment [15,17,18,114,123–128]. It does not incorporate our present measurements or the very recent Convergent-Closed-Coupling (CCC) theory of Zammit *et al.* [16]. The observed discrepancies in this figure, between both theory and experiment, were a significant motivation for the current study. A notable point, in the case of the previous experimental data, is that each experiment has differing angular acceptance of scattered positrons, with the Trento apparatus having the best discrimination against forward scattered positrons of those experiments presented in figure 7.1. This is the likely source of much of the observed discrepancy, as explained in a previous Chapter 4.

When a positron with incident energy in the range of 0-200 eV collides with a H_2 molecule a number of processes may occur. In the present series of experiments, we have focused on measurements of the grand total, total positronium formation and total inelastic scattering cross sections. As explained in Chapter 4 the experiment was unable to

discriminate between elastic scattering and vibrational or rotational excitation. However, the quasi-elastic (i.e. summed over vibrational and rotational excitation) total and angular differential positron scattering cross section was measured up to 50 eV. These results provide absolute scattering cross sections which can be used in models of positron transport, or in detailed comparisons with state-of-the-art quantum scattering calculations.

7.2 Results

7.2.1 Grand Total Scattering Cross Section

The total scattering results below 10 eV are shown in figure 7.2. The figure compares the current experimental results with selected previous work, including the experimental data of the Trento Group [122], the theoretical results of Reid *et al.* [15], along with the most recent results of Zhang *et al.* [63], Tenfen *et al.* [129] and Zammit *et al.* [16]. The total cross section with estimated corrections for the missing angular range is shown using the calculations of Reid *et al.* [15] as discussed in Chapter 4. The results appear larger in magnitude than all previous work, even that of the Trento group, which was far larger in magnitude than all previous experimental data (see figure 7.1). The experimental results in figure 7.1 have far worse angular resolution, for instance Hoffman *et al.* [121] reported a minimum angle of 25 degrees at 5 eV, Charlton *et al.* [123] reported minimum angle of 20 degrees and Zhou *et al.* [124] reported a minimum angle of 24 degrees at 20 eV. The angular resolution for the present measurements was considerably better than all previous experimental work (see table 7.1), and this likely accounts for most of the apparent differences in the results. The comparison with the Trento data shown in the figure is also consistent with comparisons of recent measurements [92, 130, 131].

In this energy range, the experimental data lies higher in magnitude than all the theoretical calculations shown in figure 7.2, as well as the other theories shown in figure 7.1. The reasons for this are less clear, as the calculations have none of the angular resolution difficulties that are seen in the case of experiment and thus should be higher than the reported experimental values. For the most part the theories represent the relative shape of the cross section reasonably well, while underestimating the magnitude. In the case of Reid *et al.*, an increase in the cross section at energies above 7 eV is due to the method used to incorporate the positronium formation channel. Here the Ps channel was considered to be an inelastic scattering channel, such as ionisation or electronic excitation, with a threshold energy of the average of the the Ps threshold and dissociation. One obvious consideration in the comparison with theory is that the calculations do not take into account vibrational and rotational excitation, with all calculations being performed with a fixed internuclear distance of 1.4 a_o. The effect of the internuclear separation will be discussed in 7.3. Both vibrational and rotational excitation are included in the experimental data and it may be that including these processes in theoretical calculations will improve the agreement. However, given the magnitude of the vibrational excitation measured by Sullivan *et al.* [119], and reasonable estimates of the rotational excitation, it

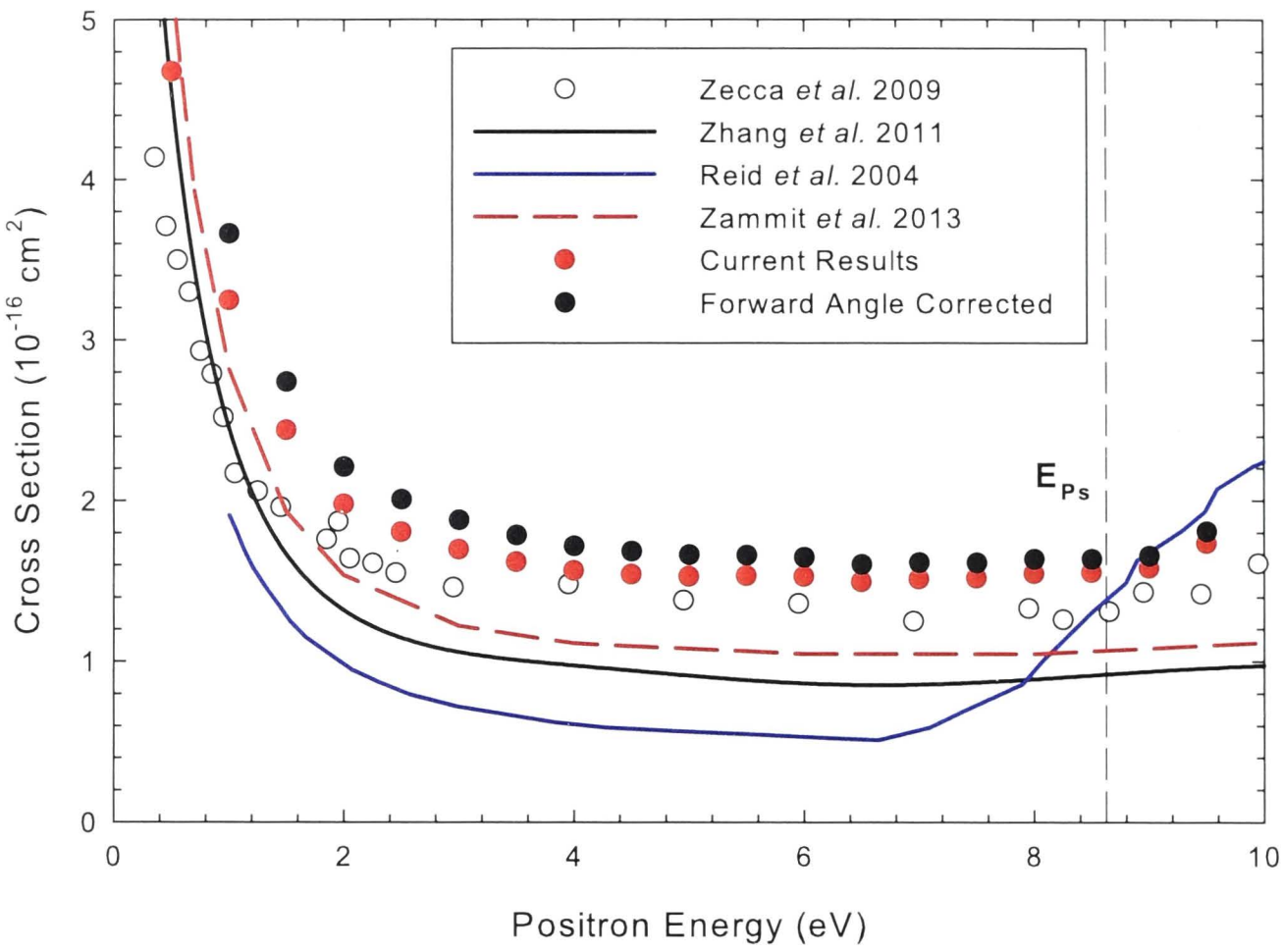

Figure 7.2: Experimental and theoretical results for the total cross section below the ionization threshold. Experimental results: solid red circles, current results; solid black circles, angular correction applied, see text; open circles, Trento results [122]. Theoretical results: solid blue line, Reid *et al.* [15]; solid black line, Zhang *et al.* [63]; and dashed red line, Zammit *et al.* [16].

is unlikely that this can account for all of the difference between experiment and theory in this case.

The comparison of the current results with previous work up to energies of 200 eV is shown in figure 7.3. At energies above the positronium formation threshold, the various experimental results converge, with no difference within the stated errors of the measurements. This is consistent with previous observations that differences in angular resolution become less important as the scattering energy increases. The peak of the total cross section around 25 eV corresponds to the maximum of the positronium formation cross section (7.2.2). The comparison between experiment and theory is also very good in this energy range, with the calculations lying perhaps a little lower than the measurements at

Table 7.1: Missing forward angles for this experimental work estimated using the theoretical results of Reid *et al.* [15], see text for discussion.

E (eV)	θ_C (^{o})	% Missing
1	23	16
3	13	12
5	10	9
7	8	6

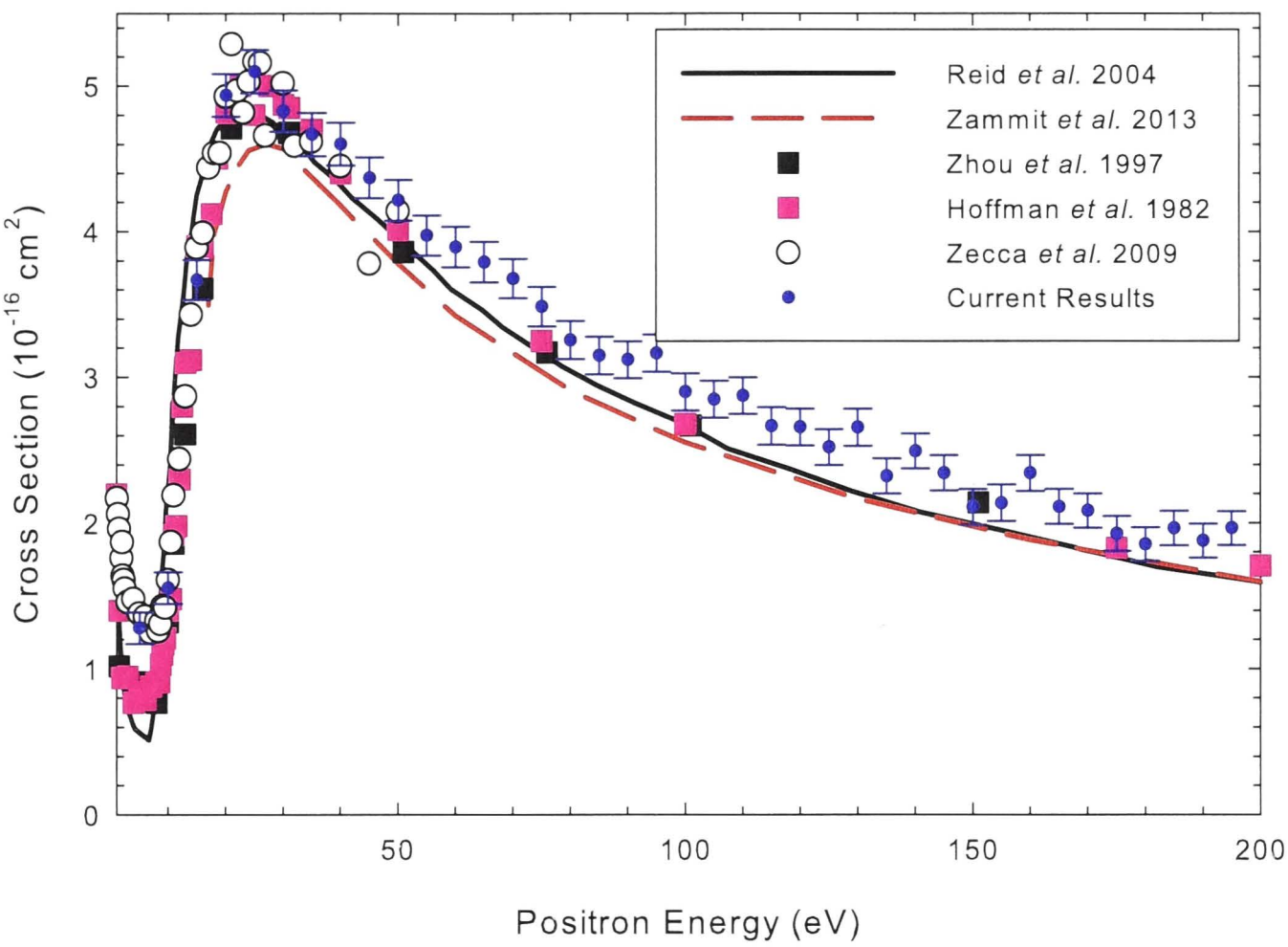

Figure 7.3: Comparison of results for the Grand Total Cross Section (GTCS) up to 200 eV. Experimental result: filled blue circles; current results open black circles; Zecca *et al.* [122], filled magenta squares; Hoffman *et al.* [121], filled black squares; Zhou *et al.* [124]. Theoretical results; solid black line, results from Reid *et al.* [15]; dashed red line, results from Zammit *et al.* [16]

energies above 50 eV. The underestimation of the most recent theoretical results of Zammit *et al.* [16] below 30 eV will likely be resolved as understanding of how the positronium formation channel couples to the elastic scattering channel, and in particular the role of virtual positronium states, is improved.

7.2.2 Positronium Formation

The positronium formation cross section is shown in figure 7.4, where we see a reasonable agreement between the present results and those of previous investigators [124, 132, 133]. The results show the positronium formation cross section is a smoothly varying function over the range of investigation which is typical of the energy dependence seen in previous measurements of other diatomic molecular targets [42]. It rises to a peak at $\sim$ 25 eV and then falls away as the ionization channel opens, falling to essentially zero by 150 eV. Theoretical results for the positronium formation cross section are included in figure 7.4. We see general agreement with a coupled-state calculation of Biswas *et al.* [135] at energies below 80 eV. Above 50 eV, a simplified second-order perturbative Born series was used by Biswas *et al.* [134], but theory and experiment do not converge until approximately 70 eV. Unfortunately, few theoretical results are available for the positronium formation

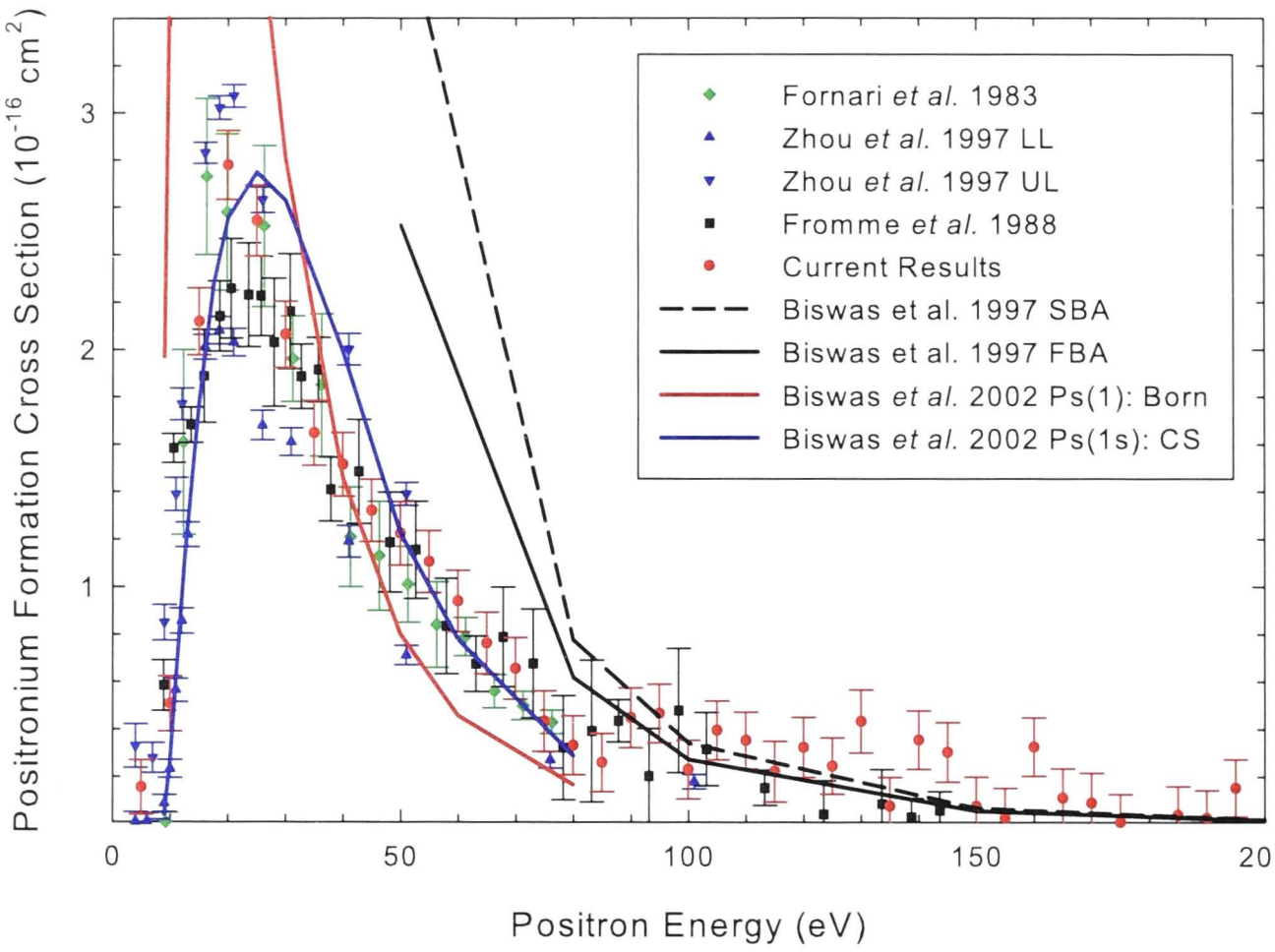

Figure 7.4: Comparison of the Positronium (Ps) formation cross section up to 200 eV. Experimental results: filled red circles; current, filled magenta circles; Fromme *et al.* 1988 [132], filled blue down-triangle; upper limit Zhou *et al.* 1997 [124], filled blue up-triangle; lower limit Zhou *et al.* [124], filled green circle, Fornari *et al.* 1983 [133]. Theoretical results from Biswas *et al.* [134]: dashed black line; second-order Born approximation (SBA), solid black line; first-order Born approximation (FBA) and theoretical results from Biswas *et al.* [135]: solid red line; Ps(1) Born, solid blue line; Ps(1s) CS calculations.

channel due to the difficulty in treating the multi-centre nature of the scattering problem, as discussed in Chapter 2, requiring more extensive theoretical investigation.

7.2.3 Elastic Differential Cross Section

The quasi-elastic (summed over rotations and vibrations) differential cross section (DCS) was measured at energies of 1, 3, 7 and 10 eV. We also note here that there has been one previous measurement of the elastic differential cross section for positron scattering from molecular hydrogen by Sullivan *et al.* [38], although this was at 0.5 eV, and thus below the range of energies considered in this work. Figure 7.5 compares the current experimental results with those from available theory [15, 16, 63, 66, 125, 129]. Comparison of the experimental and theoretical results show general agreement in angular dependence but, as was the case with the total cross sections, the magnitude is significantly different, with the experimental results being larger and more forward peaked in all cases. The results of Reid *et al.* [15] are in best agreement with the experimental results in terms of the angular dependence, but the magnitude is different by a factor of almost three, and this factor is nearly constant over the range of energies covered by the experimental

results. This agreement in shape was the basis for using these results to estimate the missing contribution of the forward angle scattering to the total cross section as discussed in Chapter 4. The recent CCC results from Zammit *et al.* [16] obtain better agreement in magnitude across the experimental results, which is again represented in the comparison at the total cross section level. Other theories have varying degrees of agreement in terms of the shape of the DCS, but are much smaller in magnitude than the experimental data. One major difference between the experiments in this case, and the theoretical approaches, is the inclusion of vibrational and rotational excitation in the experimental data. This may account for some of the difference in observed magnitude, although previous measurements of the vibrational total cross section [119] suggest that this is at most only 10 % of the total scattering in this energy range, and thus not enough to make up for all of the differences in theory and experiment.

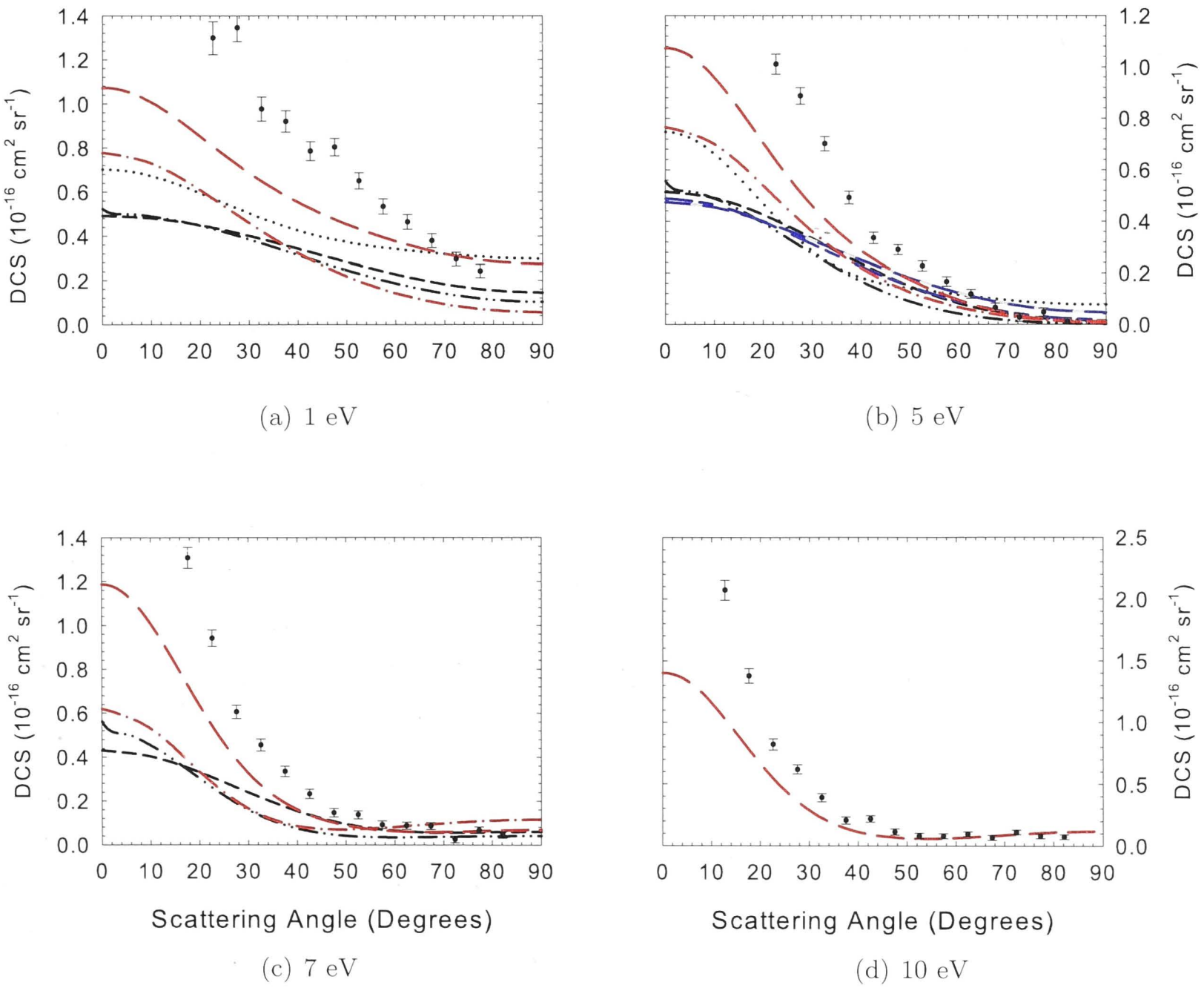

(a) 1 eV

(b) 5 eV

(c) 7 eV

(d) 10 eV

Figure 7.5: Comparison of experimental and theoretical results for elastic differential cross section at various energies. Solid circles; current experimental results. Various lines (see legend); theoretical results from Lino *et al.* [66], Reid *et al.* [15], Zhou *et al.* [63], Gibson *et al.* [125], Tenfen *et al.* [129], and Zammit *et al.* [16],

7.2.4 Elastic Total Cross Section

The results for the elastic, or quasi-elastic due to the presence of vibrational excitation, total scattering cross section above 8.2 eV are shown in figure 7.6. In the case of this measurement, the angular resolution problem described above has a larger effect, i.e. more of the forward angle distribution is missed when compared to the total cross section. This is due to the magnetic field ratio technique used to separate elastic from inelastic scattering as discussed in Chapter 4. As a result, at energies above the first electronic excitation, the measured elastic scattering does not appear to match to the total cross section below the threshold, as can be seen in figure 7.6. Nonetheless, we can make a comparison with the calculation of the elastic cross section by Zammit *et al.* [16] above the positronium formation threshold. Within the error of the experimental measurement, agreement with the calculation is good, although the effect of the missing forward angles is likely to make the comparison less favourable. On the other hand, the fact that the measurement also includes contributions from vibrational and rotational excitation would tend to raise the value of the cross section, and these effects will tend to cancel each other. It appears that the energy dependence of the cross section is a little different between theory and experiment, with a steeper decline as energy increases in the theory, although given the size of the error bars it is difficult to be conclusive.

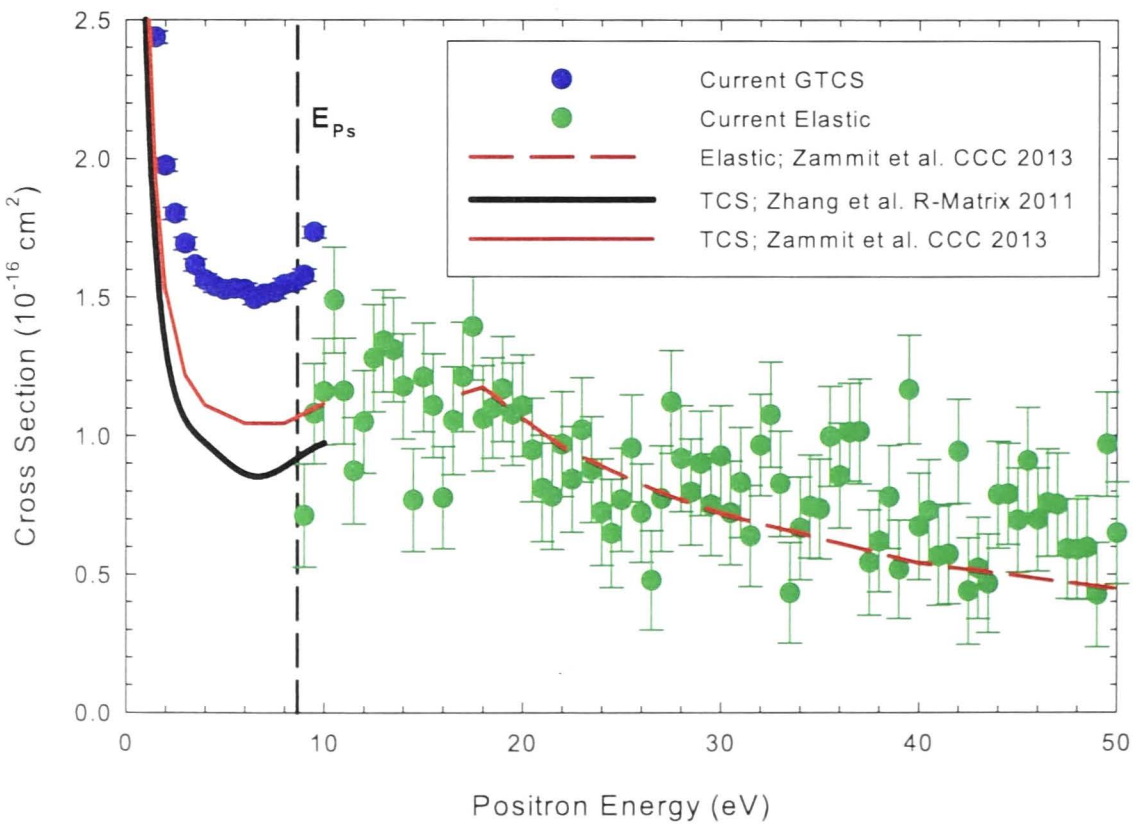

Figure 7.6: Comparison of theoretical and experimental results for the total (σ_{TCS}) and total elastic cross section ($\sigma_{Elastic}$) of positrons from molecular hydrogen (H_2). Theoretical results for the total scattering cross section from Zhang *et al.* [63], solid black line and Zammit *et al.* [16], solid red line. Theoretical results for the elastic scattering cross section from Zammit *et al.* [16], dashed red line. Current experimental results: filled blue circles, grand total scattering cross section (σ_{GTCS}): filled green circles, total elastic cross section ($\sigma_{Elastic}$).

7.2.5 Total Inelastic Cross Section

Figure 7.7 shows a comparison of the total inelastic cross section, which is the sum of inelastic scattering channels (for example electronic excitation, single and double ionization, but excluding rotation and vibrational excitation and positronium formation), up to 50 eV. We also compare this data with previous theoretical ionization and experimental electronic excitation results below 50 eV. Sullivan *et al.* [34] measured the cross section for the $B\,^1\Sigma$ electronic excitation up to 30 eV, which is included in the figure. The theoretical ionization results of Campeanu *et al.* [136], and experimental results of Fromme *et al.* [132] and Moxom *et al.* [137], have been added for a general comparison. The current results are a sum of all inelastic scattering channels and should be larger than any single partial cross section, which is consistent with what is observed in figure 7.7. However, the magnitude of the total inelastic cross section presented here is substantially larger than any of the other results, even at 50 eV where it might be expected that ionisation is the dominant inelastic process. Given fair agreement between the two experiments and the theory for this process at 50 eV, it may be possible that a significant part of this total inelastic cross section arises from electronic excitations (other than the $B\,^1\Sigma$ state), or even fragmentation. Further studies of the relevant partial cross sections would be useful to try and resolve this apparent discrepancy.

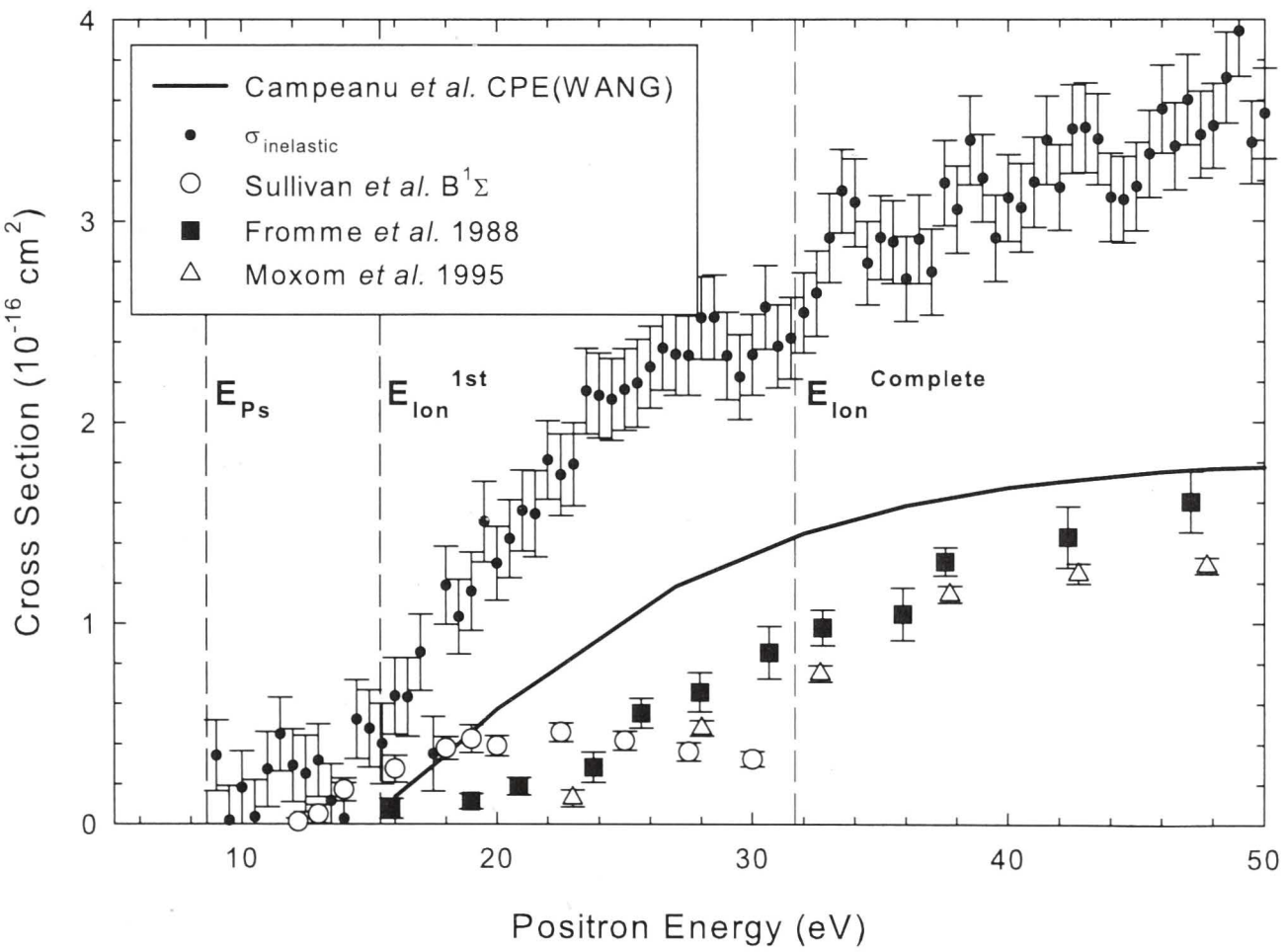

Figure 7.7: Comparison of results for the excitation of inelastic channels in positron-H_2 scattering. Current experimental results for the total inelastic cross section; solid circles, results for the excitation of the $B^1\Sigma$ state by Sullivan *et al.* [119]. Results for direction ionization of H_2; solid squares, experimental results by Fromme *et al.* [132]; hollow triangles, experimental results by Moxom *et al.* [137]; theoretical results for single ionization by Campeanu *et al.* [136]

7.3 Discussion

The role of the internuclear separation and the ro-vibrational motion of the molecule is likely to play a critical role in the convergence of theory and experiment at low scattering energies. Recall that the vibrational excitation cross section is non-zero even at 5 eV and may couple to the elastic channel. A simple example of how the scattering length is effected by changing the internuclear separation is shown in figure 7.8. Figure 7.8 is a plot of the scattering length as a function of internuclear separation from Zhang *et al.* [138] with the mean value of R used in the most recent calculations by Zammit *et al.* [16] indicated.

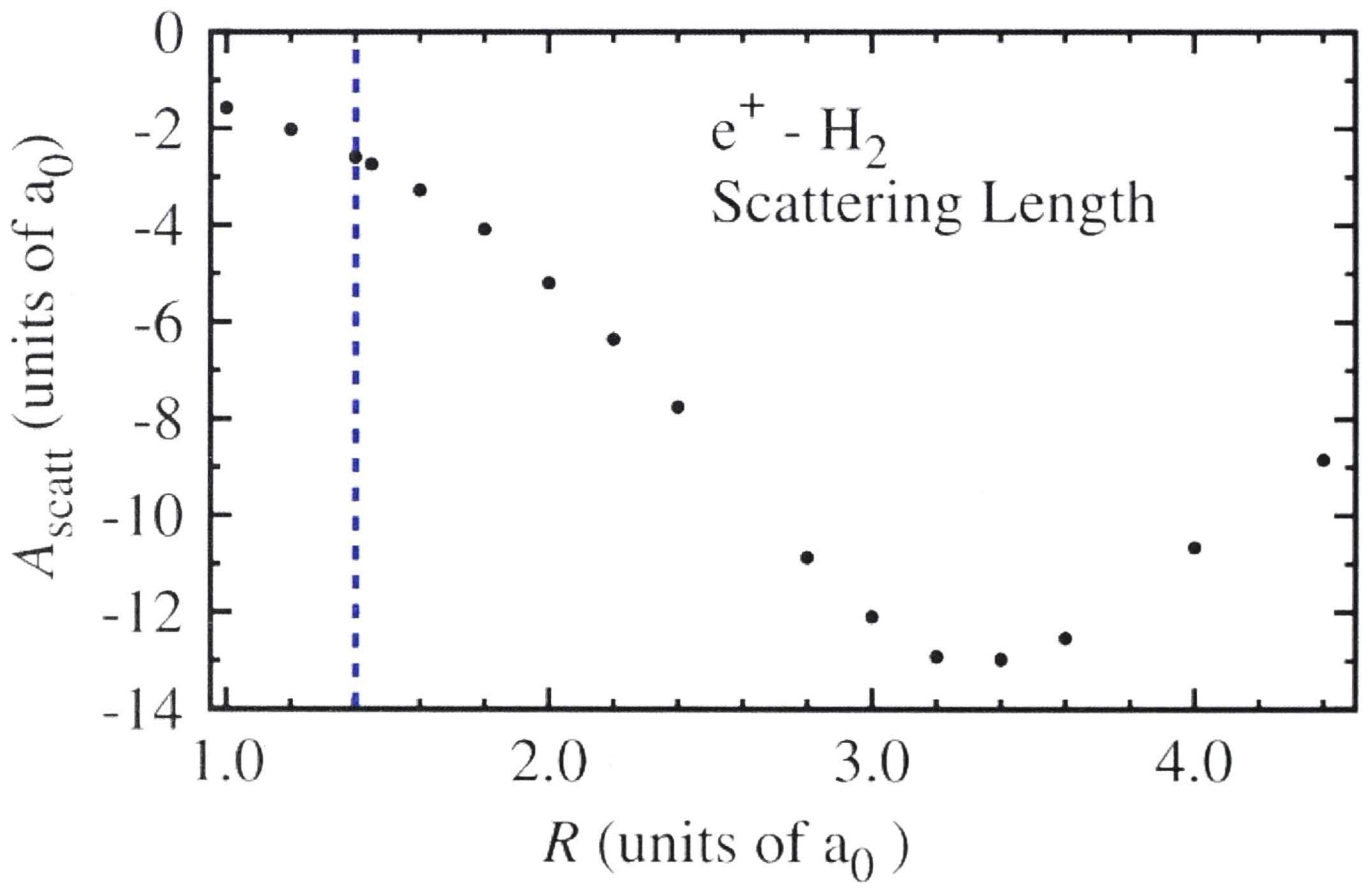

Figure 7.8: Calculation of the scattering length for a number of internuclear separations from Zhang *et al.* [138]. The vertical blue dashed line indicates the mean value of the internuclear separation used in calculations.

7.4 Conclusion

We have reported measurements of a number of total and partial cross sections for positron scattering from H_2. Comparison between the present experiment and the other recently published experimental data shows excellent agreement, with observed differences largely explained by a consideration of the differences in forward angle discrimination. The available theoretical results for the total cross section, however, are significantly different in magnitude at low energies to the experimental data. This difference is in part due to the inclusion of vibrational and rotational scattering in the experiments, but not the calculations, although this is unlikely to account for all of the differences. However, the inclusion of a variation in the internuclear separation into calculations may provide some insight. The measured positronium formation cross section is in good agreement with

previous work, including one of the calculations reported by Biswas *et al.* [135]. We have also reported the total inelastic scattering cross section which appears to indicate some discrepancies when considering previous work on total inelastic measurements, but may be explained by the fact that unmeasured (or calculated) processes such as electronic excitation have a larger magnitude than may be initially assumed. Given the discrepancies observed, there is clearly scope for further detailed studies of positron scattering from molecular hydrogen, particularly as this represents the simplest molecular target readily available for comparison between experiment and theory. Understanding and benchmarking of simple systems such as this is crucial for further developing a detailed understanding of low energy positron scattering.

Chapter 8

Search for Threshold Cusps in Molecular Targets

This chapter presents a search for features in the quasi-elastic scattering cross section due to the opening of the positronium formation in positron-molecule scattering. The theoretical description of a cusp was developed for nuclear scattering and is briefly reviewed. Comparisons are made to previous experimental results for positron scattering showing channel coupling in positron-atom scattering. A review of the results and discussion of the relevant scattering channels is presented, along with comparisons to electron scattering.

8.1 Introduction

Channel coupling, in the form of cusps, in elastic scattering channels at the opening of an inelastic scattering channel was first described by Wigner [139]. This original work was inspired by nuclear scattering scattering experiments in which cusps occurred in the elastic scattering channel due to the onset of a new production channel. A similar case exists in positron scattering at the onset of the positronium (Ps) formation channel as reported by Jones *et al.* [20] and discussed in Chapter 2. Signatures of channel coupling are commonly found in electron scattering in the form of Wigner cusps in the elastic scattering cross section, due to the onset of a strong inelastic scattering channel [19]. In positron scattering, the positron formation channel is the analogous strong scattering channel.

The first search for a cusp feature in the region of the Ps formation threshold was undertaken by Campeanu *et al.* [140]. An approximate elastic scattering cross section was determined by subtracting a Ps formation cross section measurement from a measurement of the grand total scattering cross section. This resulted in a total elastic scattering cross section, which had an apparent cusp at the Ps formation threshold, and dropping by nearly 20 % before the threshold of the first electronic excitation at 20.62 eV. An early experimental search for a cusp in the elastic scattering cross section for positron scattering helium about the positronium formation threshold energy was undertaken by Coleman *et al.* [141]. In these measurements, the predicted decrease in the elastic scattering cross section across the Ore gap was not observed, but a cusp could not be ruled out due to the

resolution limitations of the experimental apparatus.

A theoretical exploration of the elastic scattering cross section, for positron scattering for noble gases other than helium, was undertaken by Meyerhof and Laricchia [142] using the R-Matrix approach. These results indicated the presence of a cusp in the elastic scattering cross section at the Ps formation threshold for neon through to xenon. Theoretical work, using the Kohn variational method, was undertaken by Van Reeth and Humberston [143] for positron scattering from helium and atomic hydrogen in an attempt to reproduce the results of Campeanu *et al.* [140] and determine the magnitude for comparison to the experimental results of Coleman *et al.* [141]. They found a small cusp in the elastic scattering channel for positron scattering from helium and atomic hydrogen. The calculated cusp in the elastic scattering cross section was due to the onset of the positronium formation channel, but had a different energy dependence than that reported by Coleman *et al.*.

The results of Jones *et al.* [20], showed distinct cusp features in the elastic scattering cross section for positron scattering from a range of noble gases. Figure 8.1 shows a comparison from Jones *et al.* of the various cusp measurements in helium and the calculation from Van Reeth and Humberston. The results of Coleman *et al.* and Jones *et al.* share the same energy dependence below 20 eV, but are in contrast to the theoretical calculations. No other theoretical calculations have attempted to tackle this difficult scattering problem as discussed in Chapter 2.

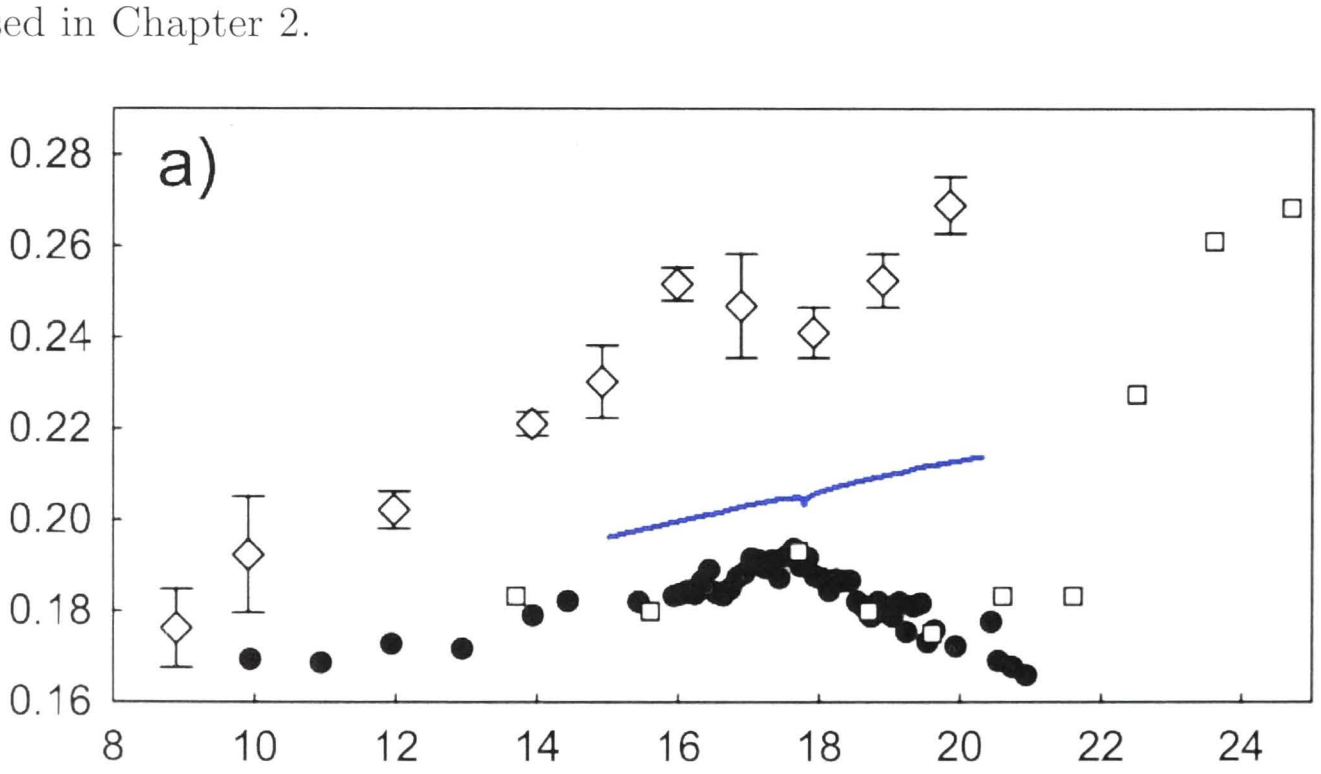

Figure 8.1: Comparison of experimental results about the positronium formation threshold taken from Jones *et al.* [20] for positrons elastically scattered from helium: solid circles, experimental results from Jones *et al.*; open diamonds, experimental results from Karwasz *et al.* [144]; open squares, experimental results from Coleman *et al.* [141] and the blue line are theoretical results from Van Reeth and Humberston [143].

The results of Jones *et al.* [20] demonstrate that the nobles gases, helium thru to xenon, all show a cusp feature centered about the positronium formation threshold energy in the elastic scattering cross section. The series of Wigner cusps in the noble gases appear Lorentzian in shape, but no trend was found in magnitude of the cusps, but the width

of the cusps were all nearly the same, leaving the question of the dominant mechanisms open. In an effort to elucidate this problem, a search for cusp features due to the onset of positronium was undertaken for a series of molecules isoelectronic with helium (H_2) and neon (H_2O, NH_3 and CH_4). Molecules have additional degrees of freedom due to the their structure resulting in additional scattering channels, vibrational for example, which are open at the Ps formation threshold, discussed in Chapter 2. The molecular targets in this search range from linear (H_2) and progress to effectively spherical (CH_4).

8.2 The Wigner Cusp

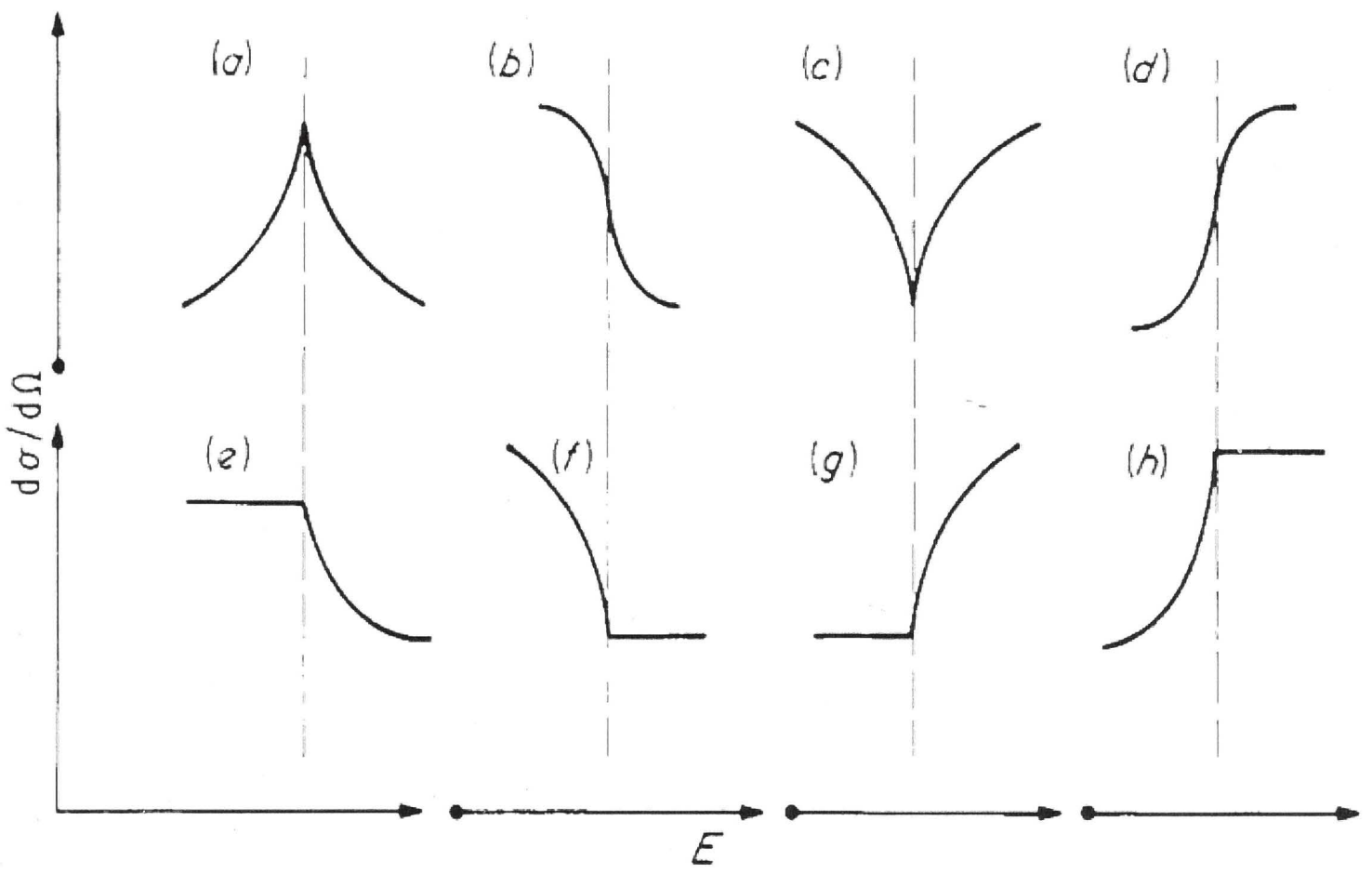

Figure 8.2: The family of cusps from Eyb and Hoffmann [19].

Wigner produced a formalism which describes the shape of the scattering cross section about the threshold of a new production channel. This formalism can be used, for example, to describe the case of electron scattering and has been reviewed in a number of publications [19, 145]. A cusp feature can occur in the elastic scattering cross section due to the strong opening of an inelastic scattering channel. This cusp has both angular and energy dependence [19]. The differential scattering cross section can be written, see also section 2,

$$\delta(\theta, E) = |f_t(\theta)|^2 - A_0|f_t(\theta)||E - E_t|^{1/2} \begin{cases} sin(2\delta_0 - \alpha) & E > E_t, \\ cos(2\delta_0 - \alpha) & E < E_t, \end{cases} \tag{8.1}$$

where

$$f_t = \frac{1}{2ik_t}\sum_{l=0}^{\infty}(2l+1)(e^{2i\delta_t}-1)P_l(cos\theta), \tag{8.2}$$

is the scattering amplitude at the threshold energy, E_t, k_t is the corresponding wave number, δ_l is the phase shift for angular momentum l, and P_l are the Legendre polynomials. The second term in equation 8.1 describes the interaction of the elastic and inelastic channels about the threshold energy, E_t. The amplitude of the coupling is defined by the positive constant, A_0, δ_0 is the phase shift of the s partial wave (l=0) at the threshold energy and α is defined as $f_t(\theta) = |f_t(\theta)|e^{i\alpha(\theta)}$.

This assumes that s-wave scattering dominates near threshold leading to the Wigner threshold law,

$$\delta_{in}^{l} \propto (E - E_t)^{l+1/2}, \tag{8.3}$$

and provides the form for the background scattering amplitude about the threshold energy. The shape of the cusp or step is dependent on the phase shift in the second term of equation 8.1, δ_0 and a series of cases of the phase $2\delta_0 - \alpha$ shown in figure 8.2. Here, Eyb and Hoffman [19] have compared a series of cases: fixing the coupling constant, A_0, and the scattering amplitude, f_t, and considering $n = 0, 1, 2, 3$ we have cases (a) thru (d) where $2\delta_0 - a = \frac{\pi}{4} + \frac{n\pi}{2}$ and cases (e) thru (h) where $2\delta_0 - a = \frac{\pi}{4} + \frac{n\pi}{2}$. Van Reeth and Humberston used a variational calculation to determine a cusp in positron-helium scattering. This cusp had the character of case (c) in figure 8.2 which implies that the term $2\delta_0 - a = \frac{\pi}{4} + \frac{n\pi}{2}$.

8.3 Results

A series of measurements of positron-molecule scattering was undertaken to search for Wigner cusps about the onset of the positronium formation threshold in each of the molecules. The results of Jones *et al.* [20] were used as motivation for the current search. These results are the first dedicated search for channel coupling in positron-molecule scattering about the positronium formation threshold.

8.3.1 Isoelectronic Series of Helium: H_2

A cusp has been observed in the elastic scattering cross section for positron scattering from helium [5, 20]. As discussed, theory and experiment are in disagreement as to the shape or energy dependence of the elastic scattering cross section. Molecular hydrogen is isoelectronic with helium and a detailed set of cross sections for positron-H_2 scattering are presented in Chapter 7. The quasi-elastic (containing vibrational excitation) scattering cross section was measured in detail about the positronium formation threshold to look for a cusp feature. The results are shown in figure 8.3 with the results for positron-helium scattering shown for comparison, both experimental results are fitted with an idealised peak shape constructed from a Lorentzian profile on a linear background. A cusp in the

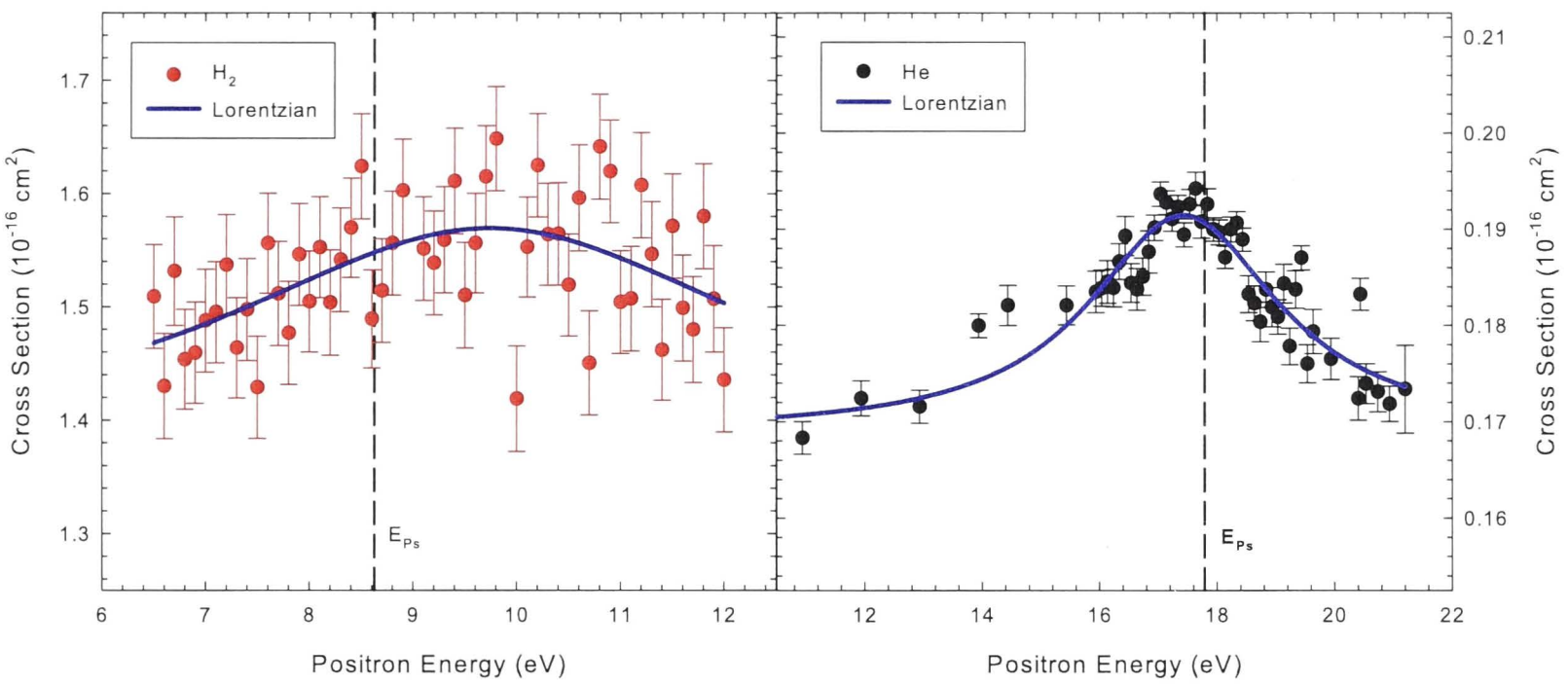

Figure 8.3: Comparison of the elastic scattering cross sections for H_2 and He in the region of the positronium formation threshold. The solid line is a fit to the experimental data in an attempt to parameterise relevant aspects of cusp behavior. The fit was composed of a Lorentzian profile plus a linear background.

elastic scattering channel is not clearly seen for molecular hydrogen. The cusp, in the helium case, is centered on the positronium formation threshold whereas the peak in the fit observed in molecular hydrogen is centered around 10 eV. The first electronic excitation is at 11.8 eV and the positronium formation threshold is at 8.68 eV. Therefore it is likely that the shape of the cross section for H_2 is consistent with the expected smooth variation seen for many other scattering cross sections.

8.3.2 Isoelectronic Series of Neon: H_2O, NH_3, and CH_4

Of all the noble gases investigated by Jones *et al.* [146], Ne has the smallest cusp (4.1 ± 1 %) as a percentage of the grand total scattering cross section at the positronium formation threshold. The current result, see figure 8.4, confirm the magnitude and shape of the cusp previously observed (5.2 ± 2 %). The line of best fit is for the current data set and the fit from Jones *et al.* was not plotted. The statistical character of the data does not rule out a cusp of type (a) of figure 8.2 from [19], but the data of Jones *et al.* is indicative of a Lorentzian shape.

The only available results for positron-water scattering in which the quasi-elastic scattering cross section was reported are those of Makochekanwa *et al.* [92]. These results were unable to detect a feature in the quasi-elastic scattering cross section about the positronium formation threshold. These results have been compared to the current results in figure 8.5. The statistical quality of the data is similar, with a small discrepancy in the absolute magnitude. Neither set of experimental results were able to observe a cusp feature similar to that observed in neon by Jones *et al.* [20]. In the case of water, the quasi-elastic scattering cross section is nearly linear in shape over the region observed with each data set

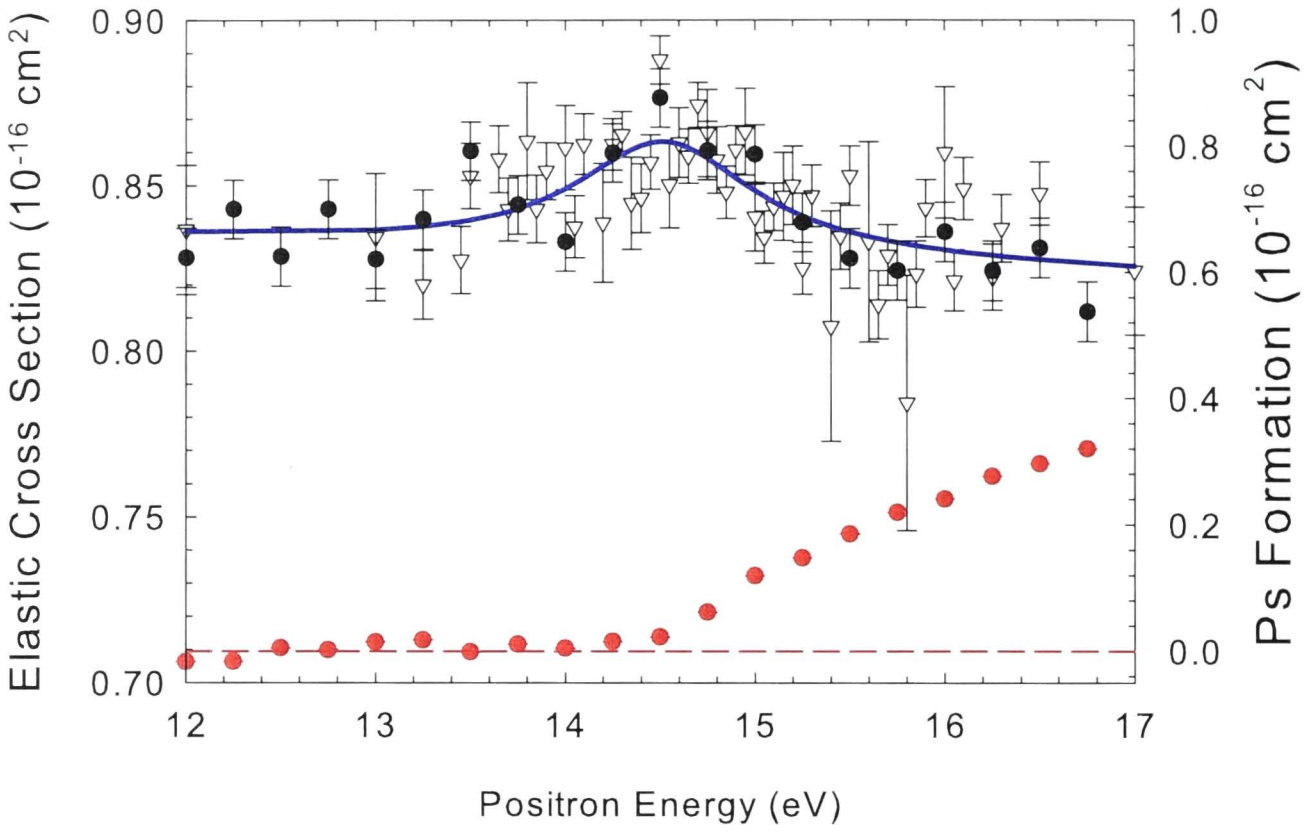

Figure 8.4: Comparison of results for positron scattering from Neon. The results for the quasi-elastic scattering cross section: solid black circles; current results, open triangles; results of Jones *et al.* [20]. The results for the positronium (Ps) formation cross section: current results, solid red circles. The horizontal red dashed line indicates the zero value of the Ps formation cross section. The solid blue line is a fit to the current quasi-elastic scattering cross section cross section, see the text for details.

reporting the same slope with no cusp on the order of those seen in the noble gases. The positronium formation cross section appears to turn on in a linear fashion.

Only one previous study of positron-ammonia scattering has been undertaken by Sueoka *et al.* [147] where the grand total scattering cross section was measured. These results give no indication of a feature about the postronium formation threshold, but the Wigner cusps in the noble gases were observed in the elastic, and not observed in the grand total, scattering cross section. The current results are shown in figure 8.6 and, similar to the case for water, a nearly linear energy dependence is seen in the quasi-elastic scattering cross section about the positronium formation threshold indicated with a vertical dashed line.

There are a large number of previous experimental results for positron-methane scattering [123, 148–151]. These previous results measured only the grand total scattering cross section and no measurement of the positronium formation absolute cross section has been available until now. Previously, Charlton *et al.* [152] measured the formation of ortho-positronium (o-Ps) as a function incident positron energy, but assigned no absolute value. This measurement gave a similar shape near the observed threshold, but reports a threshold lower than the Ps formation threshold, of 5.81 eV, and have not been included for clarity. While no quasi-elastic scattering cross sections are available for methane in the literature, the vibrational excitation cross sections have been measured by Sullivan

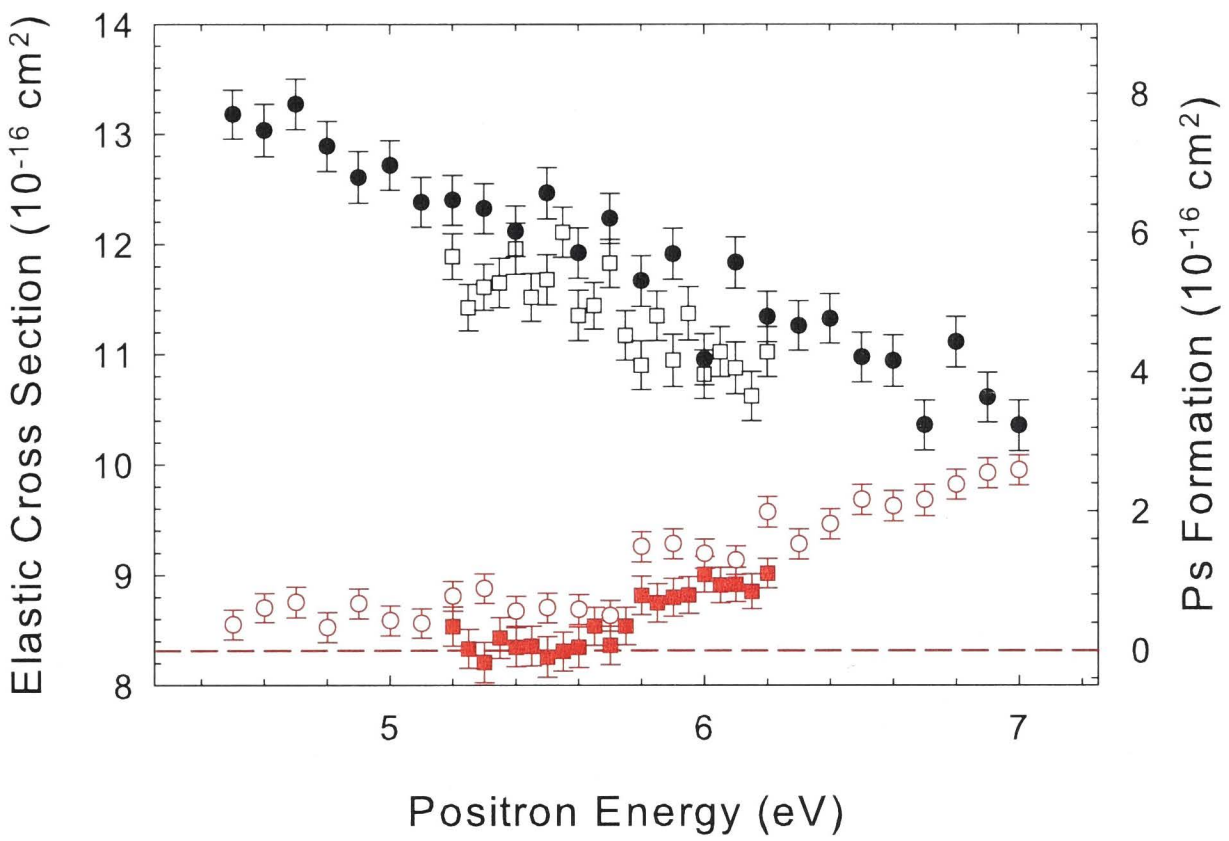

Figure 8.5: Comparison of results for positron scattering from Water (H_2O). The results for the quasi-elastic scattering cross section: filled black circles; current results and open squares; results of Makochekanwa *et al.* [92]. The results for the positronium (Ps) formation scattering cross section: open red circles; current results and filled red squares; results of Makochekanwa *et al.* [92]. The horizontal dashed line indicates the zero value of the Ps formation cross section.

et. al. [38] and will be discussed below in the context of the comparison between Wigner cusps in atomic versus molecular systems. The current quasi-elastic scattering cross section results are shown in figure 8.7. The energy dependence is again nearly linear about the positronium formation threshold, indicated by a vertical dashed line in the plot. The positronium formation cross section turns on with no corresponding feature about the threshold consistent with the other molecules in this series.

8.4 Discussion

No apparent Wigner cusp is observed for positron scattering from any molecules in the two series investigated here. Molecular hydrogen is a diatomic molecule which can be vibrationally and rotationally excited. These excitations have threshold energies well below the positronium (Ps) formation threshold and constitute many open scattering channels at the Ps formation threshold. Sullivan *et al.* [88] measured the vibrational excitation of the ν_1 mode and extrapolation of the experimental data puts the vibrational excitation of H_2 at approximately 0.1 Å^2 or $\sim$ 6 % of the scattering cross section at the Ps formation threshold. At the Ps threshold in H_2 there are about 15 vibrational channels open in addition to numerous rotational channels and dissociation. The peak magnitude of the cusp observed in helium was 11 % $\pm$ 1.0 %. The cusp in helium and the vibrational excitation cross section in H_2 are the same order-of-magnitude as a percentage of the grand

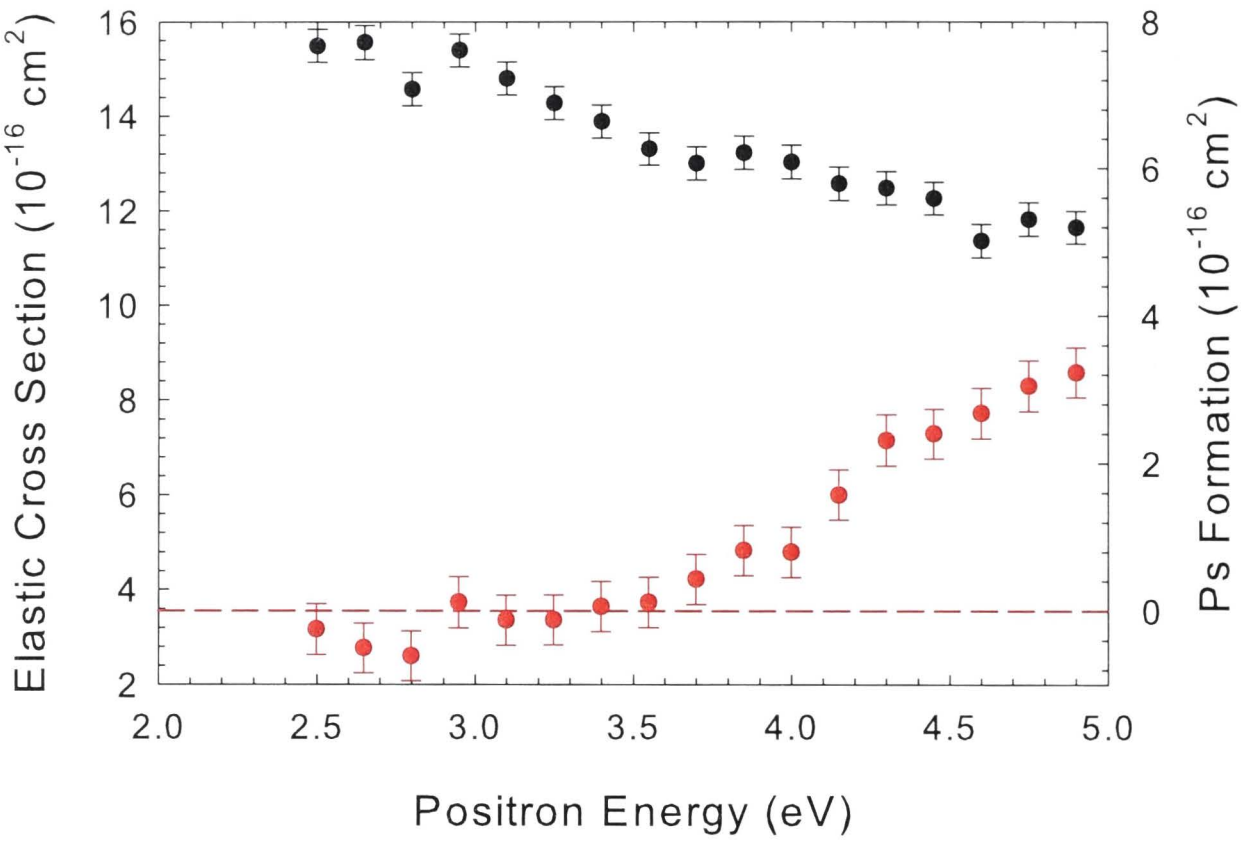

Figure 8.6: Results for positron scattering from Ammonia (NH_3); solid black circles, quasi-elastic scattering cross section and solid red circles, positronium (Ps) formation. The horizontal dashed line indicates the zero value of the Ps formation threshold.

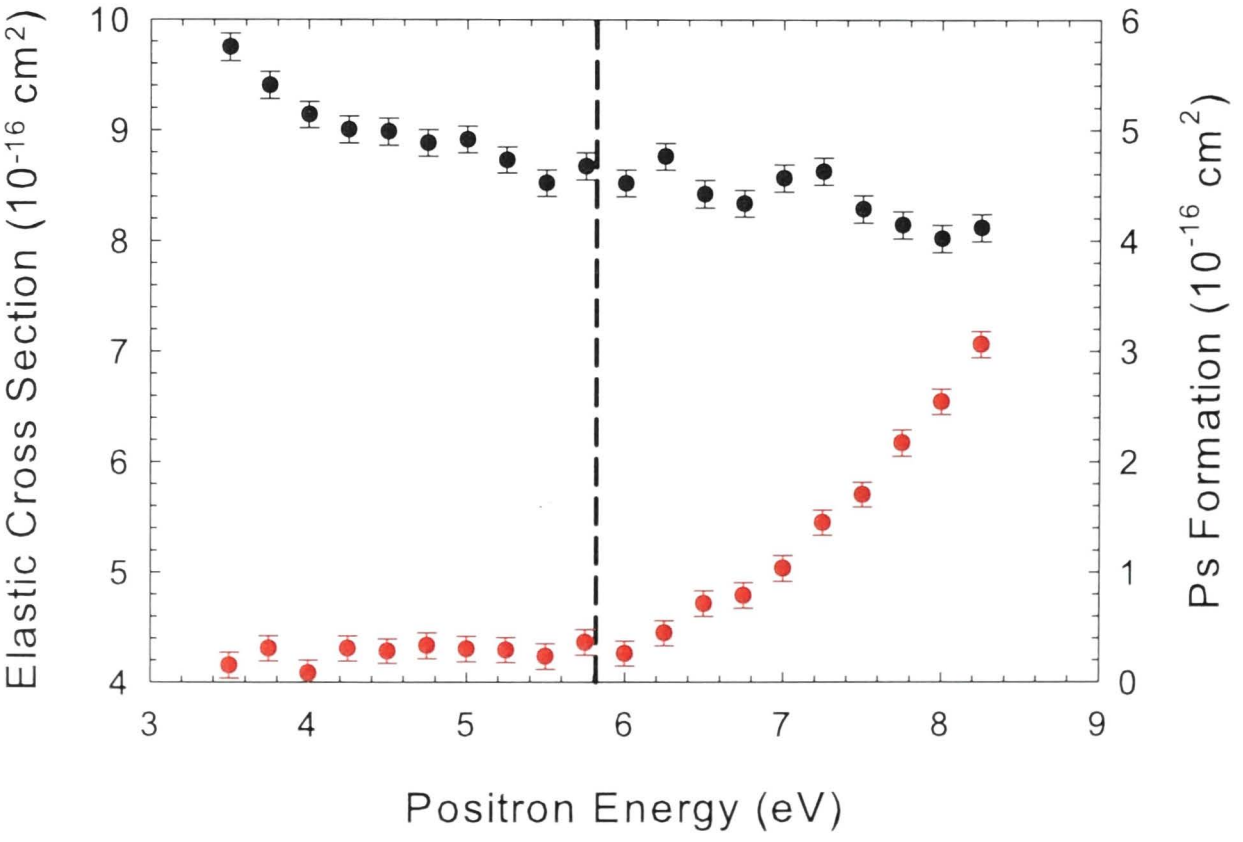

Figure 8.7: Results for positron scattering from Methane (CH_4). The quasi-elastic scattering cross section are the solid black circles and the positronium (Ps) formation cross section are the solid red circles.

total scattering cross section. Thus if a cusp feature is present, it is considerably narrower in energy or smaller in magnitude than in the atomic case. However, the presence of many such additional scattering channels with a non-zero cross section could possibly suppress the observation of the cusp by sharing the coupling between all open channels.

Table 8.1: Atomic and molecular configurations and parameters: ionisation potential; I.P., first electronic excitation; 1^{st} e^*, static dipole moment, μ ; dipole polarizability, α. See NIST Atomic Spectral Database (ASD) [153] and NIST Webbook [154].

Target	Configuration	I.P. (eV)	1^{st} e*	μ	α
He	$1s^2$	24.587	20.62	0	1.383
Ne	$[\mathrm{He}]2s^2 2p^6$	21.564	16.62	0	24.56
Ar	$[\mathrm{Ne}]3s^2 3p^6$	15.760	11.55	0	83.80
Kr	$[\mathrm{Ar}]3d^{10}4s^2 4p^6$	14.000	9.92	0	115.79
Xe	$[\mathrm{Kr}]4d^{10}5s^2 5p^6$	12.130	8.32	0	161.4
H_2	$X^1\Sigma_g^+$	15.426	11.19	0	6.74
H_2O	$(1a_1)^2(2a_1)^2(1b_2)^2(3a_1)^2(1b_1)^2, \tilde{X}^1A_1$	12.617	7.14	1.85	9.78
NH_3	$(1a_1)^2(2a_1)^2(1e)^4(3a_1)^2, \tilde{X}^1A_1$	10.186	5.67	1.42	14.56
CH_4	$(1a_1)^2(2a_1)^2(1t_2)^6$, $^1A_1$	12.618	8.61	0	17.61

Table 8.2: Vibrational Mode Energies and Symmetries (NIST Webbook) [154]

Target	Mode	E_ν (meV)	Symmetry	Sym. Species
H_2O	ν_1	453.4	$C_{2\nu}$	a_1 Sym. Str.
	ν_2	197.8		a_1 Bend
	ν_3	465.7		b_2 Anti. Str.
CH_4	ν_1	361.7	T_d	a_1 Sym. Str.
	ν_2	190.2		e Bend
	ν_3	374.3		f_2 Deg. Str.
	ν_4	161.9		f_2 Deg. Deform
NH_3	ν_1	413.7	$C_{3\nu}$	a_1 Sym. Str.
	ν_2	117.8		a_1 Sym. Deform
	ν_3	427.0		e Deg. Str.
	ν_4	201.7		e Deg. Deform

No Wigner cusps are observed for positron scattering from the isoelectronic series of Neon: Water, Ammonia and Methane. Again, if a cusp feature is present it is narrower in energy or smaller in magnitude that in the atomic case. Recall that for the case of the noble gases, only two scattering channels are possible below the first electronic excitation; quasi-elastic scattering and positronium formation, neglecting direct annihilation. In the case of the isoelectric series of Ne, the first electronic excitation is above the positronium formation threshold for all three molecules, see Table 8.1. However, each molecule has a number of fundamental vibrational modes, Table 8.2, which open at hundreds of meV collision energy.

Water has three normal vibrational modes listed in Table 8.2. A recent attempt at measuring these modes was unsuccessful in completely separating the second vibrational mode from quasi-elastic scattering, but the measurement was consistent in magnitude with

electron scattering data of Khakoo *et al.* and El-Zein *et al.* [155, 156]. This electron data can be used to estimate the magnitude of the total vibrational cross section at the opening of the Ps formation channel is nearly 1 Å. This is nearly 10 % of the total scattering cross section at the Ps formation threshold whereas the magnitude of the cusp in Neon was 5.2 $\pm$ 2 %.

Ammonia has four normal vibrational modes listed in 8.2. Vibrational excitation of ammonia via positron impact has not been measured with results for vibrational excitation via electron impact sparse in this case. However, some data does exist from Gulley *et al.* [157] for electron scattering, near the positronium formation threshold energy. Integrating the differential cross section for the first and third vibrational modes nearest the Ps threshold yields a value of 0.58 Å. This is $\sim$ 4 % percent of the grand total scattering cross section at the positronium formation threshold of 3.3 eV.

Methane has four normal vibrational modes. The cross section for the excitation of these modes from ground state by positron impact has been measured by Sullivan *et al.* [88]. In those experiments the first and third modes were degenerate as were the second and the fourth due to the finite energy resolution of $\sim$ 25 meV [88]. These measurements extended from threshold to 6 eV. From these results the magnitude for the excitation of the $\nu_1 + \nu_3$ modes, at the Ps formation threshold of 5.81 eV, are $\sim$ 0.2 Å and for the excitation of the $\nu_2 + \nu_4$ modes are $\sim$ 0.1 Å. Therefore, at the onset of positronium formation the total cross section for vibrational excitation is $\sim$ 0.3 Å with four channels open, ignoring the possibility of overtones. Overtones increase the density of states and may have a strong effect on the channel coupling. Measurements of the quasi-elastic scattering cross section in the region about the Ps formation threshold are shown in figure 8.7. No cusp feature is observed about the Ps formation threshold. At this energy the vibrational excitation cross section has a magnitude of $\sim$ 4 % of the total scattering cross section whereas the cusp in Neon was $\sim$ 5 % of the total.

The Lorenztian shape was chosen empirically to analyse the experimental data of Jones *et al.* [20]. The idealised peak shape was constructed from a Lorenztian profile on a linear background and was adequate to describe the experimental data based on the statistical nature of the data. Searching molecules isoelectronic with helium and neon have shown no such cusp features due to the onset of the positronium formation channel. Eyb and Hoffman have shown that there are a number of possible shapes of Wigner cusp which depend on the phase between the already open channel and the opening channel or δ_0, see figure 8.2. This search focused on cusps of a similar magnitude and shape as those seen in the noble gases by Jones *et al.* finding none, but not ruling out sharper features or features smaller in magnitude.

8.5 Conclusion

These are the first measurements searching for channel coupling in the form of Wigner cusps in positron scattering from molecules; H_2, H_2O, NH_3 and CH_4. The null measure-

ment of a cusp feature in these molecules is likely due to open and non-zero vibrational excitations at the Ps formation threshold suppressing the magnitude below that detectible by the current experimental setup. Alternatively, the large number of states, in the molecular case, may distribute the channel coupling, with no strong coupling to a single state. While no cusp was observed in molecular hydrogen, a further detailed experimental study of positron scattering from diatomic molecules may provide further insight as the vibrational structure is less complicated that the molecules in this series. Ultimately, a molecular system which has a negligible vibrational excitation cross section at the threshold for positronium formation would be ideal for testing the effect of the density of states. Further theoretical work in calculating the magnitude and shape of Wigner cusps would be of great utility to a future experimental exploration to guide the experimental requirements. This is particularly important since the only available theoretical prediction reports a shape and magnitude (in positron scattering from helium) in stark contrast to that measured by experiment. It is possible that cusps are present in these molecules, but smaller in magnitude than the current set of experiments was able to measure. This limits the utility of these measurements in determining a trend in cusp formation in positron scattering from molecules. Separation of vibrational and rotation excitations so a true elastic scattering cross section could be determined for these molecular targets may be required to detect a cusp, and provide greater physical insight in to this coupling phenomena. As no trend was found in cusp results for the noble gases, a more thorough theoretical and experimental investigation of these cusps and their formation mechanism is also warranted.

Chapter 9

Rotating Wall

This chapter describes the theory of operation and implementation of a rotating wall electrode in the buffer-gas trap. Particular attention is drawn to the energy distribution of the resultant positron pulse as well as the absolute number of positrons trapped. Comparisons are made between previous work where applicable.

9.1 Introduction

The accumulation of large numbers of positrons to form a positron plasma was demonstrated by Surko *et al.* [158] and control of the positron plasma using the rotating electric field compression technique developed for plasma control [159,160] was subsequently shown by Greaves and Surko [161]. This work was extended by Greaves *et al.* [162] to demonstrate the compression of a positron cloud that is not in the plasma regime. This chapter covers the implementation of a rotating electric field compression technique to increase the central density of the positron beam, and reduce the diameter of the beam, for application to fundamental atomic and molecular scattering experiments.

A rotating wall electrode cut into four quadrants with an oscillatory field applied such that each quadrant is out of phase by 90 degrees in circulation produces an asymmetric dipolar electric field rotating at the applied field frequency. It is this oscillatory field which allows control of the radial extent of the positron beam in the form of heating [161] whereas the applied DC potential determines the collision energy which determines the interaction between the positron and the trapping and cooling gases.

9.2 Theory

When the positron density is low, compression of the positron cloud can be described as coupling to the bounce frequency within the confining potential well [162],

$$\omega_z = \sqrt{\frac{qV_o}{md^2}} \tag{9.1}$$

where V_o is the potential well depth, d is the length of the well, m is the mass of the trapped particle (positron) and q is the charge of the positron. Since a positron trap and accumulator typically use a diatomic gas for trapping and polyatomic gas for cooling,

a Stokes viscous drag is present in the full description of the positron's motion in the potential [163] thereby complicating the description.

9.3 Implementation

As discussed previously in Chapter 3, positrons were trapped and cooled in a Surko-style buffer-gas trap. One of the electrodes in the trap was divided into four electrically-isolated quadrants. A combination of static and oscillating field was applied using a combination of the analog-output (PXI-6733) and amplifier (T506) and a radio frequency (RF) signal generator based on an AD9854 DDS or Direct Digital Synthesizer and designed and constructed at the ANU. The circuit allowed a DC-bias potential to be added to four phase-shifted signals before coupling to the electrode via coaxial feedthroughs. This resulted in a radio-frequency oscillatory potential applied to the segmented electrodes,

$$\Phi_i = A\, cos\,(\omega t + \phi_i) + V_{Bias}, \tag{9.2}$$

where i = 1,2,3,4 for each segment for $\phi_i = 0°$, $90°$, $180°$, $270°$ and V_{Bias} is the DC potential provided by the high-voltage amplifier. Each phase could be tuned using adjustable lumped circuit filters to provide the same amplitude to each phase. This resulted in four signals with the same amplitude, but out of phase by $\pi/2$ or $90°$. The frequency response of the lump circuit limited the usable output frequency to approximately 22 MHz. The maximum amplitude of the RF signal was $\sim$ 1.4 V_{p-p}.

9.4 Operation

The dumping technique used, see Chapter 3 §3.3.1, required the well electrode to be raised and lowered during the trap cycle, see Chapter 3. When the RW-electrode was used as the well electrode, resulting signal was not ideal (AC + DC) due to loading affects. Rather than rebuilding the coupling circuit, the RW-electrode was move into the load section of the trap or from position 8 to position 6 as seen in figure 3.7 of Chapter 3. Thus the DC or V_{Bias} potential did not vary over a trap cycle. The RF potential could be applied for part or all of the trap cycle, but generally it was run continuously during loading, cooling and dumping of the positron beam, which lead to the greatest improvement in throughput.

The trap cyclic rate was $\sim$ 100 Hz with the loading stage constituting of more than 60 % of the cycle time. The RW electrode was in position E6, see Chapter 3, or near the longitudinal centre of the trap. During loading, the RW field was applied, off of centre, to a very anharmonic potential very different to the normal configuration [161]. Over the extent of the RW electrode the DC potential was nearly constant. However, during the cooling and dumping of the positron beam, the adjacent electrode (E7) was raised to isolate the part of the positron beam which was to be cooled before dumping. This changed the DC potential to that similar to the standard configuration for compression, albeit slightly anharmonic, and the RF field only covered about a quarter of the positron

beam. Thus during the cooling and dumping of one component of the positron beam, the other was being tailored using the RW electrode.

9.5 Results

The time scale of accumulation and dumping of the positron beam in this implementation of a Surko-style buffer-gas trap was significantly faster than those used for previous positron compression studies [161]. However, compression has been observed on shorter time scales resulting in an increase in the central density of 20 % [164]. In an effort to explore the effect of the RW potential the amplitude (A) and frequency (f) were varied for a fixed well depth, see figure 9.1. The resulting phase space plot indicates a strong peak at approximately the bounce frequency of the positron in the potential well. In the experimental system a beam defining aperture, 4.5 mm in diameter, is present in the system whereas the inner diameter of the trap electrodes are 2 cm. Due to collisions with the trap gases positrons will diffuse to fill the space radially, subject to the collision energy. Therefore, observation of an enhancement of the number of positrons at the bounce frequency which is proportional to the amplitude of the applied RF signal is evidence of radial compression of the positron beam.

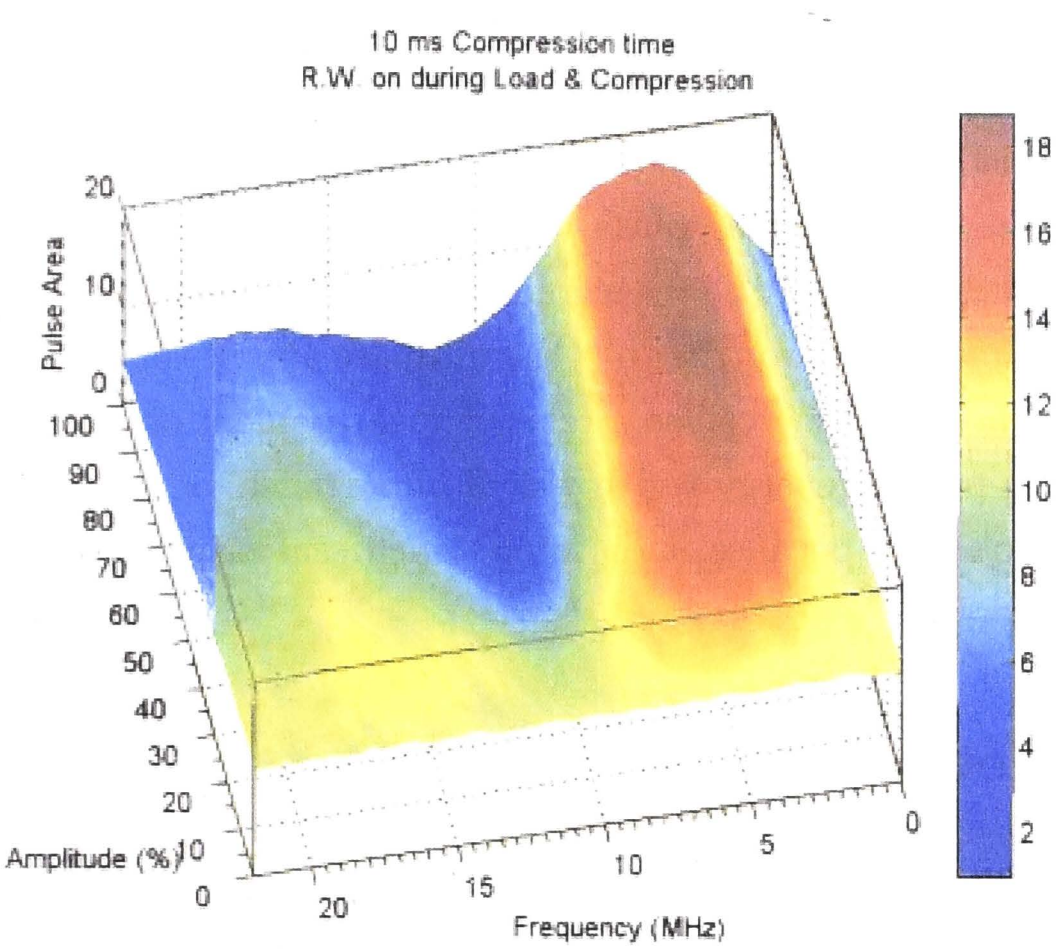

Figure 9.1: Colormap plot showing the phase space of RW signal. Frequency and Amplitude of the RF signal were varied and the resulting positron signal recorded. Pulse area is proportional to number of positrons.

The effect of the RF field on the positron beam can be readily seen in the parallel

energy width or $E_{||}$. The energy with is 40 meV when the RF field is off, but when the RF field is applied the positron beam energy spread increases to 80 meV, see figure 9.2.

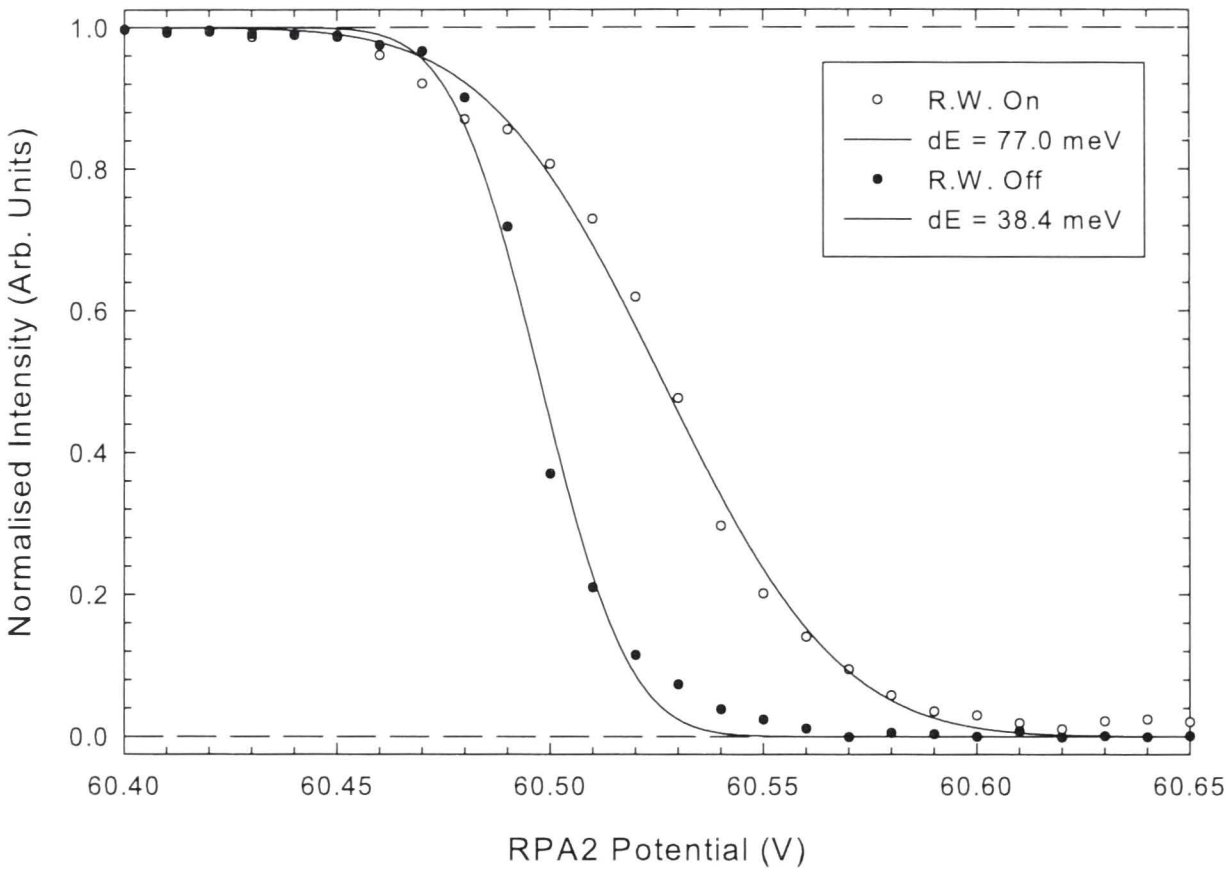

Figure 9.2: Comparison of the positron beam parallel energy distribution between the on and off states of the RF field.

The measurement of the positron cloud was done without the use of imaging techniques. Instead, the amount of charge per pulse was measured and compared as a function of frequency or amplitude because the measurement of the total charge of the beam require less accumulation time. It is also true that the ultimate aim of this work was to put more positrons through the scattering cell so a relative measurement of intensity was sufficient. Measurement of the parallel energy width was of importance for scattering measurements from atoms and molecules because it dictated which scattering measurements could be undertaken, see Chapter 3.

9.6 Discussion

The main difference of this to previous implementations is the trap repetition rate of $\sim$ 100 Hz versus 4 Hz of Cassidy *et al.* [164]. We observe a similar percentage improvement, but our measurements are aperture specific and do not constitute a direct measure of the trapping efficiency.

In the context of scattering experiments the increase in the parallel energy width becomes an issue when trying to measure processes which are separated by smaller than the energy width of the beam or if you want to measure small features, like the onset of Ps formation or resonant structures. This is likely due to the RF field permeating the entire trap cavity effectively heating positrons in the trap during the entire trap cycle

resulting in an increase in the parallel energy width of the beam. However, as discussed previously, the parallel energy width also corresponds to an effective angular resolution or limit when conducting angular resolved scattering experiments. In cases were the increase in energy width is insignificant, the increase in the positron flux from the trap can be used to decrease the accumulation time for a particular scattering experiment.

While there are two regimes for positron compression in a Surko-style buffer gas trap, the cycling time of the current trap is too fast and the densities too low to apply the plasma compression techniques. The results presented here show that the simple idea of the bounce frequency of the positron in a harmonic well is a sufficient predictor for the optimum frequency regardless of the non-ideal configuration. The fundamental nature of the bounce frequency in a harmonic trap resulting in a decrease in the loss of positrons due to radial diffusion, makes this a powerful tool. It has been selectively used to increase positron flux in the measurements presented in this thesis.

Conclusion

A series of experimental results for positron scattering from fundamental atomic and molecular systems has been presented. The principles of scattering in high magnetic fields have been used to conduct experiments which separate elastic scattering from inelastic scattering so the total forms of these partial scattering cross section can be determined as a function of the incident positron energy. A variety of measurements for an assortment of atomic and molecular targets included: Helium, Neon, Hydrogen (H_2), Water (H_2O), Ammonia (NH_3) and Methane (CH_4).

The elastic differential scattering cross section have been measured at various impact energies for helium and compared to available theoretical calculations. Agreement between theoretical and experimental results are reasonably good at some scattering energies. Below the positronium formation threshold, where theory should be able to provide an 'exact' answer, the experimental results show differences, making the extraction of partial-wave phase shifts problematic. These results show that the benchmarking of positron helium differential scattering will require further improvements to the current experimental techniques.

In the case of molecular hydrogen, at least one theoretical result provides good agreement in the angular dependence, but the a large discrepancy in the absolute magnitude still remains. Unfortunately, at this time, no theoretical results have incorporated nuclear motion, which can have a large effect on the scattering cross section, and will require further development of this difficult scattering problem.

Grand total scattering cross sections have been measured for molecular hydrogen with particular attention paid to scattering energies below 10 eV. The primary reasons for the discrepancies between experimental results was due the difference in the angular acceptance of individual scattering apparatus. Agreement at energies above 10 eV is very good between available theoretical calculations and experiment at the grand total level. However, the multi-centre nature of positron-molecule scattering has not been properly tackled as yet and it is likely that the current discrepancies will narrow with further theoretical work on this complicated scattering problem.

The total inelastic scattering cross section was measured for molecular hydrogen from the threshold for the first electronic excitation to above the double ionisation threshold. General agreement was seen between the available experimental data for electronic excitation and the available results for direct ionisation. The measurement of the total

or integral elastic scattering cross section also provided reasonable agreement with the available theory.

Channel coupling in the form of Wigner Cusps was pursued in the molecular isoelectronic series with the noble gas, Neon: Water (H_2O), Ammonia (NH_3) and Methane (CH_4). No feature was observed at the limit of the sensitivity of the apparatus. While this was likely due to the density of states, the existence of cusps in these systems due to the onset of positronium formation cannot be completely ruled out. While there is a hint of a cusp in molecular hydrogen, it is not centred about the positronium formation threshold as in its isoelectronic atomic counterpart. The measurement of the cross section for excitation of the fundamental vibrational modes have been made for molecular hydrogen and methane, but has yet to be for water and ammonia, which may provide further insight. Additional experimental efforts in the region between 100 meV and 1 eV would provide for the exploration of the effect of the onset of vibrational channels on the elastic scattering channel providing a potentially rich region of exploration of positron-molecule collisions.

A search was conducted for resonances due to the presences of a positron bound to a doubly-excited state of helium. Unfortunately, no feature attributable to a resonance was detected in either the grand total or positronium formation scattering cross sections. An upper bound on the strength of the was determined resonance based on the experimental energy resolution and the statistical uncertainty. If the resonance due to the temporary bound state of a positron bound to an excited state is similar to the comparable temporary negative ion resonance, it is beyond the detectable limit at this time. However, a search in this energy region of the Z_{eff} may provide a measurable signal, but would require modifications to the existing apparatus.

The implementation of a rotating electric field to increase the central density of the positron beam was successful. However, it was at the cost of the parallel energy width in the current configuration. While this decreased the accumulation time for measurement of scattering cross sections at high energy, it provided no aid in the search for narrow features in total and partial scattering cross sections. Further exploration of the many possible operational modes of the trap incorporating a rotating-wall electrode is warranted.

10.1 Future Directions

There are many exciting positron scattering experiments that are enabled by the system described in this thesis. A few of the most relevant are covered here, but this list is not exhaustive.

10.1.1 Fundamental Positron Scattering

This system was originally conceived for measuring absolute positron scattering cross sections and thereby test our theoretical understanding.

Benchmarking the Positron-Helium System

The results for the elastic differential scattering cross section for positron scattering from helium are clearly not at the benchmark level over the range of investigation. The experimental technique used to determine the elastic DCS is sensitive to the percentage scatter. Simply decreasing the target density is a solution, but at the cost of accumulation time. Further improvements in the operation of the RW to increase the central density of the positron beam may allow for measurements at less than 1 % scatter on time scales shorter than a week.

Fundamental Positron-Atom Scattering

Extending the work on Helium to Neon and Argon for elastic differential scattering cross section would be of interest. A study of the elastic DCS's about the positronium formation threshold may shed some light on the puzzle of why there is no trend in the integral elastic cross section as a function of any atomic parameter. Recalling that the cusps are not detectable in the grand total, but are observed in the partial scattering cross section.

A recently commissioned vacuum oven has the potential to provide gaseous alkali and alkali-earth metal targets for scattering experiments. A search for positron binding to Li, Na, Mg, and Ca are of interest due to recent calculations predicting resonance structure due to the existence of the a bound state. It may also be necessary to develop a new scattering apparatus to measure the annihilation rate as this channel has proven the most effective in detecting resonant structure.

Fundamental Positron-Molecule Scattering

A similar investigation of other homonuclear diatomic molecules as was carried out and reported on in this thesis for molecular hydrogen will be of great importance as the theoretical tools to tackle the complexity of the problem continue to develop. Continuing this investigation to other diatomic molecules such as N_2 and O_2 and heteronuclear diatomic molecules such as CO would complement the recent measurements of the total and direction ionisation scattering cross section. However, a new investigation would focus on elastic differential measurements of N_2, in particular, the region about the threshold for excitation of the $a\,^1\Pi_g$ state.

10.1.2 C_{60} Resonance Search

Scattering resonances provide a strict test of the theoretical models used to describe the interaction. The lack of detectable resonances in elastic scattering of positrons from noble gases or from simple diatomic [114] and polyatomic molecules leads to the search in larger molecules. Note that Vibrational Feshbach Resonances (VFR) have been observed in measurements of annihilation of positron on molecules [28]. Recently, large molecules, such as C_{60}, have been used to study confinement resonances [165]. This have lead to a

large amount of theoretical work in trying to explain the resonances satisfactorily. The possibility of positron confinement resonances in C_{60} is tantalising.

There are many theoretical predictions of resonance structure in positron scattering from atoms and molecules that can be found in the literature [14,166,167]. Unfortunately, there has been no evidence to date for scattering resonances in the elastic scattering channel [114, 168], while a large amount of resonance structure has been observed in annihilation channel for large molecules [146].

More than ten years ago, the work of Gianturco and Lucchese predicted resonances in scattering of positrons from C_{60} [166]. They found that positrons could be trapped both outside and inside the C_{60} cage. No experimental work has been conducted to determine if these resonances exist and, if so, which model for positron-C_{60} scattering correctly describes the interaction potential. This is primary due to the difficulty in producing a vapor target of C_{60}. It is also true that the energy width of positron beams regularly used in scattering experiments have only now become narrow enough, due to the advent of the Surko-style trap, to warrant an extended search with the ability to distinguish between the proposed theoretical models.

Theory

In the treatment of a large molecule such as C_{60}, the fixed nuclei approximation is used to decrease the complexity of the scattering problem. It is modeled as a potential scattering problem in which the charge distribution of the molecule is calculated using GAUSSIAN (version 94, in this case). The total interaction potential is written as,

$$V_{tot}(\mathbf{r}_p) = V_S(\mathbf{r}_p) + V_{CP}(\mathbf{r}_p). \tag{10.1}$$

where the correlation potential (CP) is determined by calculating the second-order perturbation expansion [128],

$$V_{CP}(\mathbf{r}_p) = \sum_{l=1}^{\infty} -\frac{\alpha_l}{2r_p^{2l+2}}. \tag{10.2}$$

Two different methods have been used to determine the interaction potential. One being the electron correlation potential (ECP) where the potential is modeled as a homogeneous electron gas [169,170]. The other being the positron correlation potential (PCP) where the potential is generated using density functional theory for an isolated positron interacting with an electron gas [171]. The correlation potential, either ECP or PCP, together with the static potential is used in a single-centre corresponding closed-coupling calculation with the nuclei fixed.

There are two types of resonance discussed in Gianturo and Lucchese [166]. The first resonance is an angular-momentum barrier resonance where the positron is bound outside of the C_{60} cage. The second resonance was at low angular momentum where the positron is trapped inside the C_{60} cage. Both types of resonance are observed for both theoretical descriptions, but require differing amounts of correlation strength. These resonance

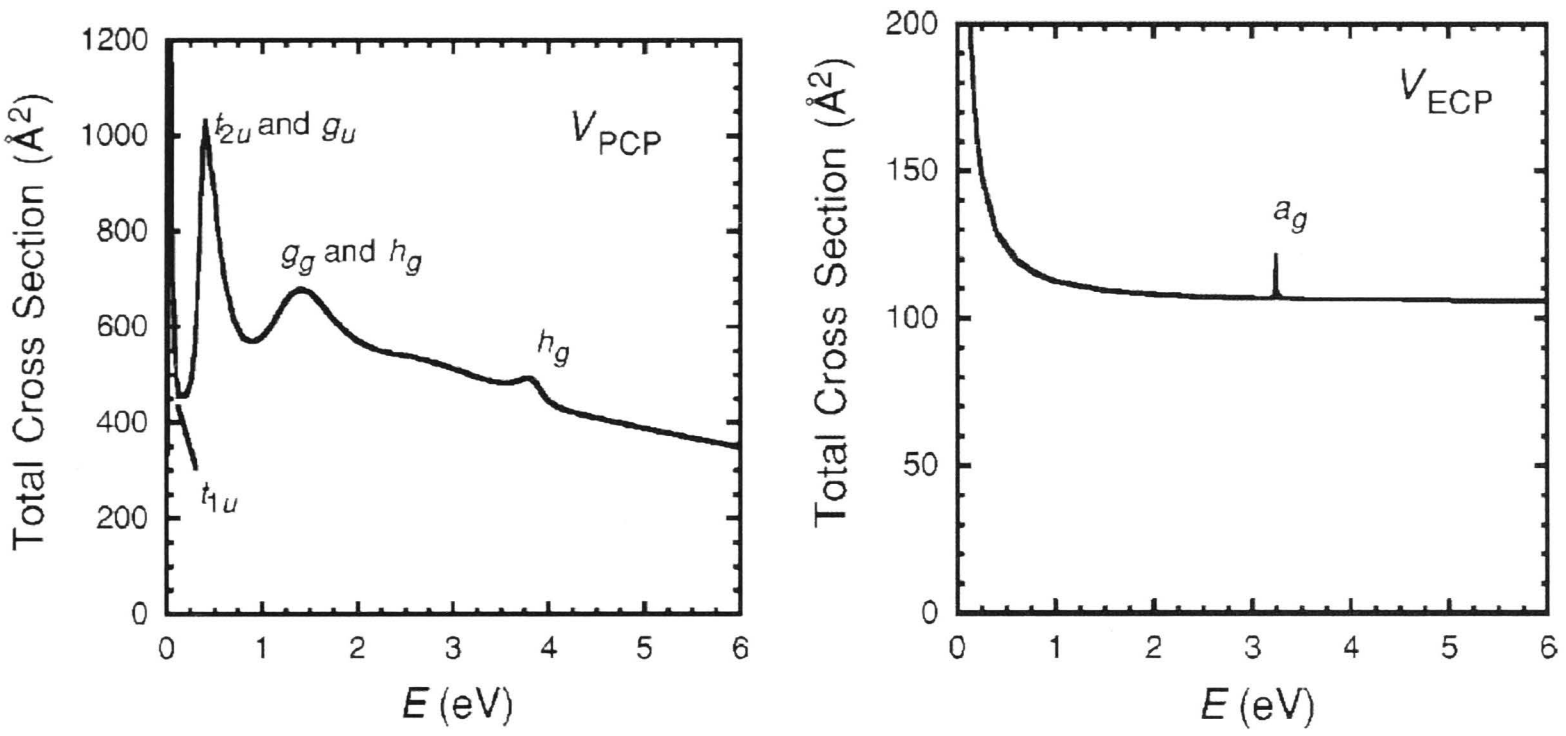

Figure 10.1: Theoretical results of Gianturco and Lucchese: *Left Panel*, Positron Correlation Potential (PCP); *Right Panel*, Electron Correlation Potential (ECP) [166].

manifest in both the total scattering cross section and the elastic differential scattering cross section. The predicted resonance structures in the total scattering cross section appear as symmetric profiles. This is the case for both confinement within the cage and trapping outside of the cage. The sharp structures predicted by both theoretical models provide a signature which is easily verifiable. As discussed in the experimental Chapter 3, the present Surko trap based positron beamline line can provide a beam with an parallel energy width of 60 meV or better. The various resonances predicted by the PCP theory shown in figure 10.1.2 range from 250 and 750 meV FWHM. The theoretical predictions for the elastic differential scattering cross section, using the ECP and PCP appoarches, show significantly different angular dependence. The folded theoretical results of Gianturco and Lucchese [166] are shown in figure 10.2, which are comparable to the measurements able to be made with the current experiment. There is a clear difference between the PCP results at the energy of a predicted resonance and away from the resonance. The comparison for the ECP results are not as clear, although it should be noted that the theoretical results are plotted on a logarithmic scale.

Comparison to Electron Scattering

A series of theoretical results on electron scattering from C_{60} at energies below 100 eV is also present in the literature [172]. These results and the references therein indicate that the GTCS for this system ranges between 100 and 200 Å^2. The measurements of Tanaka *et al.* [173] are the only gas phase results below 100 eV and only cover the region from 1 to 11.5 eV. Previous comparison between positron and electron scattering, (see Chapter 2), would imply that the GTCS for positrons should be lower than the results for electrons.

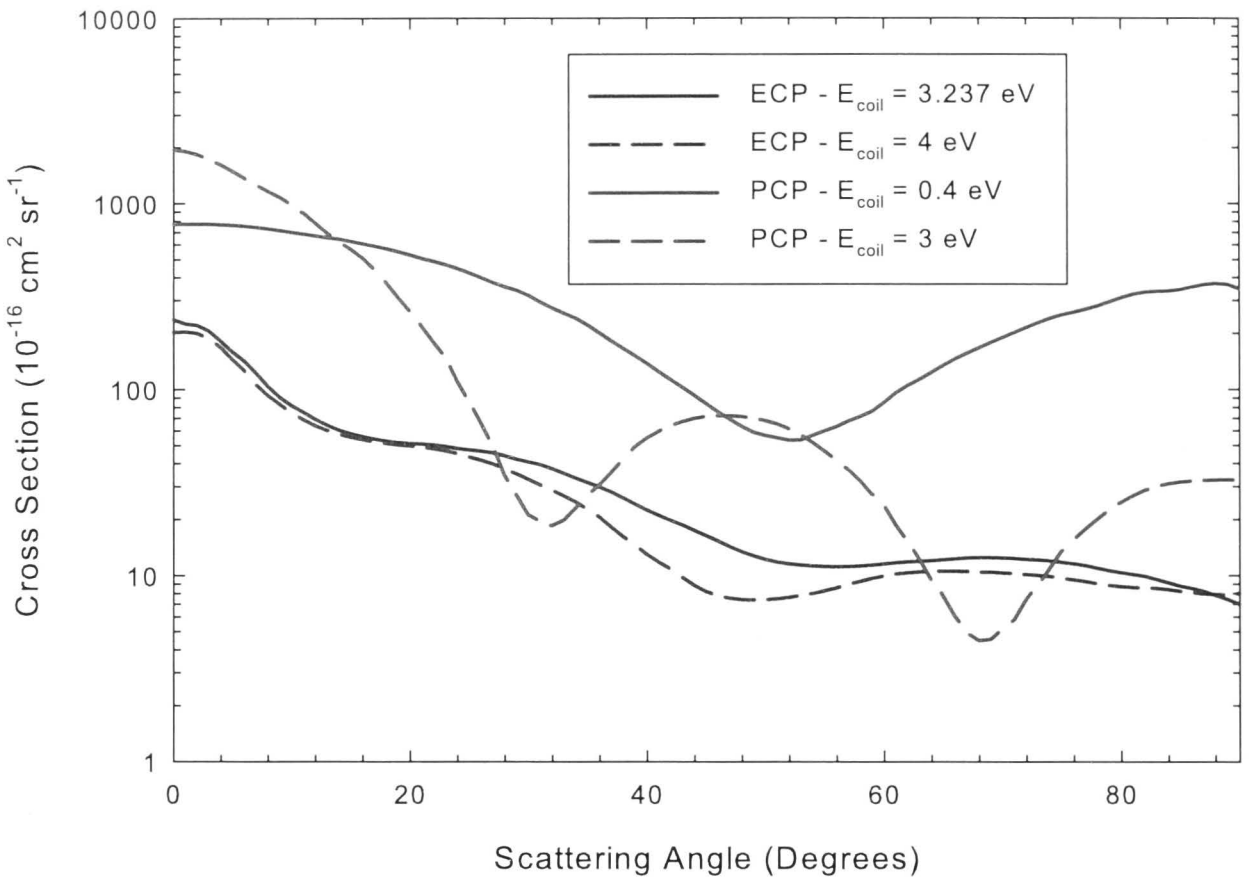

Figure 10.2: Comparison of theoretical results of [166] for differential scattering of positrons on C_{60} which has been folded about 90° to compare with possible experimental results, see text.

Proposed Experiment

The nature of the theoretical description of the scattering problem yields large differences in both the magnitude and shape of the scattering cross section for positrons and electrons at low incident scattering energies. To gain accurate results using this experimental approach, the determination of the density of the target vapor is difficult in a vacuum oven and is critically dependent on accurate vapor pressure curves. However, the energy dependence of both the grand total scattering cross section and the elastic differential scattering cross section are markedly different between the ECP and PCP theories allowing for a comparison of the relative shape of the cross sections rather than absolute magnitude.

The ionisation potential of C_{60} is approximately 7.6 eV [154]. This puts the positronium formation threshold at 800 meV allowing the methods discussed in the thesis to be used without modification for the determination of the grand total scattering and positronium formation cross section.

Leach *et al.* [174] reported a number of vibrational excitations from $\sim$ 160 meV to 560 meV and electronic excitations beginning at $\sim$ 3.04 eV (observed, $1\,^1T_{1u}$). The vibrational excitations are too tightly spaced to separate even with the highest energy resolution positron beam (25 meV parallel energy width), but a the sum of all vibrational excitations could be measured. The total quasi-elastic and inelastic scattering cross sections could also be measured using the techniques described in Chapter 4.

The experimental apparatus is usually run such that the total amount of scatter is 10%. This defines the density required for a given scattering cross section at a given

energy by the Beer-Lambert Law. The vapor pressure curve for C_{60} is,

$$log\left(\frac{p}{kPa}\right) = (8.28 \pm 0.02) - \frac{9154 \pm 150}{T}, \tag{10.3}$$

from Piacente *et al.* [175]. To obtain a density of 10^{12} per cm^2 for a scattering cross section of 100 Å, a temperature of 441 K or 168 degrees C is required. This is well within the operational range of the vacuum oven that has been constructed for use on the apparatus described in this thesis.

The search for scattering resonances often takes a significant amount of accumulation time due to the cross sections which are small. While the strength of the predicted resonances is large, the two theories predict different resonance energies requiring a search of as a function of energy. A calculation of how much target mass will be required for the measurement is needed. This can be calculated using the following equation for the mass flow between two volumes,

$$G = P_1^{\frac{3}{2}}\left(1 - \frac{P_2}{P_1}\right) r^2 \sqrt{\frac{2\pi}{RT}}, \tag{10.4}$$

where r is the radius of the aperture connecting the two volumes, R is the idea gas constant and T is the temperature [176]. Assuming a background pressure outside of the hot cell of 1 μTorr and a pressure in the hot cell of 30 μTorr, the mass flow rate is $5x10^{-8}$ grams per second. Thus one gram would last over 200 days of operation and 200 mg would last $\sim$ 45 days making the search for resonances in C_{60} possible.

Conclusion

An experiment based on the range of available theory and experiment in literature has be outlined using existing capabilities. The dangers posed by vaporising a carbon target in a vacuum system may seem too great to the seasoned experimentalist, but the demonstration of this capability is of great importance for the future of positron scattering in preparation for the study of metal atomic targets. It also is of fundamental importance as the nature of the two theories used are very different and no subsequent theory has predicted similar structure, suggesting the likelihood of their existence tentative at best. A thorough investigation of low-energy positron scattering from C_{60} would yield useful information both in the grand total scattering cross section, elastic differential scattering cross section and the operation of a vacuum oven.

Bibliography

[1] Walter E Kauppila and Talbert S Stein. Advances in Atomic and Molecular Physics. volume Volume 26, chapter Comparison, pages 1–50. Academic Press, 1989.

[2] D P Dewangan. On higher order Born approximations in atomic scattering calculations. *Journal of Physics B: Atomic and Molecular Physics*, 13(19):L595, 1980.

[3] T. Murphy and C. Surko. Positron trapping in an electrostatic well by inelastic collisions with nitrogen molecules. *Physical Review A*, 46(9):5696–5705, 1992.

[4] A. P. Mills and E. M. Gullikson. Solid neon moderator for producing slow positrons. *Applied Physics Letters*, 49(17):1121, 1986.

[5] P. Caradonna, A. Jones, C. Makochekanwa, D. S. Slaughter, J. P. Sullivan, S. J. Buckman, I. Bray, and D. Fursa. High-resolution positron scattering from helium: Grand total and positronium-formation cross sections. *Physical Review A*, 80(3):032710, 2009.

[6] R. Utamuratov, A. S. Kadyrov, D. V. Fursa, I. Bray, and A. T. Stelbovics. Multiconfigurational two-centre convergent close-coupling approach to positron scattering on helium. *Journal of Physics B: Atomic, Molecular and Optical Physics*, 43(12):125203, 2010.

[7] A. C. L. Jones, C. Makochekanwa, P. Caradonna, D. S. Slaughter, J. R. Machacek, R. P. McEachran, J. P. Sullivan, S. J. Buckman, A. D. Stauffer, I. Bray, and D. V. Fursa. Positron scattering from neon and argon. *Physical Review A*, 83(3):032701, 2011.

[8] C. Makochekanwa, J. Machacek, A. Jones, P. Caradonna, D. Slaughter, R. McEachran, J. Sullivan, S. Buckman, S. Bellm, B. Lohmann, D. Fursa, I. Bray, D.W. Mueller, A. Stauffer, and M. Hoshino. Low-energy positron interactions with krypton. *Physical Review A*, 83(3), 2011.

[9] J. R. Machacek, C. Makochekanwa, A. C. L. Jones, P. Caradonna, D. S. Slaughter, R. P. McEachran, J. P. Sullivan, S. J. Buckman, S. Bellm, B. Lohmann, D. V. Fursa, I. Bray, D. W. Mueller, and A. D. Stauffer. Low-energy positron interactions with xenon. *New Journal of Physics*, 13(12):125004, 2011.

[10] R P McEachran and A D Stauffer. Positronium formation in the noble gases. *Journal of Physics B: Atomic, Molecular and Optical Physics*, 46(7):75203, 2013.

[11] J Mitroy, M W J Bromley, and G Ryzhikh. Positron binding to a model alkali atom. *Journal of Physics B: Atomic, Molecular and Optical Physics*, 32(9):2203–2214, 1999.

[12] G F Gribakin and J Ludlow. Many-body theory of positron-atom interactions. *Physical Review A*, 70(3):32720, 2004.

[13] Dario Bressanini. Positron Binding to Lithium Excited States. *Physical Review Letters*, 109(22):223401, 2012.

[14] M. W. J. Bromley, J. Mitroy, and K. Varga. Positron Attachment to the He Doubly Excited States. *Physical Review Letters*, 109(6):063201, 2012.

[15] David Reid, William Klann, and J. Wadehra. Scattering of low- to intermediate-energy positrons from molecular hydrogen. *Physical Review A*, 70(6):062714, 2004.

[16] Mark C. Zammit, Dmitry V. Fursa, and Igor Bray. Convergent-close-coupling formalism for positron scattering from molecules. *Physical Review A*, 87(2):020701, 2013.

[17] F. Arretche, R.F. da Costa, S. dA. Sanchez, A.N.S. Hisi, E.M. de Oliveira, M.T. do N. Varella, and M.A.P. Lima. Similarities and differences in emolecule scattering: Applications of the Schwinger multichannel method. *Nuclear Instruments and Methods in Physics Research Section B: Beam Interactions with Materials and Atoms*, 247(1):13–19, 2006.

[18] G Danby and J Tennyson. Differential cross sections for elastic positron-H_2 collisions using the R-matrix method. *Journal of Physics B: Atomic, Molecular and Optical Physics*, 23(6):1005–1016, 1990.

[19] M Eyb and H Hofmann. Elastic electron-alkali atom scattering near the first inelastic threshold. *Journal of Physics B: Atomic and Molecular Physics*, 8(7):1095, 1975.

[20] A. C. L. Jones, P. Caradonna, C. Makochekanwa, D. S. Slaughter, R. P. McEachran, J. R. Machacek, J. P. Sullivan, and S. J. Buckman. Observation of Threshold Effects in Positron Scattering from the Noble Gases. *Physical Review Letters*, 105(7):073201, 2010.

[21] M. Charlton and J.W. Humberston. *Positron Physics*. Cambridge University Press, Cambridge, 2nd edition, 2005.

[22] C M Surko, G F Gribakin, and S J Buckman. Low-energy positron interactions with atoms and molecules. *Journal of Physics B: Atomic, Molecular and Optical Physics*, 38(6):R57–R126, 2005.

[23] Clifford M Surko and F. A. Gianturco, editors. *New Directions in Antimatter Chemistry and Physics*. Kluwer Academic Publishers, Netherlands, 2001.

[24] T.C Griffith and G.R Heyland. Experimental aspects of the study of the interaction of low-energy positrons with gases. *Physics Reports*, 39(3):169–277, 1978.

[25] P A M Dirac. A Theory of Electrons and Protons. *Proceedings of the Royal Society of London. Series A*, 126(801):360–365, 1930.

[26] P A Fraser. Positrons and Positronium in Gases. volume Volume 4, pages 63–107. Academic Press, 1968.

[27] G F Gribakin. Mechanisms of positron annihilation on molecules. *Physical Review A*, 61(2):22720, 2000.

[28] G F Gribakin, J A Young, and C M Surko. Positron-molecule interactions: Resonant attachment, annihilation, and bound states. *Reviews of Modern Physics*, 82(3):2557–2607, 2010.

[29] A Ore and J L Powell. Three-Photon Annihilation of an Electron-Positron Pair. *Physical Review*, 75(11):1696–1699, 1949.

[30] Paul C. Cross E. Bright Wilson, Jr., J. C. Decius. *Molecular Vibrations*. Dover, New York, 1980.

[31] G Herzberg. *Molecular Spectra and Molecular Structure I. Spectra of Diatomic Molecules*. Van Nostrand Reinhold Company, New York, 1950.

[32] W. Kauppila, T. Stein, J. Smart, M. Dababneh, Y. Ho, J. Downing, and V. Pol. Measurements of total scattering cross sections for intermediate-energy positrons and electrons colliding with helium, neon, and argon. *Physical Review A*, 24(2):725–742, 1981.

[33] T S Stein, W E Kauppila, V Pol, J H Smart, and G Jesion. Measurements of total scattering cross sections for low-energy positrons and electrons colliding with helium and neon atoms. *Physical Review A*, 17(5):1600–1608, 1978.

[34] J. P. Sullivan, J.P. Marler, S. J. Gilbert, S. J. Buckman, and C. M. Surko. Excitation of Electronic States of Ar, H_2, and N_2 by Positron Impact. *Physical Review Letters*, 87(7):073201, 2001.

[35] Stephen J Buckman and Charles W Clark. Atomic negative-ion resonances. *Reviews of Modern Physics*, 66(2):539–655, 1994.

[36] N F Lane. The theory of electron-molecule collisions. *Reviews of Modern Physics*, 52(1):29–119, 1980.

[37] J P Marler and C M Surko. Systematic comparison of positron- and electron-impact excitation of the ν_3 vibrational mode of CF_4. *Phys. Rev. A*, 72(6):62702, 2005.

[38] J. P. Sullivan, S. J. Gilbert, J. P. Marler, R. G. Greaves, S. J. Buckman, and C. M. Surko. Positron scattering from atoms and molecules using a magnetized beam. *Physical Review A*, 66(4):042708, 2002.

[39] J R Danielson, J J Gosselin, and C M Surko. Dipole Enhancement of Positron Binding to Molecules. *Physical Review Letters*, 104(23):233201, 2010.

[40] G F Gribakin and C M R Lee. Positron Annihilation in Molecules by Capture into Vibrational Feshbach Resonances of Infrared-Active Modes. *Physical Review Letters*, 97(19):193201, 2006.

[41] J P Marler, J P Sullivan, and C M Surko. Ionization and positronium formation in noble gases. *Physical Review A*, 71(2):22701, 2005.

[42] J P Marler and C M Surko. Positron-impact ionization, positronium formation, and electronic excitation cross sections for diatomic molecules. *Physical Review A*, 72(6):62713, 2005.

[43] Albert Messiah. *Quantum Mechanics*. Dover, New York, 1^{st} edition, 1999.

[44] Aaron Temkin. Polarization and Exchange Effects in the Scattering of Electrons from Atoms with Application to Oxygen. *Physical Review*, 107(4):1004–1012, 1957.

[45] M. D. Lloyd and M. R. C. McDowell. An application of the polarized-orbital approximation to electron impact excitation of atomic hydrogen. *Journal of Physics B: Atomic and Molecular Physics*, 2(12):1313, 1969.

[46] R P McEachran, A G Ryman, A D Stauffer, and D L Morgan. Positron scattering from noble gases. *Journal of Physics B: Atomic and Molecular Physics*, 10(4):663, 1977.

[47] S. Chen, R. P. McEachran, and A. D. Stauffer. Ab initio optical potentials for elastic electron and positron scattering from the heavy noble gases. *Journal of Physics B: Atomic, Molecular and Optical Physics*, 41(2):25201, 2008.

[48] Igor Bray and Andris T Stelbovics. Convergent close-coupling calculations of electron-hydrogen scattering. *Physical Review A*, 46(11):6995–7011, 1992.

[49] Igor Bray. Convergent close-coupling method for the calculation of electron scattering on hydrogen-like targets. *Phys. Rev. A*, 49(2):1066–1082, 1994.

[50] H. Wu, I. Bray, D. V. Fursa, and A. T. Stelbovics. Low-energy positronhelium convergent close coupling calculations. *Journal of Physics B: Atomic, Molecular and Optical Physics*, 37(1):L1, 2004.

[51] K Varga and Y Suzuki. Precise solution of few-body problems with the stochastic variational method on a correlated Gaussian basis. *Physical Review C*, 52(6):2885–2905, 1995.

[52] Frank E Harris. Expansion Approach to Scattering. *Physical Review Letters*, 19(4):173–175, 1967.

[53] J. Mitroy, M. W. J. Bromley, and G. G. Ryzhikh. Positronic Atoms. In C. M. Surko and F. A. Gianturco, editors, *New Directions in Antimatter Physics and Chemisty*, pages 199–221. Kluwer Academic Publishers, Netherlands, 2001.

[54] G. G . Ryzhikh, J. Mitroy, and K. Varga. The structure of exotic atoms containing positrons and positronium. *Journal of Physics B: Atomic, Molecular and Optical Physics*, 31(17):3965, 1998.

[55] J Y Zhang and J Mitroy. Stochastic variational method for elastic scattering. *Physical Review A*, 78(1):12703, 2008.

[56] A Hibbert. Developments in atomic structure calculations. *Reports on Progress in Physics*, 38(11):1217, 1975.

[57] V A Dzuba, V V Flambaum, G F Gribakin, and C Harabati. Calculation of the positron bound state with the copper atom. *Physical Review A*, 60(5):3641–3647, 1999.

[58] M W J Bromley, J Mitroy, and G G Ryzhikh. Configuration interaction calculations of positronic atoms and ions. *Nuclear Instruments and Methods in Physics Research Section B: Beam Interactions with Materials and Atoms*, 171(12):47–59, 2000.

[59] V A Dzuba, V V Flambaum, and G F Gribakin. Detecting Positron-Atom Bound States through Resonant Annihilation. *Phys. Rev. Lett.*, 105(20):203401, 2010.

[60] J. Tennyson. Electronmolecule collision calculations using the R-matrix method. *Physics Reports*, 491(23):29–76, 2010.

[61] J. M. Carr, P. G. Galiatsatos, J. D. Gorfinkiel, A. G. Harvey, M. A. Lysaght, D. Madden, Z. Mašín, M. Plummer, J. Tennyson, and H. N. Varambhia. UKRmol: a low-energy electron- and positron-molecule scattering suite. *The European Physical Journal D*, 66(3):58, 2012.

[62] P G Burke. *R-Matrix Theory of Atomic Collisions: Application to Atomic, Molecular and Optical Processes*. Springer Series on Atomic. Springer, Berlin, 2011.

[63] R. Zhang, K. L. Baluja, J. Franz, and J. Tennyson. Positron collisions with molecular hydrogen: cross sections and annihilation parameters calculated using the R -matrix with pseudo-states method. *Journal of Physics B: Atomic, Molecular and Optical Physics*, 44(3):35203, 2011.

[64] Kazuo Takatsuka and Vincent McKoy. Extension of the Schwinger variational principle beyond the static-exchange approximation. *Physical Review A*, 24(5):2473–2480, 1981.

[65] José S E Germano and Marco A P Lima. Schwinger multichannel method for positron-molecule scattering. *Physical Review A*, 47(5):3976–3982, 1993.

[66] Jorge Lino, José Germano, Euclimar da Silva, and Marco Lima. Elastic cross sections and annihilation parameter for e^+-H_2 scattering using the Schwinger multichannel method. *Physical Review A*, 58(5):3502–3506, 1998.

[67] D. D. Reid and J. M. Wadehra. A quasifree model for the absorption effects in positron scattering by atoms. *Journal of Physics B: Atomic, Molecular and Optical Physics*, 30(9):2318, 1997.

[68] David D Reid and J M Wadehra. Intermediate- to high-energy positrons scattered by alkali-metal atoms. *Physical Review A*, 57(4):2583–2589, 1998.

[69] A C L Jones. *Low Energy Positron Interactions with the Rare Gases*. PhD thesis, The Australian National University, 2011.

[70] Peter Caradonna. *Experimental Studies of Positron-Helium Interactions at Low Energies*. PhD thesis, The Australian National University, 2011.

[71] Peter J Schultz and K G Lynn. Interaction of positron beams with surfaces, thin films, and interfaces. *Reviews of Modern Physics*, 60(3):701–779, 1988.

[72] K G Lynn, B Nielsen, and J H Quateman. Development and use of a thin-film transmission positron moderator. *Applied Physics Letters*, 47(3):239–240, 1985.

[73] B. L. Brown, W. S. Crane, and A. P. Jr. Mills. Generation of highly monochromatic positrons using cold moderators. *Applied Physics Letters*, 48(11):739–741, 1986.

[74] S. J. Gilbert, C. Kurz, R. G. Greaves, and C. M. Surko. Creation of a monoenergetic pulsed positron beam. *Applied Physics Letters*, 70(15):1944, 1997.

[75] S. J. Gilbert, R. G. Greaves, and C. M. Surko. Positron Scattering from Atoms and Molecules at Low Energies. *Physical Review Letters*, 82(25):5032–5035, 1999.

[76] J P Sullivan, A Jones, P Caradonna, C Makochekanwa, and S J Buckman. A positron trap and beam apparatus for atomic and molecular scattering experiments. *Review of Scientific Instruments*, 79(11):113105, 2008.

[77] First Point Scientific, Inc.

[78] iThemba Labs.

[79] G. R. Massoumi, N. Hozhabri, W. N. Lennard, P. J. Schultz, S. F. Baert, H. H. Jorch, and A. H. Weiss. Rare gas moderated electrostatic positron beam. *Review of Scientific Instruments*, 62(6):1460, 1991.

[80] R.G. Greaves and C.M. Surko. Positron trapping and the creation of high-quality trap-based positron beams. *Nuclear Instruments and Methods in Physics Research Section B: Beam Interactions with Materials and Atoms*, 192(1-2):90–96, 2002.

[81] S. J. Buckman, R. J. Gulley, M. Moghbelalhossein, and S. J. Bennett. Spatial profiles of effusive molecular beams and their dependence on gas species. *Measurement Science and Technology*, 4(10):1143, 1993.

[82] Ian Humphrey. A Monte Carlo study of pressure dependent effects in the electron impact excitation of the He 3 ^{1}P state. *Measurement Science and Technology*, 11(8):1193–1207, 2000.

[83] B P Mathur, J E Field, and S O Colgate. Calculations of effusive-flow patterns. III. Scattering chambers with thin circular apertures. *Physical Review A*, 11(3):830–833, 1975.

[84] J P Sullivan, C Makochekanwa, A Jones, P Caradonna, and S J Buckman. High-resolution, low-energy positron scattering from helium: measurements of the total scattering cross section. *Journal of Physics B: Atomic, Molecular and Optical Physics*, 41(8):81001, 2008.

[85] S. Tang and C. M. Surko. Angular dependence of positronium formation in molecular hydrogen. *Physical Review A*, 47(2):R743–R746, 1993.

[86] S. J. Gilbert, J. P. Sullivan, R. G. Greaves, and C. M. Surko. Low-energy positron scattering from atoms and molecules using positron accumulation techniques. *Nuclear Instruments and Methods in Physics Research Section B: Beam Interactions with Materials and Atoms*, 171(12):81–95, 2000.

[87] Peter Caradonna, James P. Sullivan, Adric Jones, Casten Makochekanwa, Daniel Slaughter, Dennis W. Mueller, and Stephen J. Buckman. Excitation of the n=2 states of helium by positron impact. *Physical Review A*, 80(6):060701, 2009.

[88] J P Sullivan, S J Gilbert, J P Marler, L D Barnes, S J Buckman, and C M Surko. Low energy positron scattering and annihilation studies using a high resolution trap-based beam. *Nuclear Instruments and Methods in Physics Research Section B: Beam Interactions with Materials and Atoms*, 192(12):3–16, 2002.

[89] T Takaishi and Y Sensui. Thermal transpiration effect of hydrogen, rare gases and methane. *Transactions of the Faraday Society*, 59(1):2503–2514, 1963.

[90] J Kestin and W Leidenfrost. An absolute determination of the viscosity of eleven gases over a range of pressures. *Physica*, 25(712):1033–1062, 1959.

[91] J P Sullivan, C Makochekanwa, A Jones, P Caradonna, D S Slaughter, J Machacek, R P McEachran, D W Mueller, and S J Buckman. Forward angle scattering effects

in the measurement of total cross sections for positron scattering. *Journal of Physics B: Atomic, Molecular and Optical Physics*, 44(3):035201, 2011.

[92] Casten Makochekanwa, Ana Bankovic, Wade Tattersall, Adric Jones, Peter Caradonna, Daniel S Slaughter, Kate Nixon, Michael J Brunger, Zoran Petrovic, James P Sullivan, and Stephen J Buckman. Total and positronium formation cross sections for positron scattering from H_2O and HCOOH. *New Journal of Physics*, 11(10):103036, 2009.

[93] Philip R. Bevington and Keith D. Robinson. *Data Reduction and Error Analysis for the Physical Sciences*. McGraw-Hill, New York, 3rd edition, 2003.

[94] K L Baluja and Ashok Jain. Positron scattering from rare gases (He, Ne, Ar, Kr, Xe, and Rn): Total cross sections at intermediate and high energies. *Physical Review A*, 46(3):1279–1290, 1992.

[95] C.P. Campbell, Mary T. McAlinden, Ann A. Kernoghan, and H.R.J. Walters. Positron collisions with one- and two-electron atoms. *Nuclear Instruments and Methods in Physics Research Section B: Beam Interactions with Materials and Atoms*, 143(1-2):41–56, 1998.

[96] T Mizogawa, Y Nakayama, T Kawaratani, and M Tosaki. Precise measurements of positron-helium total cross sections from 0.6 to 22 eV. *Physical Review A*, 31(4):2171–2179, 1985.

[97] Stephen J Buckman and James P Sullivan. Benchmark measurements and theory for electron(positron)molecule(atom) scattering. *Nuclear Instruments and Methods in Physics Research Section B: Beam Interactions with Materials and Atoms*, 247(1):5–12, 2006.

[98] P Van Reeth and J W Humberston. Elastic scattering and positronium formation in low-energy positron-helium collisions. *Journal of Physics B: Atomic, Molecular and Optical Physics*, 32(15):3651, 1999.

[99] L Boesten and H Tanaka. Rational function fits to the nonresonant elastic differential cross sections (DCS) for e^+-He collisions, 0° to 180°, 0.1 to 1000 eV. *Atomic Data and Nuclear Data Tables*, 52(1):25–42, 1992.

[100] R. Utamuratov, A. S. Kadyrov, D. V. Fursa, and I. Bray. A two-centre convergent close-coupling approach to positron helium collisions. *Journal of Physics B: Atomic, Molecular and Optical Physics*, 43(3):31001, 2010.

[101] P. Coleman and J. McNutt. Measurement of Differential Cross Sections for the Elastic Scattering of Positrons by Argon Atoms. *Physical Review Letters*, 42(17):1130–1133, 1979.

[102] R.L. Chaplin, L.M. Diana, and D.L. Brooks. Absolute differential and total cross sections for the scattering of positrons from helium. *Nuclear Instruments and Methods in Physics Research Section B: Beam Interactions with Materials and Atoms*, 56-57:595–598, 1991.

[103] R. P. McEachran. Private Communication, 2012.

[104] I. Bray. Private Communication, 2010.

[105] P VanReeth. Private Communication, 2012.

[106] R. Utamuratov. Private Communication, 2010.

[107] D G Thompson. The Elastic Scattering of Slow Electrons by Neon and Argon. *Proceedings of the Royal Society of London. Series A. Mathematical and Physical Sciences*, 294(1437):160–174, 1966.

[108] D F Register, S Trajmar, and S K Srivastava. Absolute elastic differential electron scattering cross sections for He: A proposed calibration standard from 5 to 200 eV. *Physical Review A*, 21(4):1134–1151, 1980.

[109] M. K. Ali and P. A. Fraser. The contribution of long-range forces to low-energy phaseshifts. *Journal of Physics B: Atomic and Molecular Physics*, 10(15):3091, 1977.

[110] J Mitroy, M W J Bromley, and G G Ryzhikh. Positron and positronium binding to atoms. *Journal of Physics B: Atomic, Molecular and Optical Physics*, 35(13):R81, 2002.

[111] L. Barnes, S. J. Gilbert, and C. M. Surko. Energy-resolved positron annihilation for molecules. *Physical Review A*, 67(3):032706, 2003.

[112] Dieter Fromme, Georg Kruse, Wilhelm Raith, and Günther Sinapius. Partial-Cross-Section Measurements for Ionization of Helium by Positron Impact. *Physical Review Letters*, 57(24):3031–3034, 1986.

[113] Talbert S Stein and Walter E Kauppila. PositronGas Scattering Experiments. volume Volume 18, pages 53–96. Academic Press, 1982.

[114] James P Sullivan, Steven J Gilbert, Stephen J Buckman, and Clifford M Surko. Search for resonances in the scattering of low-energy positrons from atoms and molecules. *Journal of Physics B: Atomic, Molecular and Optical Physics*, 34(15):L467, 2001.

[115] J. Mitroy. Private Communication, 2012.

[116] M W J Bromley Mitroy and J. Excited, bound and resonant positron-atom systems. *Journal of Physics: Conference Series*, 199(1):12011, 2010.

[117] J J Quéméner, C Paquet, and P Marmet. Natural Line Shapes Resolved in the Ionization Yield of He^+ below the n=2 Threshold. *Phys. Rev. A*, 4(2):494–498, 1971.

[118] J R Danielson, A C L Jones, M R Natisin, and C M Surko. Comparisons of Positron and Electron Binding to Molecules. *Physical Review Letters*, 109(11):113201, 2012.

[119] J. P. Sullivan, S. J. Gilbert, and C. M. Surko. Excitation of Molecular Vibrations by Positron Impact. *Physical Review Letters*, 86(8):1494–1497, 2001.

[120] P. G. Coleman, T. C. Griffith, and G. R. Heyland. Measurement of total scattering cross-sections for positrons of energies 2 400 eV on molecular gases: H_2, D_2, N_2, CO. *Applied Physics*, 4(1):89–90, 1974.

[121] K. Hoffman, M. Dababneh, Y.-F. Hsieh, W. Kauppila, V. Pol, J. Smart, and T. Stein. Total-cross-section measurements for positrons and electrons colliding with H_2, N_2, and CO_2. *Physical Review A*, 25(3):1393–1403, 1982.

[122] Antonio Zecca, Luca Chiari, A Sarkar, Kate L Nixon, and Michael J Brunger. Total cross sections for positron scattering from H_2 at low energies. *Phys. Rev. A*, 80(3):32702, 2009.

[123] M Charlton, T C Griffith, G R Heyland, and G L Wright. Total scattering cross sections for low-energy positrons in the molecular gases H_2, N_2, CO_2, O_2 and CH_4. *Journal of Physics B: Atomic and Molecular Physics*, 16(2):323, 1983.

[124] S Zhou, H Li, W E Kauppila, C K Kwan, and T S Stein. Measurements of total and positronium formation cross sections for positrons and electrons scattered by hydrogen atoms and molecules. *Phys. Rev. A*, 55(1):361–368, 1997.

[125] T L Gibson. Low-energy positron-H_2 collisions in the distributed positron model. *Journal of Physics B: Atomic, Molecular and Optical Physics*, 25(6):1321–1336, 1992.

[126] E A G Armour, D J Baker, and M Plummer. The theoretical treatment of low-energy e^+-H_2 scattering using the Kohn variational method. *Journal of Physics B: Atomic, Molecular and Optical Physics*, 23(17):3057, 1990.

[127] T. Mukherjee and N. K. Sarkar. Ro-vibrational close coupling study of positron-hydrogen molecule scattering using the parameter-free model correlation polarization potential. *Journal of Physics B: Atomic, Molecular and Optical Physics*, 41(12):125201, 2008.

[128] F A Gianturco, P Paioletti, and J A Rodriguez-Ruiz. Polarisation potentials for positron-molecule scattering processes. *Zeitschrift für Physik D: Atoms, Molecules and Clusters*, 36(1):51–63, 1996.

[129] W. Tenfen, K. T. Mazon, S. E. Michelin, and F. Arretche. Low-energy elastic positron cross sections for H_2 and N_2 using an ab initio target polarization. *Physical Review A*, 86(4):042706, 2012.

[130] L. Chiari, P. Palihawadana, J. R. Machacek, C. Makochekanwa, G. Garcia, F. Blanco, R. P. McEachran, M. J. Brunger, S. J. Buckman, and J. P. Sullivan. Experimental and theoretical cross sections for positron collisions with 3-hydroxy-tetrahydrofuran. *The Journal of Chemical Physics*, 138(7):074302, 2013.

[131] L. Chiari, E. Anderson, W. Tattersall, J. R. Machacek, P. Palihawadana, C. Makochekanwa, J. P. Sullivan, G. Garcia, F. Blanco, R. P. McEachran, M. J. Brunger, and S. J. Buckman. Total, elastic, and inelastic cross sections for positron and electron collisions with tetrahydrofuran. *The Journal of Chemical Physics*, 138(7):074301, 2013.

[132] D Fromme, G Kruse, W Raith, and G Sinapius. Ionisation of molecular hydrogen by positrons. *Journal of Physics B: Atomic, Molecular and Optical Physics*, 21(10):L261, 1988.

[133] L S Fornari, L M Diana, and P G Coleman. Positronium Formation in Collisions of Positrons with He, Ar, and H_2. *Phys. Rev. Lett.*, 51(25):2276–2279, 1983.

[134] P K Biswas and A S Ghosh. Study of positronium formation in positron - hydrogen molecule scattering. *Journal of Physics B: Atomic, Molecular and Optical Physics*, 30(4):983–989, 1997.

[135] P K Biswas, J S E Germano, and T Frederico. Positron hydrogen molecule scattering considering the positronium-formation channel. *Journal of Physics B: Atomic, Molecular and Optical Physics*, 35(18):L409–L418, 2002.

[136] R I Campeanu, J W Darewych, and A D Stauffer. Positron-impact ionization of molecular hydrogen. *Journal of Physics B: Atomic, Molecular and Optical Physics*, 30(21):5033–5041, 1997.

[137] J Moxom, G Laricchia, and M Charlton. Ionization of He, Ar and H_2 by position impact at intermediate energies. *Journal of Physics B: Atomic, Molecular and Optical Physics*, 28(7):1331–1347, 1995.

[138] J.-Y. Zhang and J. Mitroy. Positron Scattering and Annihilation from the Hydrogen Molecule at Zero Energy. *Physical Review Letters*, 103(22):223202, 2009.

[139] Eugene Wigner. On the Behavior of Cross Sections Near Thresholds. *Physical Review*, 73(9):1002–1009, 1948.

[140] R. I. Campeanu, D. Fromme, G. Kruse, R. P. McEachran, L. A. Parcell, W. Raith, G. Sinapius, and A. D. Stauffer. Partitioning of the positron-helium total scattering

cross section. *Journal of Physics B: Atomic and Molecular Physics*, 20(14):3557, 1987.

[141] P. G. Coleman, K. A. Johnston, A. M. G. Cox, A. Goodyear, and M. Charlton. Elastic positron-helium scattering near the positronium formation threshold. *Journal of Physics B: Atomic, Molecular and Optical Physics*, 25(22):L585, 1992.

[142] W E Meyerhof and G Laricchia. Threshold and channel-coupling effects in positron elastic scattering from noble gases. *Journal of Physics B: Atomic, Molecular and Optical Physics*, 30(9):2221–2238, 1997.

[143] P Van Reeth and J W Humberston. A significant feature in the total cross section for positron-helium scattering at the positronium formation threshold. *Journal of Physics B: Atomic, Molecular and Optical Physics*, 32(5):L103, 1999.

[144] G P Karwasz, D Pliszka, A Zecca, and R S Brusa. Positron scattering in helium: Virtual-positronium resonances. *Nuclear Instruments and Methods in Physics Research Section B: Beam Interactions with Materials and Atoms*, 240(3):666–674, 2005.

[145] Roger Newton. Threshold Properties of Scattering and Reaction Cross Sections. *Physical Review*, 114(6):1611–1618, 1959.

[146] D.B. Jones, S.M. Bellm, P. Limão Vieira, and M.J. Brunger. Low-energy electron scattering from pyrimidine: Similarities and differences with benzene. *Chemical Physics Letters*, 535:30–34, 2012.

[147] O Sueoka, S Mori, and Y Katayama. Total cross sections for positron and electron collisions with NH_3 and H_2O molecules. *Journal of Physics B: Atomic and Molecular Physics*, 20(13):3237–3246, 1987.

[148] Antonio Zecca, Luca Chiari, Emanuele Trainotti, and Michael J Brunger. Very low-energy total cross sections and the experimental scattering length for the positron-xenon system. *Journal of Physics B: Atomic, Molecular and Optical Physics*, 45(8):085203, 2012.

[149] M S Dababneh, Y.-F. Hsieh, W E Kauppila, C K Kwan, Steven J Smith, T S Stein, and M N Uddin. Total-cross-section measurements for positron and electron scattering by O_2, CH_4, and SF_6. *Phys. Rev. A*, 38(3):1207–1216, 1988.

[150] O Sueoka and S Mori. Total cross sections for low and intermediate energy positrons and electrons colliding with CH_4, C_2H_4 and C_2H_6 molecules. *Journal of Physics B: Atomic and Molecular Physics*, 19(23):4035, 1986.

[151] K Floeder, D Fromme, W Raith, A Schwab, and G Sinapius. Total cross section measurements for positron and electron scattering on hydrocarbons between 5 and 400 eV. *Journal of Physics B: Atomic and Molecular Physics*, 18(16):3347, 1985.

[152] M. Charlton, T. C. Griffith, G. R. Heyland, K. S. Lines, and G. L. Wright. The energy dependence of positronium formation in gases. *Journal of Physics B: Atomic and Molecular Physics*, 13(24):L757, 1980.

[153] A. Kramida, Yu. Ralchenko, J. Reader, and NIST ASD Team. NIST Atomic Spectral Database, 2012.

[154] NIST Webbook.

[155] M. Khakoo, C. Winstead, and V. McKoy. Vibrational excitation of water by electron impact. *Physical Review A*, 79(5):052711, 2009.

[156] A A A El-Zein, M J Brunger, and W R Newell. Excitation of vibrational quanta in water by electron impact. *Journal of Physics B: Atomic, Molecular and Optical Physics*, 33(22):5033–5044, 2000.

[157] R J Gulley, M J Brunger, and S J Buckman. Resonant excitation of NH_3 by low energy electron impact: the $\nu_{1,3}$ normal vibrational modes. *Journal of Physics B: Atomic, Molecular and Optical Physics*, 25(10):2433, 1992.

[158] C M Surko, M Leventhal, and A Passner. Positron Plasma in the Laboratory. *Physical Review Letters*, 62(8):901–904, 1989.

[159] X.-P. Huang, F Anderegg, E M Hollmann, C F Driscoll, and T M O'Neil. Steady-State Confinement of Non-neutral Plasmas by Rotating Electric Fields. *Physical Review Letters*, 78(5):875–878, 1997.

[160] F Anderegg, E M Hollmann, and C F Driscoll. Rotating Field Confinement of Pure Electron Plasmas Using Trivelpiece-Gould Modes. *Physical Review Letters*, 81(22):4875–4878, 1998.

[161] R G Greaves and C M Surko. Inward Transport and Compression of a Positron Plasma by a Rotating Electric Field. *Physical Review Letters*, 85(9):1883–1886, 2000.

[162] R G Greaves and J M Moxom. Compression of trapped positrons in a single particle regime by a rotating electric field. *Physics of Plasmas*, 15(7):72304–72306, 2008.

[163] C. Isaac, C. Baker, T. Mortensen, D. van der Werf, and M. Charlton. Compression of Positron Clouds in the Independent Particle Regime. *Physical Review Letters*, 107(3):033201, 2011.

[164] D. B. Cassidy, S. H. M. Deng, R. G. Greaves, and A. P. Mills. Accumulator for the production of intense positron pulses. *Review of Scientific Instruments*, 77(7):073106, 2006.

[165] A. Kilcoyne, A. Aguilar, A. Müller, S. Schippers, C. Cisneros, G. AlnaWashi, N. Aryal, K. Baral, D. Esteves, C. Thomas, and R. Phaneuf. Confinement Resonances in Photoionization of $Xe@C_{60}^{+}$. *Physical Review Letters*, 105(21):213001, 2010.

[166] F A Gianturco and Robert R Lucchese. Computational investigation of positron scattering from C_{60}. *Phys. Rev. A*, 60(6):4567–4576, 1999.

[167] M. T. N. Varella, V. R. C. Carvalho, and M. A. P. Lima. New Directions in Antimatter Chemistry and Physics. page 493. Amsterdam: Kluwer, Netherlands, 2001.

[168] J. R. Machacek, R. Boadle, S. J. Buckman, and J. P. Sullivan. Search for positron quasibound states in the doubly excited region of the helium atom. *Physical Review A*, 86(6):064702, 2012.

[169] E Boroski and R M Nieminen. Electron-positron density-functional theory. *Physical Review B*, 34(6):3820–3831, 1986.

[170] J P Perdew and Alex Zunger. Self-interaction correction to density-functional approximations for many-electron systems. *Physical Review B*, 23(10):5048–5079, 1981.

[171] Ashok Jain. Low-energy positron-argon collisions by using parameter-free positron correlation polarization potentials. *Physical Review A*, 41(5):2437–2444, 1990.

[172] C. Winstead and V. McKoy. Elastic electron scattering by fullerene, C_{60}. *Physical Review A*, 73(1):012711, 2006.

[173] Hiroshi Tanaka, Ludwig Boesten, Kunizo Onda, and Osamu Ohashi. Crossed-Beam Experiment for the Scattering of Low Energy Electrons from Gas Phase C_{60}. *Journal of the Physical Society of Japan*, 63(2):485, 1994.

[174] Sydney Leach, Michel Vervloet, Alain Desprès, Emilienne Bréheret, Jonathan P. Hare, T. John Dennis, Harold W. Kroto, Roger Taylor, and David R.M. Walton. Electronic spectra and transitions of the fullerene C_{60}. *Chemical Physics*, 160(3):451–466, 1992.

[175] V. Piacente, G. Gigli, P. Scardala, A. Giustini, and D. Ferro. Vapor Pressure of C_{60} Buckminsterfullerene. *The Journal of Physical Chemistry*, 99(38):14052–14057, 1995.

[176] E Becker. *Gas dynamics*. Academic Press, 1968.